SCUOLA DI DOTTORATO
UNIVERSITÀ DEGLI STUDI DI MILANO-BICOCCA

Department of Materials Science

PhD program in Materials Science and Nanotechnology

PA-MBE Growth and Characterization of Nitride Semiconductors, from InGaN Thin-films to GaN and AlN Self-assembled Nanowires

Mani Azadmand

Cycle XXXI – Reg. n° 811341

Supervisor: Prof. Stefano Sanguinetti

Coordinator: Prof. Marco Bernasconi

ACADEMIC YEAR 2018-2019

To my best friend, my father

During this study he passed from this world. I dedicate this work with all my love to him.

He taught me the meaning of true love, the love which you give with no expectation, the love of a father to his child!

Rest in peace.

Acknowledgements

This thesis is an effort of years that involves many people for which I am so thankful and would like to express my sincere gratitude and give special mention in this acknowledgement.

First of all, I am extremely grateful to my supervisor, Prof. Stefano Sanguinetti, because of believing in me and providing me with endless knowledge. He was always supportive and very kind to me. I am also very thankful to my dear friend and colleague, Dr. Sergio Bietti, who patiently taught me the principles of the MBE and always was ready to my occasionally technical and scientific questions.

Additionally, I would like to gratefully acknowledge all members of our research group and collaborators: Prof. Emiliano Bonera, Prof. Richard Nötzel, Prof. Shiro Tsukamoto, Dr. Alexey Fedorov, Dr. Daniel Chrastina, Prof. Maurizio Acciarri, Prof. Riccardo Ruffo, Dr. Stefano Vichi, Prof. Fabio Pezzoli, Dr. Elisa Vitiello, and Dr. Francesco Basso Basset.

I am also thankful to Dr. Lutz Geelhaar and our research group in department of Epitaxy, in Paul Drude Institute in Berlin, where I did six months of research work as my PhD abroad period stage. I appreciate all the efforts done by Dr. Thomas Auzelle, Dr. Oliver Brandt, Dr. Gabriele Calabrese, Dr. Guanhui Gao, Dr. Jonas Laehnemann, and the laboratory technicians: Mr. Carsten Stemmler, and Ms. Katrin Morgenrot, in helping me to proceed with the study.

During three years of my PhD work, I have been honored to meet many nice people and make precious friendships. I am very thankful to my friends because of being with me in my both happy and hard moments.

Finally I would like to give a special thanks to my Family for always supporting my decisions in life, and also to my dear Fiancée who has been very encouraging and great comfort to me.

Contents

1. INTRODUCTION 6

1.1 The difficulty in obtaining high-In-composition $In_xGa_{1-x}N$ crystals 8

1.2 The existence of high densities of defects in III-N semiconductors 9

1.3 Organization of the manuscript 11

2. EXPERIMENTAL SETUP 13

2.1 MBE (Molecular Beam Epitaxy) 13

2.1.1 Equipment and working principles of MBE 14

2.1.1.1 Vacuum 16

2.1.1.2 Sources 18

2.2 Magnetron Sputtering 19

2.3 In-situ characterization techniques 20

2.3.1 Reflection High Energy Electron Diffraction (RHEED) 20

2.3.2 Quadrupole Mass Spectrometer (QMS) 23

2.4 Ex-situ characterization techniques 25

2.4.1 Scanning Electron Microscopy (SEM) 25

2.4.2 Raman Spectroscopy 28

2.4.3 High Resolution Transmission Electron Microscopy (HRTEM) 31

2.4.4 High Resolution X-ray Diffraction (HRXRD) 31

2.4.5 Atomic Force Microscope (AFM) 34

2.4.6 Photoluminescence (PL) 36

2.4.6.1 Time Resolved PL (TRPL) 38

2.4.7 Cathodoluminescence (CL) 39

2.4.8 Variable-angle Spectroscopic Ellipsometry 40

2.4.9 4-probe resistivity measurements 41

3. HETEROEPITAXIAL GROWTH OF INGAN THIN-FILMS ON SI(111) 43

3.1 Choosing the substrate 44

3.2 Substrate preparation 45

3.3 Droplet effects on growth rate 49

3.4 Calibration of Raman spectroscopy for InGaN in the central composition range 60

3.5 Droplet effects on Indium incorporation 66

3.6 Growth regimes: Metal-rich, N-rich, and Intermediate 71

4. GROWTH AND CHARACTERIZATION OF SELF-ASSEMBLED GAN AND ALN NWS ON TIN$_X$-SPUTTERED SAPPHIRE 77

4.1.1 SPUTTERING TIN$_x$ ON SAPPHIRE BY REACTIVE MAGNETRON SPUTTERING 78

4.1 SELF-ASSEMBLED GAN NWS GROWTH ON TIN$_x$-SPUTTERED SAPPHIRE 80

4.1.1 TWO-STEP GROWTH, THE KEY FOR HIGH-TEMPERATURE GROWTH OF GAN NWS ON TIN$_x$ FILM 91

4.2 SELF-ASSEMBLED ALN NWS GROWTH ON TIN-SPUTTERED SAPPHIRE 95

SUMMARY, CONCLUSIONS, AND OUTLOOK 107

FAILURES 110

PUBLICATIONS AND CONFERENCES 112

REFERENCES 114

Chapter 1

1. INTRODUCTION

Over the past 40 years, the family of III-N semiconductors consisting of the binary compounds InN, GaN, AlN, and their alloys, has emerged as one of the most important classes of semiconductor materials. They have bandgaps that span a very large spectral range, from InN (0.7 eV) near infrared (~1900 nm) to GaN (3.4 eV), and to AlN (6.2 eV) deep ultraviolet (UV) (~200 nm[1]. InN and AlN can be alloyed with GaN which allows tuning of the band gaps (from 0.7 to 6.2 eV) and emission wavelengths (see Figure 1.1).

All these materials are direct band gap semiconductors which makes them attractive for light emission applications. Short wavelength light emitters are required for full color display, laser printers, high density information storage, and under water communication. Moreover, the development of non-classical III-N light sources that produce streams of photons with controllable quantum correlations, in particular single-photon emitters (SPEs) are the fundamental resource for many scalable quantum information technologies[2–4]. Light to hydrogen conversion via water splitting is of immense interest as a clean, storable, and renewable energy source. InN/InGaN quantum dots (QDs) have a great potential to be used efficiently for this application[5]. III-N semiconductors are particularly suitable for applications in these areas.

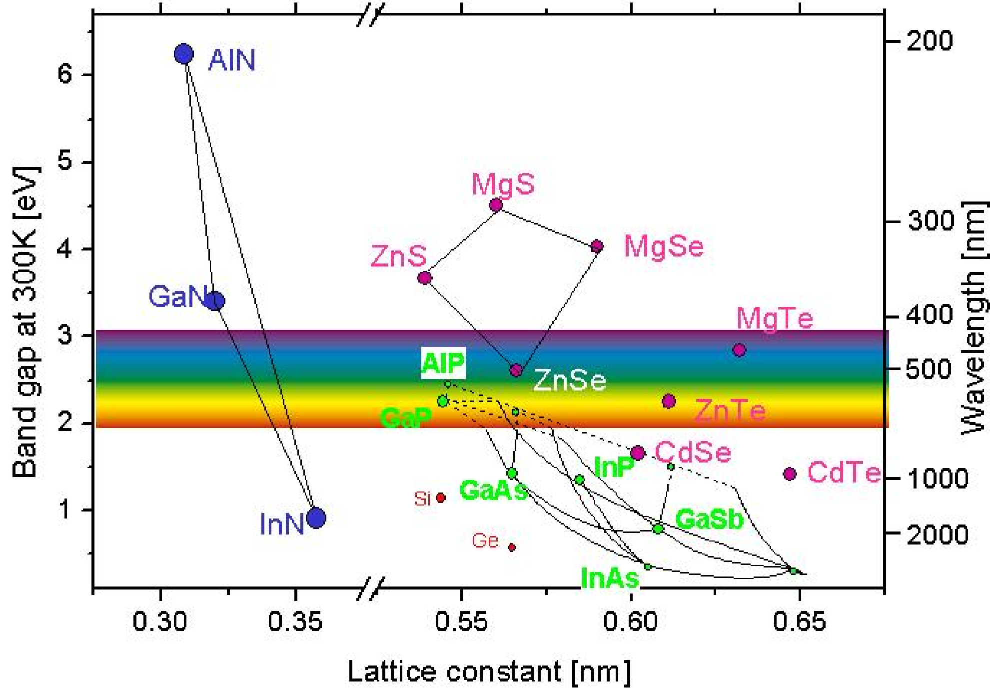

Figure 1.1: Lattice parameter and band gap of common semiconductors

GaN is the most common compound from this group. Over the past two decades, tremendous progress has been made in GaN-based optoelectronic devices, including light-emitting diodes (LEDs) and lasers operating in the blue and near-UV spectral range. Isamu Akasaki, Hiroshi Amano and Shuji Nakamura won the 2014 Nobel prize in Physics for the invention of efficient blue LEDs which has enabled bright and energy-saving white light sources.[6] By combining GaN LEDs with phosphors it is possible to fabricate high-efficiency white light emitters which are predicted to play a crucial role in future high-efficiency home and commercial lighting systems. Group III-nitrides have also found applications in other electronic devices. For example, advanced GaN/AlGaN high-power microwave transistors are now commercially available.[7]

However, the use of III-nitrides to realize high efficiency LEDs and lasers operating in the deep UV, deep visible, and near-IR spectral range, has remained very limited. Two main issues in realization of III-N full potential can be addressed: 1- The difficulty in obtaining high-In-composition $In_xGa_{1-x}N$ crystals, and 2- The existence of huge densities of defects in III-N semiconductors. The prophecy of this thesis is to remedy these issues.

1.1 The difficulty in obtaining high-In-composition $In_xGa_{1-x}N$ crystals

InGaN has unique properties like: high near band edge absorption, high carrier mobility, surface electron accumulation, and superior radiation resistance [7,8]. Its wide tunability of the band gap which spans from 0.7 to 3.4 eV (depending on the In amount in the composition) puts InGaN in high demand for many industrial applications. This large energy range covers almost the whole solar spectrum thus making InGaN the optimal material for many applications such as: light sources, light detectors, solar cells, photo electrochemical water splitting and electrochemical biosensors[9–12].

So far, the fundamental properties of GaN are relatively well established, and many excellent review papers can be found in the literature[13–15]. In contrast, the study of In(Ga)N is still in the early stage. This is mainly because of its difficulty in obtaining $In_xGa_{1-x}N$ crystals with high In amount, as a result of low dissociation temperature of InN and high equilibrium vapor pressure of nitrogen. Different binding energies of In-N and Ga-N are reflected in the different decomposition temperatures (630°C for InN and 850°C for GaN)[16]. So in case of InGaN growth at high temperatures, a significant reduction of In incorporation in the epilayer occurs not only due to the re-evaporation of adsorbed surface adatoms but also due to the thermal decomposition of In-N binds.

Attempts to increase the In amount in the crystal by raising the In flux, results in In droplet formation on the surface which further causes compositional gradient in the growth direction.[17] Since the size and the density of the droplets increase during growth, the average In content shows a vertical gradient in the film. Shimizu et al. [18] realized in short growth times there is only a few or no In droplet generation (even in high In pressure). So they suggested the growth of a thin GaN layer when the In droplets are not generated or still small, can prevent the formation of In droplets and consequently increase the In amount in final composition. They succeed to increase the indium mole fraction to 29% which was much higher than 12% achieved by single layer grown under the same conditions.

As another successful approach, low growth temperatures have been used to avoid InN decomposition and In desorption, thus allowing the growth of high-In-composition InGaN layers by plasma-assisted molecular beam epitaxy (PA-MBE) [19–22] as well as metal organic vapor phase

epitaxy (MOVPE).[23] Aseev et al.[9] has shown the ability of tuning the emission wavelength up to near infrared by increasing the Indium percentage in InGaN thin-films. Benefiting from high-In-composition InGaN layers grown in low-temperature regime, Alvi et al. applied InN/InGaN QDs for electrochemical sensing applications such as biosensors for clinical diagnosis[10,24] and ion-selective electrodes[11], and in different applications like generating hydrogen by water splitting[5,25]. However, in InGaN low-temperature growth, the generation of metal droplets is critical since the excess of metal atoms accumulate on the surface (In-N dissociation temperature is lower than the onset temperature for the evaporation of In)[26], unless the growth is carried in N-rich conditions which will cause the 3D growth and rough surface[27,28].

In this thesis, the presence of metal droplets on the surface, during the InGaN low-temperature growth, and their effects on adatom incorporation dynamics is studied. The optimum growth window, where is possible to grow InGaN single crystal, under a good control on both composition and morphology of the layers is proposed.

1.2 The existence of high densities of defects in III-N semiconductors

Due to high melting temperature and a very high decomposition pressure, GaN cannot be grown using conventional methods used for GaAs or Si like Czochraslski or Bridgman growths. So, there is no GaN bulk single crystal commercially available (with an acceptable price) and all technological development of III-N-based devices relies on heteroepitaxial growth[1,29,30] which generates huge densities of defects (with 10^9–10^{11} cm^{-2} density of threading dislocations (TDs)) due to lattice mismatch of grown layers with the substrate.[31] For instance, the heteroepitaxial growth of III-N semiconductors on Si wafers allows for low cost and large mass production. But the growth of Ga(In)N directly on Si, due to inevitable formation of amorphous SiN interlayer, proceeds under weak epitaxial constraint (weak epilayer- substrate interaction) resulting in 3D growth mode. [32,33] To avoid this problem, Zhang et. al. used an AlN buffer layer on Si which was very beneficial for improvement in crystal quality of InGaN layers.[34] However, AlN buffers are detrimental for the III-N/Si heterojunction electrical functionality. A promising approach to improve the crystal quality of (In)GaN grown on Si substrate, is nitridation process at high

temperatures, since it can improve the epitaxial relation between grown layers and the substrate.[19,35]

On the other hand, growing laterally relaxed 3D structures like nanowires (NWs) (also called nanorods, nanocolumns, nanowhiskers, etc) seems an attractive solution to solve the problem with lack of lattice-matched substrates, as they can release the epitaxial strain through a lateral plastic relaxation[36].

GaN NWs can be grown free of threading dislocations on a variety of lattice-mismatched substrates including Si. This versatility constitutes a strong asset compared to conventional heteroepitaxial GaN layers. However, in spite of their high structural perfection, the excitonic lifetime of state-of-the-art GaN NW ensembles grown on Si substrates by MBE does not exceed 250 ps at 10 K, whereas it may reach ~1 ns for freestanding GaN layers grown homoepitaxially. This short lifetime evidences the presence of a strong non-radiative channel in GaN NWs, attributed to point defects rather than structural defects or surface recombination.[37] These non-radiative point defects may either originate from deep impurities such as Ca stemming from the ex-situ substrate preparation[38] or be formed by native defects, making the use of a higher growth temperature desirable. At these high temperatures, however, Si substrates may start to decompose.[39]

Analogously to the case of GaN, the lack of lattice-matched substrates significantly constrains the heteroepitaxial growth of high-quality AlN films and the related devices usually need to cope with a large density of extended defects. So similarly, an interesting workaround is the growth of AlN in the shape of NWs. However, the heteroepitaxial growths of AlN NWs by MBE carried out at a substrate temperature below 1000 °C have systematically ended up in severely coalesced ensembles.[40] Due to the low mobility of Al adatoms, even higher growth temperatures would be desirable to obtain well-separated AlN NWs. However, above 1000 °C, conventional substrates like templates of GaN NWs or Si would significantly degrade.[41,42]

In this thesis, I introduce a very promising approach to grow high-quality self-assembled GaN and AlN NWs on an in-situ-produced substrate with metallic conductivity which can be used as a back contact. The GaN NWs grown in this study have shown an excitonic life-time as long as 0.52 ns, which is by far, the longest excitonic life-time has been achieved for GaN heteroepitaxial materials.

1.3 Organization of the manuscript

This thesis is manly devoted to the investigation of PA-MBE growth and characterization of III-N materials, in particular InGaN thin-films, and GaN and AlN NWs. For the sake of simplicity in naming the samples, for each group of III-N materials, the first letter of the composition is used prior to the number of the sample. For instance, I1 represents the first InGaN sample, or G3 is the GaN sample number 3, and so on. All the InGaN samples discussed in chapter 3, are grown as thin-films and all GaN and AlN samples discussed in chapter 4, are grown in the shape of nanowires. After the first chapter which was an introduction to III-nitrides, the summary of the next chapters is as below.

Chapter 2

In chapter 2, the growth and characterization techniques which are used in this study are briefly explained.

Chapter 3

In chapter 3, heteroepitaxial growth of InGaN thin-films on Si(111) with focus on the central composition is discussed. The growth influence of III/N ratio on the growth mechanism, morphology, and composition of InGaN thin-films is studied. The existence of metal droplets on the growth surface and relevant role of droplets in determining the InGaN growth dynamics, are exclusively discussed by analyzing the adatoms and the kinetics of incorporation in the presence of droplets. Also the related mathematical models to observed phenomenon are proposed. The important role of Vapor-Liquid-Solid (VLS) growth mode that takes place under the droplets in the InGaN epilayer growth is explained. The In incorporation suppression by metal droplets during the growth of InGaN layers in metal-rich condition is discussed.

Moreover, Raman spectroscopy of InGaN (with the focus on the central composition) as a fast method to measure the $In_xGa_{1-x}N$ composition, is studied and by combining the obtained data with the reported data in literature, the Raman spectra for whole InGaN composition is calibrated.

All the discussions in this chapter is based on my work in Materials Science Department of Milano Bicocca University and LNESS institute, under the supervision of Professor Stefano Sanguinetti.

Chapter 4

As it mentioned in chapter 1, the III-N devices mostly are grown heteroepitaxially on lattice mismatched substrates which causes the generation of large densities of defects in the crystal. In this regard, the growth of NWs, seems a promising approach. The conventional substrates have not fulfilled all the requirements in order to grow non-coalesced III-N NWs. In this chapter, I investigate the self-assembled growth of high-quality GaN and AlN NWs on TiN_x-sputtered sapphire. I will discuss the advantages of TiN-sputtered substrate as an ideal surface to grow high-quality GaN and AlN NWs.

At first I will report the sputtering procedure of TiN_x films on 2-inch sapphire wafers by Magnetron sputtering system. Then, PA-MBE growth and characterization of self-assembled GaN NWs on the TiN_x-sputtered sapphire is discussed. The first motivation of this study is the advantage of using a refractory and clean substrate and its compatibility with GaN NWs growth condition, which allows to grow high quality and pure GaN NWs in elevated temperatures without suffering from unwanted doping due to atoms diffusion from substrate to NWs. The second motivation of this work is the TiN metallic conductivity which is very beneficial from application point of view by opening up the possibility of making back contact to the NWs.

In the second part of this chapter, I explain the PA-MBE growth and characterization of self-assembled AlN NWs with high crystalline quality and optical properties on TiN-sputtered sapphire. Similar to GaN NWs growth, here also I get advantage of TiN high temperature performance, to increase the growth temperature.

The work of this chapter, is based on my PhD abroad period, in Paul Drude Institute (PDI) in Berlin, under supervision of Dr. Lutz Geelhaar and tutorship of Dr. Thomas Auzelle.

Chapter 2

2. Experimental setup

In this chapter I introduce the experimental tools which I used during my PhD work.

2.1 MBE (Molecular Beam Epitaxy)

The word “epitaxy” is taken from the two Greek words, epi "above" and taxis "in ordered manner".[43] Epitaxial growth of thin films (such as semiconductors) is the growth of a single crystal layer, such that the crystal lattice of the semiconductor grows to match the crystal structure of a carefully chosen substrate.

Since a molecular-beam apparatus was first successfully used by Cho[44] and Arthur[45] in the late 1960s to crystallize and investigate GaAs epilayers, high-vacuum epitaxial growth techniques using particle beams have developed rapidly. This development accelerated when different semiconductor devices with quantum-well structures were invented in the 1970s. The three epitaxial growth techniques that are mainly pursued are: MBE, CVD (Chemical Vapor Deposition), and LPE (Liquid Phase Epitaxy).[46]

MBE is an ultra-high vacuum (UHV, $<10^{-8}$ Torr) technique for epitaxial growth via interaction of one or several molecular or atomic beams that occurs by impingement of the beams (originated from effusion cells or gas source crackers or plasma cells) onto a surface of a rotating heated crystalline substrate. MBE has the capability to grow artificially layered crystals of various complexity with a high degree of control and reproducibility. It has become a popular technique for growing III-V compound semiconductors as well as several other materials. MBE can produce high-quality layers with good control of thickness, doping, and composition. In this method, not only single atomic layer can be grown, but also a good control to grow complex alloys with very abrupt interfaces is possible. Atomic scale changes in the composition can be achieved by shuttering sources, allowing for the growth of complex quantum well and super-lattice structures. Besides producing quantum wells, it is also possible to produce other low dimensional structures like quantum dots not only by Stranski-Krastanow Mechanism but also trough the droplet epitaxy method[47,48]. In MBE, consumption of source material is reasonably small and reproducibility with

high accuracy is achievable. However, its low growth rate and long recovery time after each exposure to air (opening the main chamber) are the main obstacles in the way of its industrialization.

2.1.1 Equipment and working principles of MBE

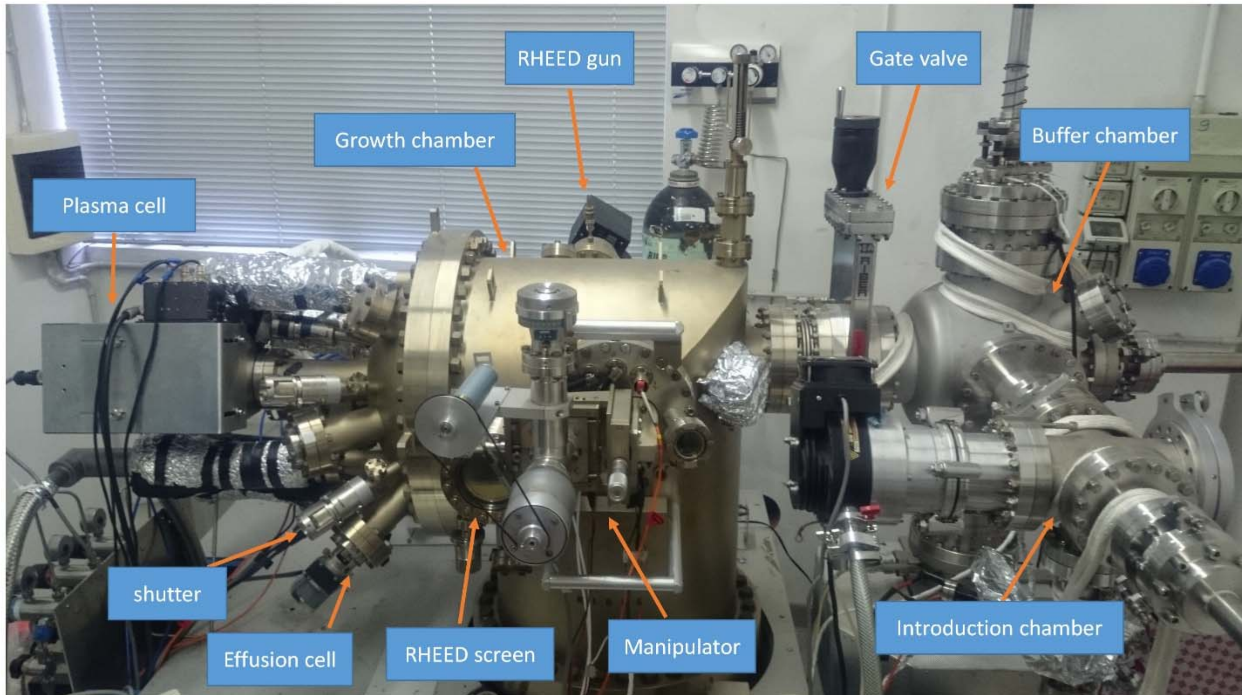

Figure 2.1: PA-MBE (Riber 32) used in this thesis. The components characteristic of the main elements of the system are indicated.

In MBE, the constituent elements of a semiconductor in the form of 'molecular beams' are deposited onto a heated crystalline substrate to form epitaxial layers. MBE growth is conducted far from thermodynamic equilibrium and is governed mainly by the kinetics of the surface processes occurring when the impinging beams of adatoms react with the outermost atomic layers of the substrate.

In Figure 2.1 the PA-MBE system which is used to grow InGaN thin-films in this thesis with indication of its components is shown. The system consist of a loading chamber (also called introduction chamber), where samples are loaded and outgassed at 200 ºC to remove water, a buffer chamber (also called preparation chamber) which keeps the loading chamber apart from the growth chamber through its gate valves (and also can host several samples), and a growth chamber (also

called main chamber) where samples are transferred to proceed to the growth. The transfer between chambers can be done by mechanical/magnetic arms (push rods) through gate valves.

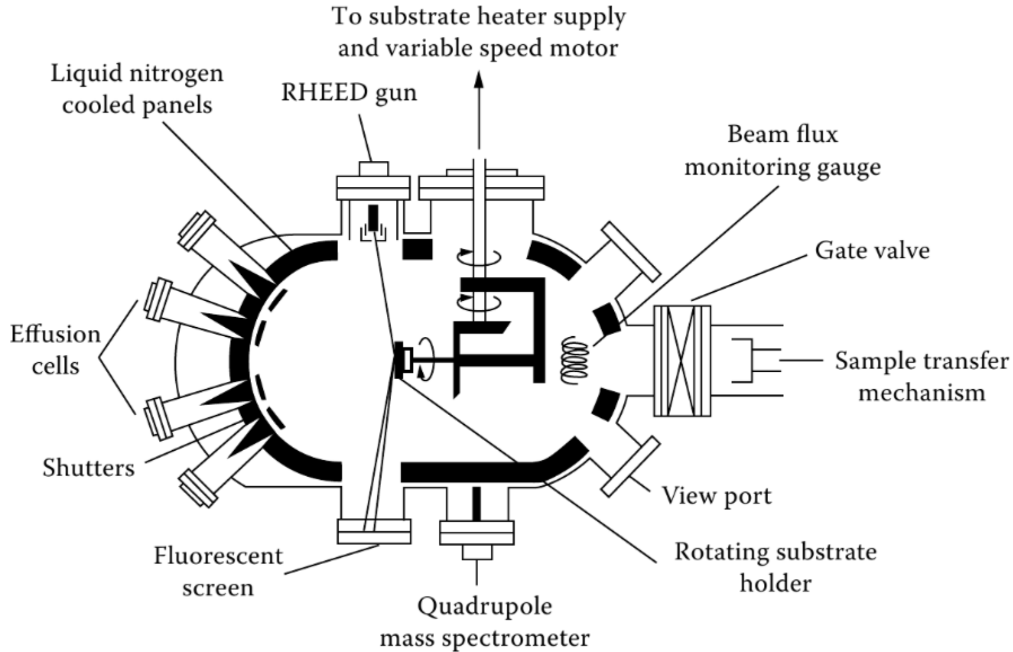

Figure 2.2: a typical setup for a MBE growth chamber[49]

Within the growth chamber (Figure 2.2) the substrate wafer is placed and fixed in a substrate holder with a heating filament located behind the substrate with a small distance where also a thermocouple is fixed near to center of substrate to measure the changes in the substrate temperature. The substrate temperature is one of the main growth parameters which can be controlled using thermocouple (or/and pyrometer) and can be tuned by applying a voltage to substrate heater. Normally a proportional-integral-derivative (PID) controller is used to control the applied voltage to reach a determined temperature, by following a function based on the feedbacks coming from thermocouple.

The position of substrate can be changed using substrate manipulator. Before growth, the sample holder is flipped around from the loading position so that the sample faces the material sources. Considering that the molecular beams have different impinging angles in respect to the substrate, the sample holder is designed for continual azimuthal rotation of the sample to improve layer uniformity.

2.1.1.1 **Vacuum**

All the three chambers are independently pumped to achieve a working pressure of high or ultra-high vacuum. In the growth chamber, UHV condition is necessary to ensure a long mean path of atoms and molecules, so that a molecular beam regime is maintained (no dispersion). The mean path must be greater than the distance between the effusion cells and the substrate, which is usually a few tens of centimeters. If we suppose that an atom evaporated with temperature T has cross section σ, in a vacuum chamber with pressure p, the mean free path would be:

$$\lambda = \frac{k_B T}{\sqrt{2}\pi\sigma^2 p} \tag{2.1}$$

Typical values for σ are 2-5 Angstrom, so that a pressure of at least 10^{-5} mbar is required. This is an approximation for the upper limits to the system operability. However pressures as low as 10^{-9} mbar are required to grow high purity layers (deposition rate from background pressure gas much lower than 0.001 ml/s), so that λ is comparable to the distance between the effusion cells and the substrate holder. Such a vacuum can be achieved by a combination of vacuum pumps, namely, a rough pumping with a rotary pump (down to ~10^{-3} Torr) that is used for pumping the back pressure of a turbo molecular pump to achieve a pressure of 10^{-7} - 10^{-8} Torr. An ion pump brings the pressure down to 10^{-9} - 10^{-10} Torr (the safe starting point to use an ion pump is below 10^{-5} Torr). The ultimate UHV can be reached pressure of 10^{-10} - 10^{-11} Torr by running liquid nitrogen continuously to cool down the walls of cryoshroud. Its panels are located inside the growth chamber, surrounding the growth region and acting as an effective pump for many of the residual gasses in the chamber.
To keep such ultra-high vacuum condition, the chamber must be resistant to the compression forces from outside and also not to desorb materials from its body in the vacuum. Also standard metal gaskets must be used in the points of junction. To measure the pressure inside the chambers, based on the required range of measurement, different pressure gauges are used.
The **Pirani gauge** can be used reliably for the range between 1-10^{-5} mbar. It consists of a metal sensor wire, suspended in a tube linked to the vacuum chamber connected to an electrical circuit.

The wire is heated and its loss of heat due to the gas molecules collisions is taken into account as an indirect indication of pressure. After a calibration, the pressure can be read.
The other class of pressure gauge is **cold cathode gauge** which is used for the pressure range of 10^{-3} - 10^{-8} mbar. In this type of gauge, the gases are ionized by a strong electrical field. A magnetic field is also used to increase the path of the electrons produced by the cathode and that ionizes the gas molecules. The positive ions produced this way are collected by the cathode and so the ionization current is measured.
In the main chamber normally a **Hot Filament Ionization Gauge** (sometimes called **Bayard-Alpert ionization Gauge)** is the choice of use. This gauge is widely used at very low-pressures from 10^{-3} to 10^{-9} mbar. A UHV Bayard-Alpert gauge together with the schematic representation of filament and grid is shown in Figure 2.3. To measure the pressure, a filament is heated to emit electrons and a DC voltage is applied to the external grid to accelerate the electrons to pass through the grid and collide with molecules existing around. As the consequence, a part of molecules are ionized and attracted to the central ion collector wire by a negative potential applied on this wire. The current is measured which is a composition-dependent current since different ions will produce different currents at the same pressure. However if the gas composition is constant, the current will be directly proportional to the pressure.

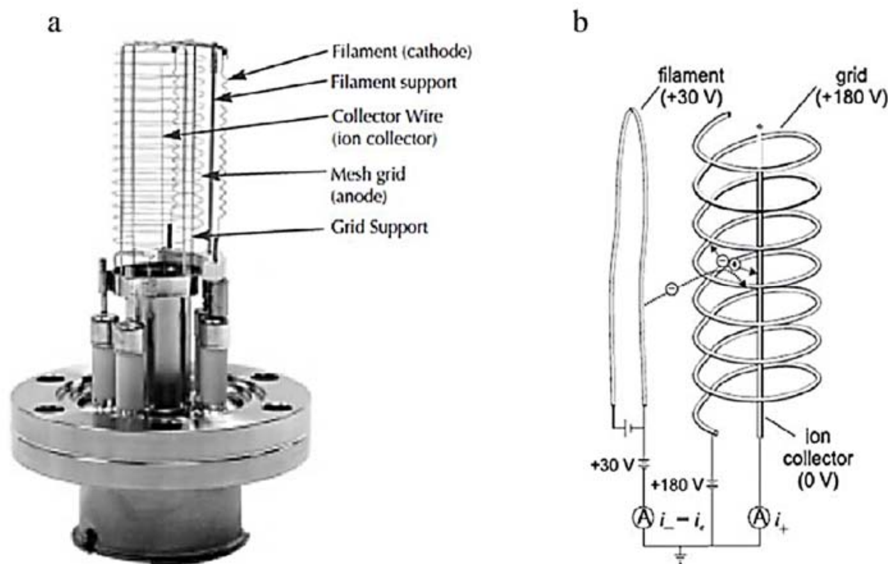

Figure 2.3: (a) Bayard-Alpert filament UHV gauge, (b) schematic representation of filament (cathode) and grid (anode)

Sufficiently low pressures of 10^{-10} Torr (the MBE system which is used for growing InGaN thin-films) and 10^{-11} Torr (the MBE system which is used for growing GaN and AlN nanowires) are achieved in this study which allows for the growth of high-purity materials.

2.1.1.2 **Sources**

Sources are key elements of any MBE system. They must be designed to supply the needed uniformity and material purity. The molecular beams (group III materials in this study) are obtained by Knudsen cells. Knudsen cells, or K- cells are the standard evaporation source for most MBE systems. It consists of a heating element, surrounding heat shield and a crucible thermocouple assembly mounted on a port flange. A thermocouple is mechanically attached to the crucible bottom. The cells include an integral cooling system in addition to heat shields. Construction materials are usually refractory metals such as tantalum and molybdenum and insulators like alumina and PBN. Lower temperature applications allow alumina, but due to the outgassing of contaminants, at temperatures above a few hundred degrees usually it is necessary to use PBN. In front of each Knudsen cell there is a mechanically driven molybdenum shutter to stop the beam in a very short fraction of time. The desired flux, can be achieved by changing the temperature of the materials in the cell. Similar to the substrate heater, here also a PID controller can be employed to accurately control the applied voltage based on the temperature set point and the feedbacks from the thermocouple.
To supply the so called “active nitrogen”, we use a radio frequency (RF) Plasma cell. Plasma cell is an effusion cell which generates the ionized molecular beam by an electrical discharge created from the inductive coupling of a RF excitation coil. In this way, RF plasma source provides very reactive atomic species by breaking the nitrogen molecules. To create N plasma, pure molecular nitrogen is fed from a high pressure cylinder, to pass through pressure regulators, filters, purifiers, valves and a mass flow controller, into radio frequency (RF)-Plasma source where the molecules break and turn to active nitrogen, which mostly consists of reactive atomic/ionized nitrogen (so called nitrogen radicals). This reactive atomic species can escape into the vacuum chamber along with nitrogen molecules N_2 that are not dissociated or ionized. Ion deflection plates are fitted to the source to deflect the ions which are escaped away from their path toward the sample.

Since, the plasma cell is used in MBE, these growth technique is called plasma-assisted (PA-MBE) or radio frequency (RF-MBE) molecular beam epitaxy.
All the cells are aligned to the center of sample where they bond and make the crystal structure. By changing the N_2 flux (can be tuned by a mass flow controller) and the applied power, we can change the flux of active N. Typically to control the III/V ratio, we fix the flux of active N at an optimum point (based on the required growth rate and considering the pumping condition in the growth chamber) and then only by changing the flux of group III, we tune the ratio. The regularly check and calibration of cells is required to keep the III/V ratio constant. To calibrate the group III materials, for each cell separately, we record and plot the variation of pressure vs the temperature of the cell.
All the III-N samples involved in this study (more than 120 samples including: GaN, InN, InGaN, and AlN) are grown by me using two PA-MBE systems (one in University of Milano Bicocca and the other one in PDI).

2.2 Magnetron Sputtering

Magnetron sputtering has become the process of choice for the deposition of a wide range of industrially important coatings.[50] It is a Plasma Vapor Deposition (PVD) process. In fact, sputtering inside an enclosed chamber which cooled by liquid nitrogen was introduced by Theuerer and Hauser (1965) and has been used by several teams for DC sputtering in UHV systems allowing deposition of high-purity films. In this technique positively charged ions are accelerated by potentials ranging from a few hundred to a few thousand electron volts to hit the negatively charged target (material to sputter) with sufficient force to dislodge and eject atoms from the target. These atoms will be ejected in a typical line-of-sight cosine distribution from the face of the target and will condense on the surface (substrate) that is placed in vicinity of the magnetron sputtering cathode. Conductive materials can be deposited using a direct current (DC) power supply and insulators can be deposited by using a radio frequency (RF) power supply. When a magnetic field is used to fold the ions and electrons trajectories, mean free path is increased and sputtering yield is increased.[51]
In this thesis I used a magnetron sputtering system to sputter TiN film on 2-inch conventional sapphire substrates. This TiN-sputtered substrate later is used as the surface to grow GaN and AlN

nanowires. Our sputtering chamber is linked to a MBE chamber which allows us to transfer the sputtered-substrates directly from sputtering chamber to MBE chamber without exposing the sample to air. This assembly allow to have extremely pure surface which is produced in UHV atmosphere and transferred to the MBE growth chamber under the UHV condition. I have performed this part of study in Epiaxial department of PDI.

2.3 In-situ characterization techniques

In-situ characterization techniques refers to the techniques which characterize the sample during the growth. As it is mentioned before, in MBE growth, working in UHV, enables us to monitor the growth procedure. Variety of characterization apparatuses can be assembled inside the MBE chamber depend on the needs. Below, we discuss two of the most common instruments which can be find in the majority MBE systems.

2.3.1 Reflection High Energy Electron Diffraction (RHEED)

Reflection high-energy electron diffraction (RHEED) is an important technique for in-situ and real-time surface study on flat surfaces. One of the main advantages of MBE over CVD, is operation of growth in UHV condition which gives us the possibility of doing in-situ characterizations such as RHEED to monitor the growth of thin-films. It allows to get a live picture of the reciprocal space lattice of the sample surface. It is extremely sensitive to surface changes, either by structural changes or due to chemicals adsorption. This technique is remarkably simple to implement, requiring at the minimum only an electron gun, a phosphor screen, and a clean surface. In Figure 2.4 schematic image of RHEED is depicted.

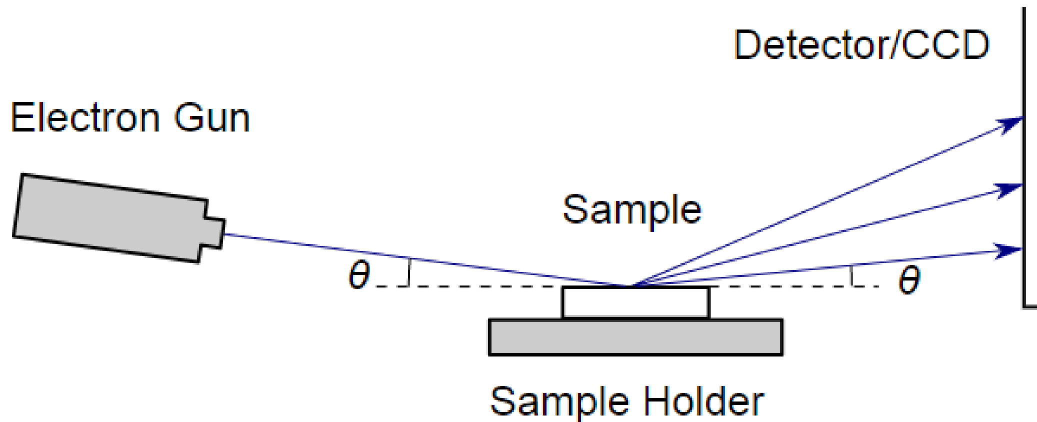

Figure 2.4: Schematic image of RHEED setup

In this method, high energy beam of electrons in the range 5-40 keV (The de Broglie wavelength of these electrons is therefore in the range 0.17-0.06 A) is directed at a low angle (1°-3°) to the surface. The electrons which are either diffracted or reflected on the sample surface are imaged on a phosphor screen. Due to this low angle incident beam, no interference with the growth process occurs. Moreover, it has a very strong effect on the diffraction. For example, atomic steps can produce large changes in both the measured intensity and the shape of the diffracted beams when the important atomic separations are parallel to the incident beam direction. In contrast, the role of atomic structure in the diffracted intensity is primarily determined by the atomic separations perpendicular to the beam direction. Also in this set up, the penetration depth is extremely small limiting its sensitivity to the atomic structure of the first few planes of the crystal lattice. The extent of these sensitivities, the importance of multiple scattering, the shape of the diffraction pattern, and the main features of calculation are all determined by the combination of a small glancing incident angle and the conservation of parallel momentum. These controlling factors are conveniently described by the Ewald construction in the reciprocal space of a surface, which will be seen to be a family of parallel rods. A schematic of set of crystal planes separated by a distance 'd' in real space and their Fourier transfer in reciprocal space, is shown in Figure 2.5. The distance between adjacent points in a reciprocal lattice is inversely proportional to the distance between points in the corresponding direction of the direct lattice. For a purely planar lattice mesh the periodic repeat distance is infinite in the perpendicular (z) direction. The reciprocal lattice points along the surface normal are therefore infinitely dense (rods in reciprocal space).[52,53]

Based on the shape of the Bragg spots, one can infer the roughness of the surface as well as the crystallinity of the grown layers. A streaky RHEED pattern indicates a very smooth surface, whereas a spotty RHEED pattern indicates the existence of small 3D features on the surface, polycrystalline surface results in arc-shape pattern, and randomly diffracted electrons from an amorphous surface, form a halo image on the screen.

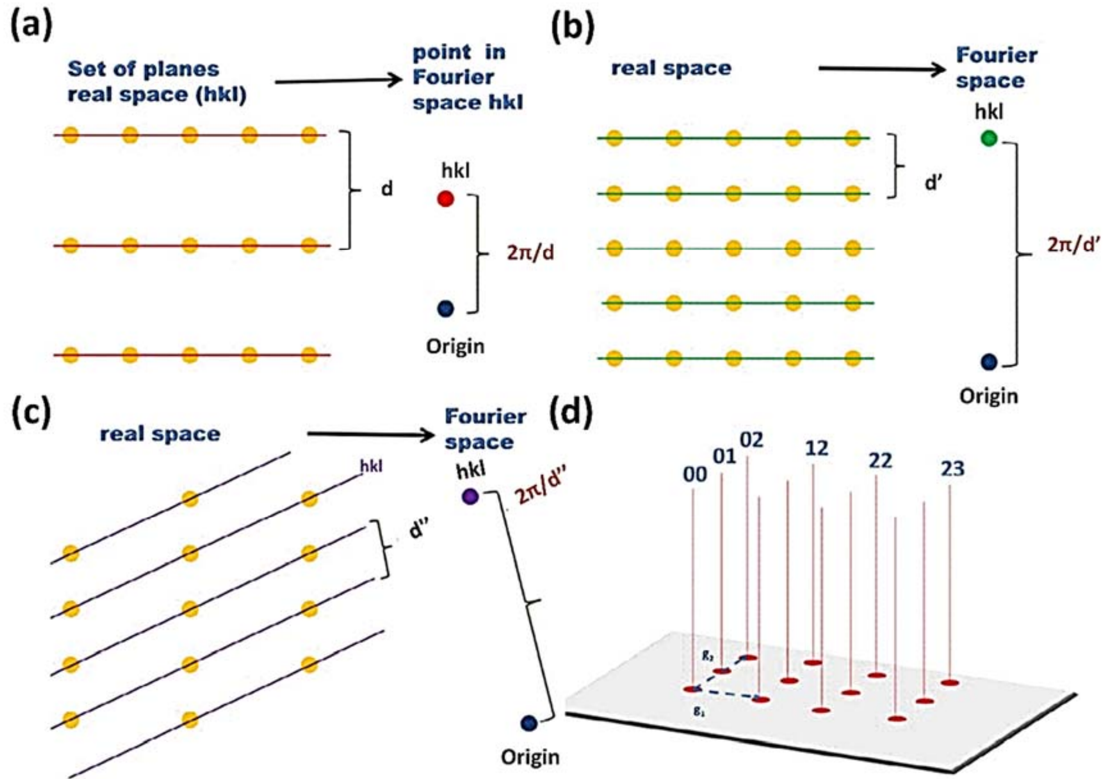

Figure 2.5: (a) Relation between a set of planes in real space and Fourier space. (b) Effect of a smaller distance between the atomic planes in real space and Fourier space. (c) Effect of non-parallel set of planes in real space and Fourier space (d) reciprocal rods from a planar lattice mesh.

As a summary of its applications, based on the RHEED patterns it is possible to have in-situ observation on important items such as:

- Crystal quality (single crystalline, polycrystalline or amorphous layers are growing)
- Very useful information about the surface flatness (growth mode, 2D, 3D)
- Surface reconstruction (normally we use it to monitor the native oxides removals from Si surface, and to calibrate the thermocouple temperature as later will be explained)

- Recognition of crystal structure and growth direction
- Lattice parameter and strain in the structure (if the setup is precisely tuned)
- Monitoring the formation of QDs
- In case of Nanowires: measuring incubation time (required time for nucleation) as well as qualitative information about density and side facets, tilt, and etc.
- The growth rate (each oscillation means one monolayer)
- Monitoring nitridation process (as will be shown later)
- RHEED is also used for some special applications[54] which is out of the concept of thesis

2.3.2 Quadrupole Mass Spectrometer (QMS)

QMS is a powerful tool that allows determining the type and amount (partial pressure) of molecules and therefore is used to determine the residual gas species within the growth chamber. The QMS benefits from using a quadrupole radio-frequency electric field (dynamic mass analyzer) which forces ions of a particular mass onto stable oscillatory trajectories. A typical feature present in a mass spectrometer, is that mass separation is established according to the ratio $\frac{M}{z.e}$ (M: molecular mass, e: elementary charge and z: number of elementary charge s). A doubly charged ion hence appears on the scale of a mass spectrometer (which refers to z=1) at half the value of its true mass. In Figure 2.6 a schematic image of QMS with its main components is shown. As can be seen, it consists of an ionizer (similar to the Bayard Alpert, i.e bombardment by electrons from a hot filament), an ion accelerator, and a mass filter consisting of four parallel metal rods, and a detector.

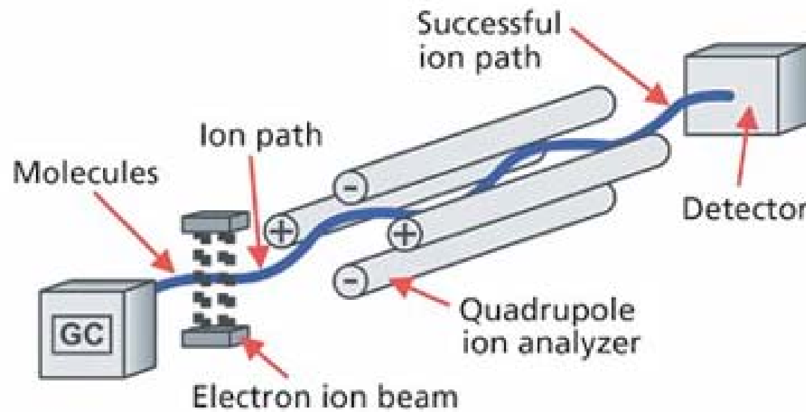

Figure 2.6: A quadrupole mass analyzer scheme

From the four rods, two (opposite) rods have an applied potential of (U+Vcos(ωt)) and the other two rods have a potential of -(U+Vcos(ωt)), where U is a DC voltage and Vcos(ωt) is an AC voltage. The applied voltages change the trajectory of ions traveling down the flight path located between the four rods. For given DC and AC voltages, only ions of a certain mass/charge ratio pass through the quadrupole filter while all other ions are expelled of their original path. In this way, a mass spectrum is obtained by monitoring the ions passing through the quadrupole filter as the voltages on the rods are varied. It is also very efficient technique to detect leaks by blowing small amount of He to the outer walls and joints and detecting it inside the chamber. Another application of the QMS is adsorbing/desorbing flux measurements. When a substrate is placed in a gas medium, the process of adsorption will start. Under static conditions, the adsorption will continue until an equilibrium concentration of adsorbed particles is reached. This method allows determining various adsorptions and desorption parameters, such as: (i) number and population of various desorbing phases, (ii) activation energy of desorption, (iii) order of the desorption and (iv) the pre-exponential frequency factor for the desorption.[53] In this way, nucleation of depositing material, or desorption of deposited material (and the amount of deposited/desorbed material) can be monitored. It becomes even more important when RHEED is unable to determine it (e.g. when the lattice parameters of the depositing materials are very close).

In this study we benefit from QMS (as will be discussed in chapter 4) by monitoring the Ga-Ti intermix during the nucleation of GaN NWs on TiN_x-sputtered substrate which makes valuable information to optimize the sputtering and growth process.

2.4 Ex-situ characterization techniques

In contrast to in-situ characterization techniques, ex-situ characterization techniques refer to techniques which we use to characterize the samples after the growth. Below, some of the most common semiconductor characterization techniques which we have employed in this thesis are briefly explained.

2.4.1 Scanning Electron Microscopy (SEM)

SEM is a very practical instrument in order to have morphological information as well as structural characterization of grown thin-films and NWs. In contrast to a standard optical microscope, SEM employs electrons instead of photons to image the sample. The required electron wavelength can be tuned dependent on the acceleration voltage. For instance if the working voltage is 10 keV, the wavelength of emitted electrons from electron gun would be 0.012 nm which is significantly below the wavelength of 400 to 700 nm used in a conventional optical microscope, therefore leading to higher resolution (spatial resolution in the order of a few nm) images. One of the advantages of this method is the simplicity of sample preparation. Before inserting the sample into the SEM chamber, it needs to be mounted on a metallic holder. An important point is that since we are dealing with huge number of electrons in the electron beam, it is required to make a good (conductive) contact between the sample and the holder. If the sample is not conductive, its surface needs to be coated with conductive materials. Carbon and Gold are the typical materials which are used for the coating.

The main compounds in a typical SEM, are: vacuum chamber, electron gun, a demagnification unit, a scan unit and a detection unit. We need high vacuum (~ 10^{-6} Torr) in order not to obstruct the electron beam by the particles in the way. The source of electrons in the SEM is called electron gun which produces a large and stable current in a small electron beam. There are two types of electron guns. One is the thermionic gun which heats a filament until electrons stream away. The

electrons are gathered as an electron beam following into a metal plate (anode) by applying a positive voltage (1-30 kV) to the anode. The other type of electron gun is called field emission gun which rips electrons away from their atoms by generating a strong electrical field (in this case the system will be called FE-SEM). The main advantages of FE-SEM over the SEM are that its filament has a longer lifetime and also gives higher resolution. There is a hole in the anode which allows a fraction of the electrons to continue down the column through the lenses to produce a smaller, more cohesive beam. A series of electromagnetic lenses within a vacuum chamber are employed to direct the electrons towards the specimen. The focal length can be changed by varying the current that passes through a coil that is around a ferromagnetic material. In the chamber, there are two sets of lenses. One is the condenser lens (located on the top) and the other is objective lens (located at bottom). The condenser lens converges the cone of the electron beam to a spot below it, before the cone flares out again, it is converged back again by the objective lens and down onto the sample. This initial convergence can be at different heights. The closer it is to the lens, the smaller the spot diameter at the point of convergence. The current which is applied to condenser lens, controls this initial spot size and is referred to as the spot size control. The diameter of this initial convergence (also called a cross-over point) affects the final diameter of the spot beam on the sample. When the focused beam of electrons is exposed to the sample, based on the interaction of electron with the sample, electrons and X-rays will be emitted from the surface of sample. They can have different energies, based on how they are produced. They are attracted to and collected by a detector. Due to the interaction of electrons with atoms in the sample, various signals are produced that contain information about the sample's surface topography. If the SEM is equipped with EDX (energy dispersive X ray analysis, also called energy dispersive spectroscopy, which in this case it will be abbreviated as EDS), it would also be capable of performing analyses of selected point locations on the sample which is especially useful in qualitatively or semi-quantitatively determining chemical compositions. Also from the density of electrons a map of the surface can be obtained. An overview of the possible interactions is presented in Figure 2.7, the electron interaction with matter is seen to be limited to the penetration regime, the so-called excitation volume. Hence, it depends on the acceleration voltage of the electrons and material density.

The two often used types of signal are backscattered and secondary electrons. The backscattered electrons occur due to elastic collisions of electrons with atoms, which causes a change in the electrons’ trajectory. Since larger atoms (larger atomic number) are more effective in scattering

the electrons compared to light atoms (smaller atomic number), they create a higher signal which on the image it will be seen whiter. So, if there are existing some phases with different kinds of atoms, this imaging mode is very useful to distinguish them. In contrast, the secondary electrons originate from the near-surface regions of the sample. They occur due to inelastic interactions between incident electron beam and the sample and so contain lower energy than the backscattered electrons. Secondary electrons are very beneficial for the topographical images of the sample's surface.

In this thesis, SEM (with a secondary electron detector), is used very frequently to investigate thickness and morphology of thin-films (in University of Milano Bicocca), as well as size, density and coalescence degree of NWs (in PDI). This characterization is performed by me. In order to reduce the detrimental effect of the electron accumulation on the surface (so called "charging") during high magnification imaging, I used silver paint to improve the contact between the sample and the metallic holder.

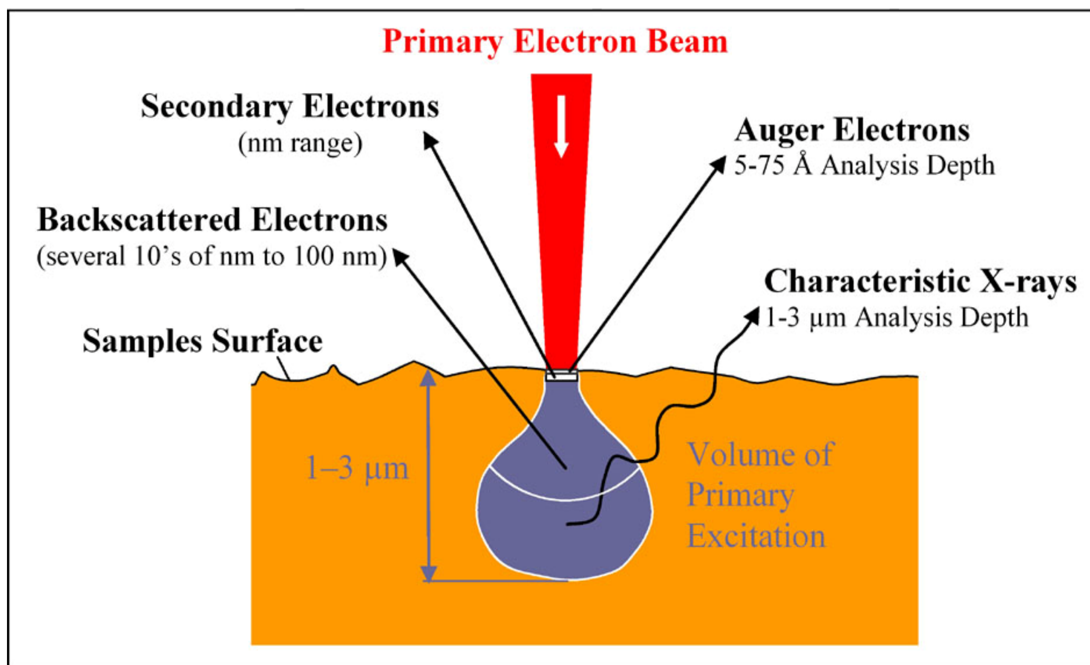

Figure 2.7: Schematic of electron interaction with matter [Image adapted from www.surfgroup.be]

2.4.2 Raman Spectroscopy

Raman spectroscopy is a non-destructive spectroscopic technique that can detect both organic and inorganic species and measure the crystallinity of solids. In this method, a monochromatic radiation is scattered in the sample to gain information about the composition, crystalline degree, presence of strain and defects, and purity of the material by analyzing vibrational, rotational, and other low- frequency modes of the system.

It is a fast and simple method with the possibility to investigate the sample locally (since the light beam can be focused to a small diameter). It is finding increased use in semiconductor characterization particularly to investigate the amount of strain. Combining Raman spectroscopy with other characterization methods like X-ray diffraction, it is possible to provide a data bank for different materials and in this way, have the opportunity to quickly characterize the composition and/or strain, by using Raman spectroscopy.

The scattered light contain mainly wavelength that was incident on the sample (Raleigh scattering) but also at different wavelengths at very low intensities (few parts per million or less) that represent an interaction of the incident light with the material. According to quantum theory, a molecular motion can have only certain discrete energy states and any change in the state is thus accompanied by the gain or loss of one or more quanta of energy. The interaction of a molecule with electromagnetic radiation can thus be analyzed in terms of an energy-transfer mechanism. The interaction of the incident light with optical phonons is called Raman scattering while the interaction with acoustic phonons results in Brillouin scattering. In Figure 2.8 a schematic image of energy distribution of scattered light is shown.

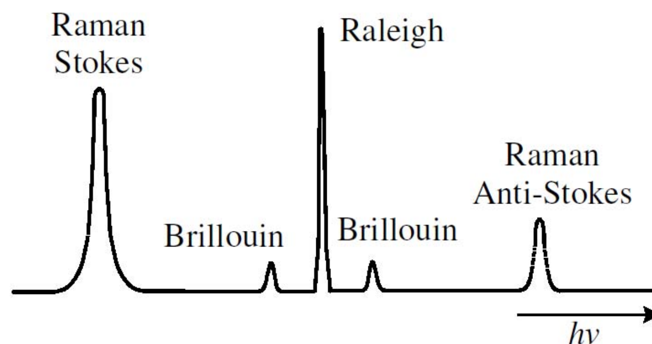

Figure 2.8: Energy distribution of scattered light

In general, the optical phonons have higher energies than acoustic phonons giving larger photon energy shifts, but even for Raman scattering the energy shift is small and since the intensity of Raman scattered light is very weak (about 1 in 10^8 parts), Raman spectroscopy is only practical when an intense monochromatic light source like a laser is used.

In this thesis, as I will discuss later, the study is mainly on III-N semiconductors with wurtzite crystal structure. Wurtzite structure, consists of four atoms in its unit cell (N = 4), so there are (3N = 12) twelve possible normal phonon modes which three of them are acoustic phonons and nine optic phonons. Taking into account degeneration, there are eight possible modes (two acoustic and six optical) at the point Γ of the first Brillouin zone.

$$\Gamma_{acoustic} = A_1 + E_1$$
$$\Gamma_{optical} = A_1 + 2B_1 + 2E_2 + E_1 \tag{2.2}$$

Among the six optical modes, the two modes E_2 are only Raman-active, the modes A_1 and E_1 are both Raman and IR active, and instead the two modes B_1 are not active for Raman or IR.

	GaN (cm^{-1})	InN (cm^{-1})
A_1-TO	533^a	480^b
E_1-TO	560^a	476^b
A_1-LO	735^a	580^b
E_1-LO	742^a	570^b
E_2-(low)/E_2^1	145^a	87^b
E_2-(high)/E_2^2	567^a	488^b
B_1-(low)	210^c	200^b
B_1-(high)	320^c	540^b

Figure 2.9: Phonon Frequencies in cm^{-1} for GaN and InN in the wurtzite structure.

The calculated phonon dispersion relations for bulk InN (left) and GaN (right) and their corresponding density of states are shown in Figure 2.10. As can be seen, there is a wide phononic

band-gap, especially in case of InN. This is the result of atomic mass differences between N atoms respact to Ga (a factor of 5) and In (a factor of 8.2) atoms.

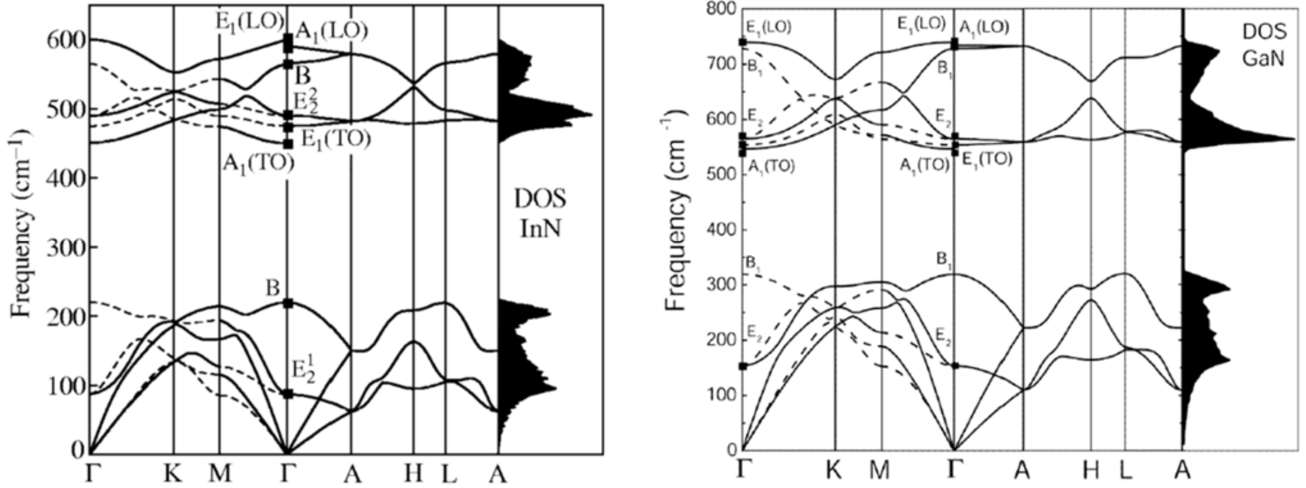

Figure 2.10: Phonon dispersion relations calculated for bulk InN (left) and GaN (right) and their corresponding density of states (DOS).

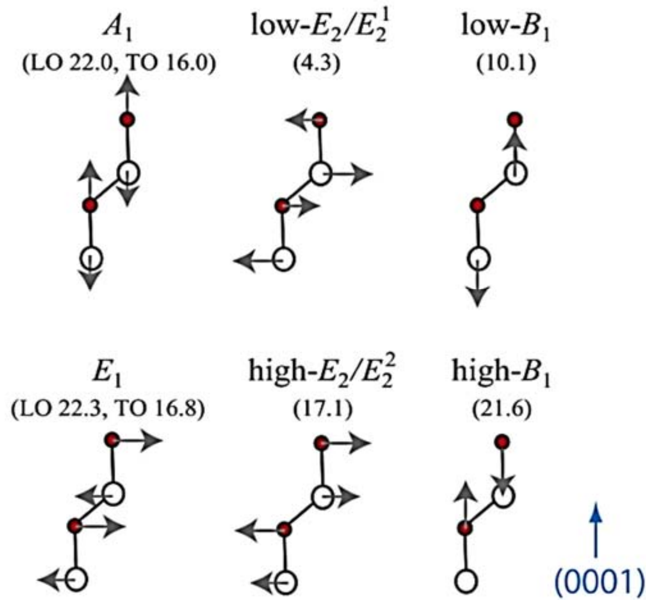

Figure 2.11: Atoms displacement for phonon modes in Γ for Wz-GaN. In red the nitrogen atoms, in white Gan atoms. With "low" and "high" are indicated the low and high frequency mode respectively. The number in brackets are the frequency in THz for GaN

In this thesis, I performed the Raman spectroscopy measurements of InGaN thin-films at University of Milano Bicocca and of TiN thin-films, and GaN and AlN NWs at PDI. I benefit using Raman spectroscopy to investigate different phonon modes and extract valuable information about $In_xGa_{1-x}N$ composition, Ti/N ratio of TiN_x films and to check if the grown thin-films and NWs are relaxed or strained.

2.4.3 High Resolution Transmission Electron Microscopy (HRTEM)

High-resolution transmission electron microscopy (HRTEM) is an imaging mode of specialized transmission electron microscopes (TEMs) that uses both the transmitted and the scattered beams to create an interference image from the atomic structure of the sample. It can be used with crystalline solids to obtain direct images of small structural groups comprising a few coordination polyhedra with resolution nearly as small as the unit cell of the crystal. In this method, all electrons emerging from the sample are combined at a point in the image plane. HRTEM has been extensively and successfully used for analyzing crystal structures and lattice imperfections of various kinds in advanced materials at atomic resolution. It can be used for analyzing crystal structures and grain boundaries, or examining lattice imperfections such as: very small defect regions, faults in the stacking sequence of structural groups or atom layers, and isolated defects in narrowly delimited areas that may actually be below the dimensions of the unit cell[53,55]. In case of epitaxial grown material, HRTEM can be effectively used to investigate the interface, dislocations, stacking faults, Quantum structures, and polarity of grown crystal.
In this study, HRTEM is used to study the AlN NWs. The measurements are carried out at PDI by a specialist TEM operator.

2.4.4 High Resolution X-ray Diffraction (HRXRD)

HRXRD is a non-destructive technique for determining atomic and molecular structure of a crystal. In case of epitaxial growth of thin-films, it is a powerful characterization technique to precisely investigate the strain state of epitaxial layers, as well as the chemical composition. It requires little sample preparation and gives structural information over entire semiconductor wafers but it is not possible to scan the sample locally. It is also unable to identify impurities.

In this method, X-rays from a quasi-point source are sent to the crystal surface under a given angle (Θ). After being reflected by different crystal planes, the resulting rays are detected as a function of the sample (or detector) rotation angle. A simple schematic image of XRD technique is depicted in Figure 2.12.

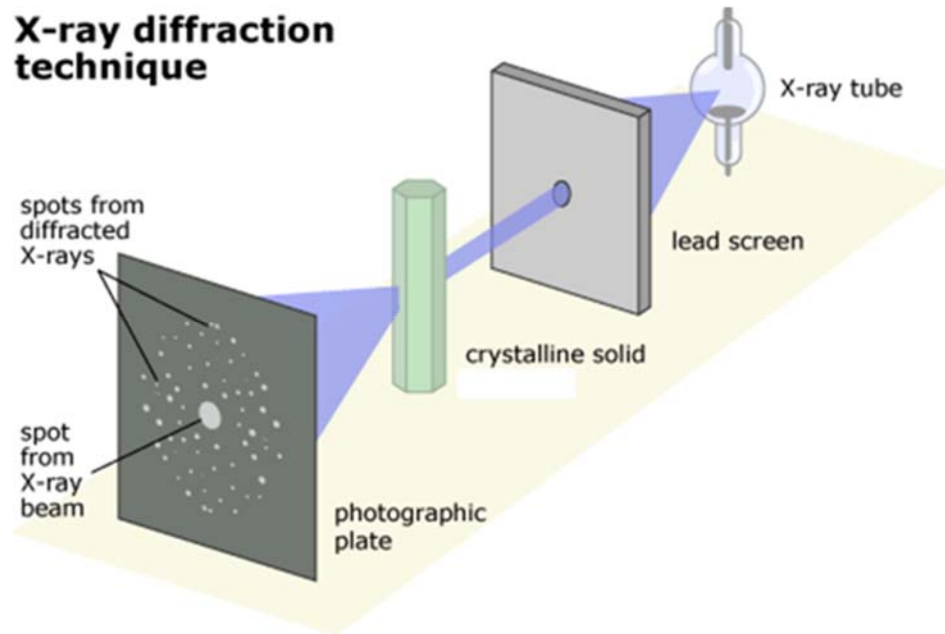

Figure 2.12: Simple schematic of XRD technique

The basis of all XRD measurements is described in Bragg's Law, which determines the angles for constructive and destructive interference between rays emerging from the crystal

$$n\lambda = 2d.\sin\Theta \tag{2.3}$$

Equation (2.3) represents the Bragg's law for constructive interference, where n is an integer, λ is the wavelength of monochromatic X-rays impinging under an angle Θ on a set of planes with lattice spacing d_{hkl} where (hkl) are the Miller indexes.

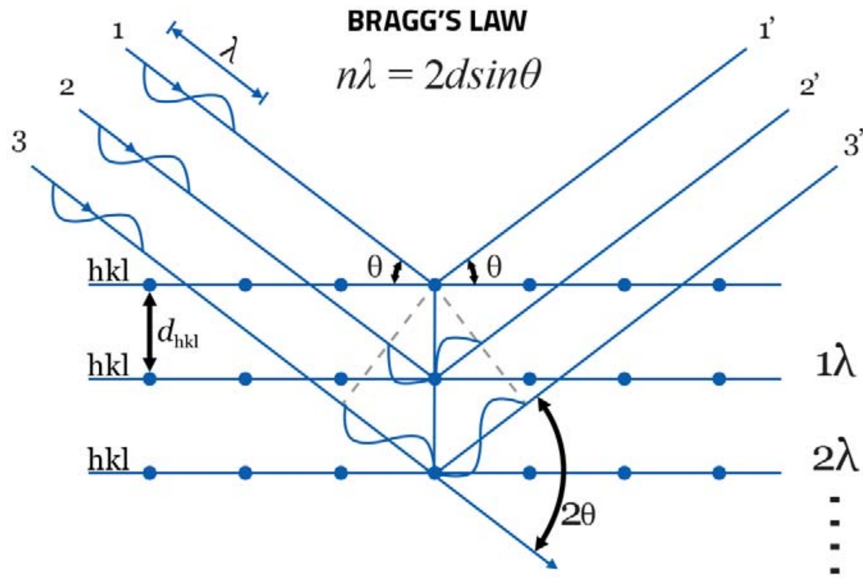

Figure 2.13: Schematic of X-rays diffraction and Bragg's law

A schematic image of X-rays diffraction and bragg's law is shown in Figure 2.13. In case of relaxed layers, it is possible to determine the lattice constant value, the layer thickness and composition by just applying the Bragg's law to each peak in the spectrum.

There are two instrumental configurations for HRXRD, that in each, the monochromator provides a conditioned beam. One is the double-axis experiment in which the detector does not discriminate between different diffraction angles 2theta. The other is the triple-axis experiment where a slit or analyzer crystal determines the angular acceptance of the detector.

In this study, to determine the In amount in $In_xGa_{1-x}N$ thin-films, monochromatic CuKα1 radiation was used, with λ = 0.154056 nm. ω–2θ scans around the InGaN(0002) Bragg peak is carried out, using the Si(111) peak from the substrate as a reference. In this kind of scan, the scattering vector $\vec{q} = \vec{k}_i - \vec{k}_f$ changes length but not direction; the direction is chosen to be normal to the (111) planes of the substrate. ω is the incidence angle and 2θ is the scattering angle; this kind of geometry is "symmetric" since $\omega \simeq 2\theta/2$.

This can be used to determine the c parameter (the (0001) plane spacing) of the InGaN in terms of the scattering angle 2θ(0002),

(2.4)

$$\frac{1}{c} = \frac{2}{\lambda} sin\theta_{(0002)}$$

which can then be used to estimate the In content under the assumption that there is no strain. Vegard's law is often used for the lattice parameters of alloys, i.e. it is assumed that the relevant property of $In_xGa_{1-x}N$ can be found by linear interpolation between GaN and InN.[56]

Table 2.1: Lattice constants of GaN and InN as compared to the Si(112) and (111) spacing[57], and expected θ values in the InGaN(0002)||Si(111) XRD scan.

	a [nm]	c [nm]	θ [°]
GaN	0.3187	0.5186	17.2819
InN	0.3533	0.5693	15.7010
	$d_{(\overline{1}\overline{1}2)}$ [nm]	$d_{(111)}$ [nm]	θ [°]
Si	0.2217	0.3136	14.2193

In this study, I use XRD mainly to:

- To obtain the In content in $In_xGa_{1-x}N$ thin-films and later to calibrate Raman data for the whole composition of $In_xGa_{1-x}N$
- Determine epitaxial relation between $In_xGa_{1-x}N$ and the Si substrate
- Determine tilt and twist of the grown layers/NWs respect to the substrate
- Check homogenous (shift in the peak) and inhomogeneous (broadening of the peak) strain in NWs.
- Find the NWs side facets crystallographic plane

The XRD measurements of InGaN thin-films are performed at LNESS institute by a specialist operator and to characterize TiN thin-films, as well as GaN and AlN NWs, I have operated the XRD measurements at PDI.

2.4.5 Atomic Force Microscope (AFM)

AFM is a high resolution scanning probe microscope that measures local properties such as vertical and lateral dimensions (with a resolution of fractions of a nanometer), or magnetism and current

when provided with an adequate probe tip. In case of morphological properties, a very sharp tip normally made of Si_3N_4 or Si is placed at the edge of cantilever that has a spring constant varying in the 0.01-50 N/m range. In Figure 2.14 schematic image of an AFM and its main components is depicted. AFM is used to profile the surface (scanning the surface in x and y directions) of thin films at a nm scale. When the tip approach contact with the thin film surface the cantilever deflects. A laser is used to measure the magnitude of deflection, therefore determining the height in relation to a set point. AFM can be operated in tapping or contact mode.

In tapping mode the probe to sample distance is set so that the probe tip lightly contacts ("taps") the sample surface during the cantilever oscillation. As the probe interacts with the surface of a sample, the oscillation amplitude or phase relation to the exciting signal change in response to the interaction. The interaction provides the basis for producing an image of the sample. Tapping mode reduces both the lateral forces on the tip (and the possibility of breakage) as well as collection of impurities on the tip. Unlike traditional contact mode which maintains a constant cantilever deflection, the tapping mode feedback loop keeps the cantilever oscillating at a constant amplitude.

Contact mode is often an order of magnitude faster and allows for atomic scale resolution, although it suffers from tip wear due to direct contact. At very small tip-sample distances (a few angstroms) a very strong repulsive force appears between the tip and sample atoms. Its origin is the so-called exchange interactions due to the overlap of the electronic orbitals at atomic distances. When this repulsive force is predominant, the tip and sample are considered to be in contact.

AFM does have issues imaging rough samples or samples where the spacing between features is smaller than the size of the AFM tip, as this leads to improper imaging of the sidewalls of the features.[46,49,53]

One of the most important applications of AFM is to study the QDs in which, the size, shape, and density of QDs can be easily investigated without any need for sample preparation.

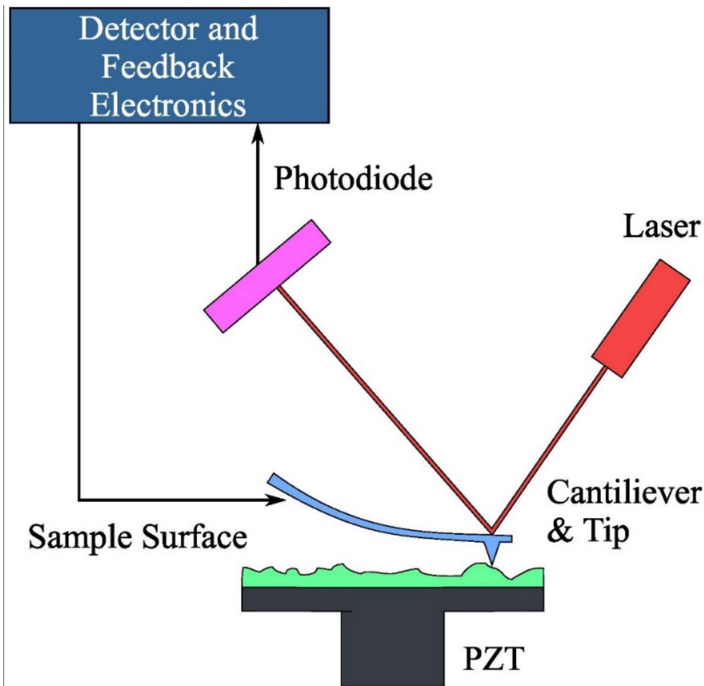

Figure 2.14: Schematic image of an AFM probe [adapted from Wikipedia]

In this thesis, morphological characterization of the samples are performed by AFM, using an ultra-sharp tip with a curvature radius of 2 nm and operating in tapping mode. Gwyddion is used as the typical software to translate the recorded data from AFM to images, and to extract further information like root mean square (RMS) roughness of the InGaN thin-films. The operations are performed mostly by me, in LNESS institute.

2.4.6 Photoluminescence (PL)

Photoluminescence is a very sensitive nondestructive method to analyze both intrinsic and extrinsic semiconductor properties. By determining the electronic bandgap, PL can provide a means to quantify the elemental composition or the strain in the structure of crystal. However the method is particularly suitable for characterization of the centers which control the electrical properties of the layers and for the detection of shallow-level impurities, but can also be applied to certain deep-level impurities, with radiative recombination. The high sensitivity of this technique provides the potential to identify extremely low concentrations of intentional and unintentional impurities that can strongly affect material quality and device performance.

The technique consist of generating high energy e-h pairs in a material (through excitation) using a laser and to measure their radiative recombination in the material. Photoluminescence is also used in other applications. PL can provide simultaneous information on many types of impurities in a sample, but only those impurities that produce radiative recombination processes can be detected. It has been largely the domain of III–V semiconductor characterization in the past with high internal efficiency. Internal efficiency is a measure of optically generated electron-hole pairs and radiative recombination, thereby emitting light. Photoluminescence has the advantage of the ability to discriminate between species involved in radiative recombination and can provide simultaneous information on many types of centers. However, compared to elementary techniques of electrical characterization, it is less well suited for the determination of impurity concentrations, particularly for the electrical majority species. Besides that, it is only applicable in case of high-quality crystals with ability of photon emission.

Photoluminescence is in general a convenient technique, requiring in the simplest form a suitable source of optical excitation, a spectrometer and a detector suitable for the emitted light. In case measurements at low temperatures is required (depend on the material and the purpose of measurement), the sample must be placed in a cryostat. In this method a photon source (laser) used to excite an electron into the conduction band, after which the electron then relaxes to a lower state by emitting a photon. The optical emission may involve other states, so that features may correspond to conduction to valence band transitions (C-V), free excitons (X), excitons bound to neutral donors or acceptors (A°X), conduction band to acceptor transitions (CA), or donor to acceptor transitions (DA) as illustrated schematically in Figure 2.15 (a) and (b). In general, specific information about the centers, the donors and acceptors, which promote electrical conductivity, can be obtained only when the electrical carriers are frozen out in these centers. Once the electrical carriers are thermally liberated, the impurities or defects which released them reveal their presence only through some inhibition of carrier mobility. The other advantage of low temperature measurement is the dramatic reduction of spectral broadening due to vibration processes.[46,58,59]

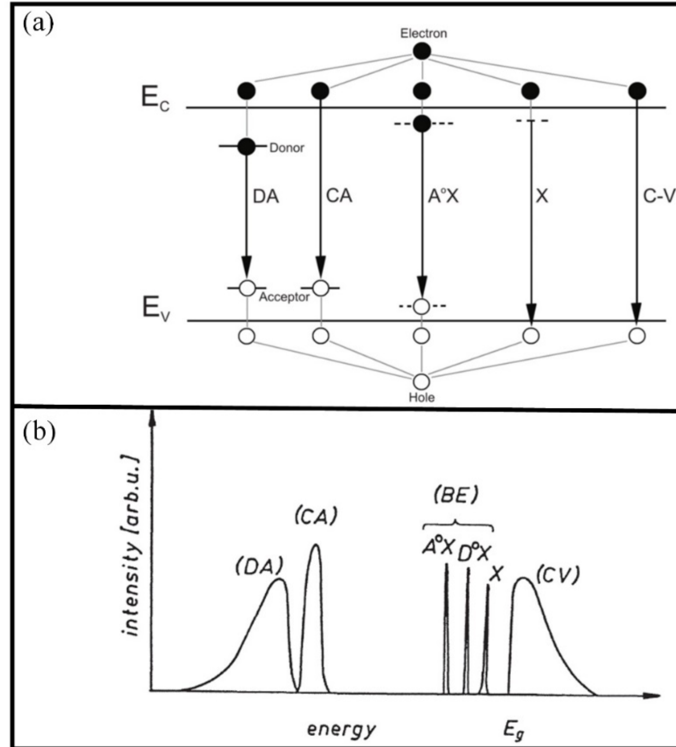

Figure 2.15: (a) Schematic representation of donor- or acceptor- related and direct radiative recombinations.[46] (b) Main parts of a near-band-edge photoluminescence spectrum. [58]

The PL measurements reported in this thesis are used in order to investigate:

- The impurity level in the NWs by checking near band edge as well as possible deep level radiative recombination.
- The crystal quality of NWs by considering the radiative/non-radiative recombination ratio as well as Time-resolved PL (as will be explained in following)
- Strain in the crystal

The PL measurements are performed by specialist operator at PDI.

2.4.6.1 Time Resolved PL (TRPL)

TRPL is an experimental technique that provides the spectral and temporal evolution of the emission of a sample following its illumination by a short pulse of light. It gives information on transient processes such as exciton capture, exciton transfer, and exciton recombination related to

bound excitons. In this method a short laser pulse is used for excitation, and a fast detector is used to determine the emission of material as a function of time after excitation. The short pulse of light generates electron-hole pairs that decay to lower energy levels of the sample. These electron-hole pairs can subsequently recombine and emit light. The emitted light is composed of a set of wavelengths corresponding to transition energies of the sample and, as a result, the measurement of the optical spectrum as a function of time provides a means to measure the transition energies and their lifetimes. The decay process, is very sensitive to additional non-radiative recombination channels, as well as to excitation transfer processes at higher doping levels.[60] So it provides useful information about the quality and purity of the material. The decay time is normally on the order of picoseconds or nanoseconds (for instance, the excitonic lifetime of state-of-the-art GaN NW ensembles grown on Si substrates by MBE does not exceed ≈250 ps at 10 K). In this case, the non-radiative channels are attributed to point defects rather than structural defects or surface recombination. [37]

In this study, I used this method to investigate GaN NWs grown on TiN film.

2.4.7 Cathodoluminescence (CL)

The basic principle is to generate high energy e-h pairs in a material by electron excitation and to measure the radiative recombination of these e-h pairs in the material. CL is very similar to PL and has the additional ability to generate e-h pairs in desired areas by moving the electron beam. There are some limitations concerning photoluminescence in choosing the laser for exciting the electrons in semiconductors with different band gaps or probing a small area (the size of the laser spot, typically on the order of 500μm, which is too large for probing individual NW). To obtain information about individual NWs CL can be used, which is based on the emission of light from electron beam excitation using a SEM. With the enhanced resolution achieved with the SEM, spatial variation in the optical properties can be directly mapped to physical features.[46]

In this thesis, since the required energy to excite AlN is very high (> 6 eV), instead of PL, CL is employed to investigate the luminescence properties of the AlN nanowires. The CL measurements are performed by specialist operator at PDI.

2.4.8 Variable-angle Spectroscopic Ellipsometry

Ellipsometry is a contactless, non-destructive technique measuring changes in the polarization state of light reflected from a surface which can be used both in-situ as well as ex-situ. In this method, polarized light is incident on the sample. The light is reflected from the sample and the ellipsometer detects the change in the state of polarization of the light. Usually linearly polarized monochromatic light is incident at some definite angle of incidence onto the sample (Figure 2.16). After reflection from the sample, light turns out to be elliptically polarized. If the parameters characterizing the substrate ambient and light beam are known, then optical characteristics of the film and their changes during MBE growth can be studied in-situ according to the changes of the reflected wave polarization. It deals with intensity-dependent complex quantities compared to intensities for reflectance or transmittance measurements. Ellipsometry can be thought of as an impedance measurement, while reflectance or transmittance can be viewed as power measurements. Impedance measurements give the amplitude and phase, whereas power measurements only give amplitudes. One determines the complex reflection coefficient ratio of the sample that depends on the ratio of the complex reflection coefficient for light polarized parallel and perpendicular to the plane of incidence. Ellipsometry is used predominantly to determine the thickness of thin dielectric films on absorbing substrates, line width, and optical constants of films or substrates.

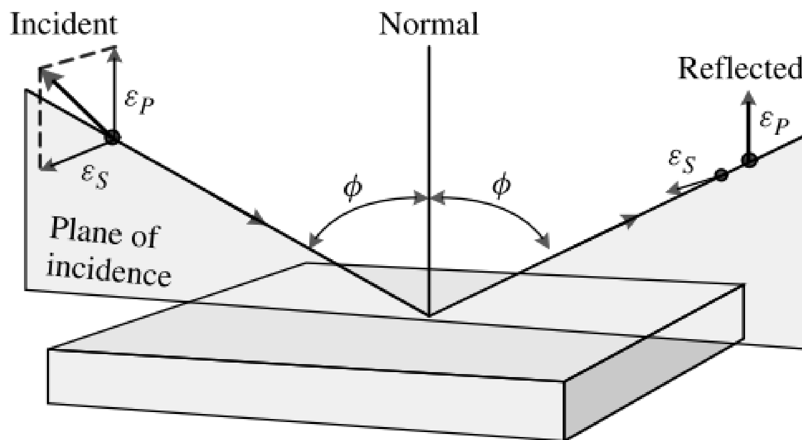

Figure 2.16 : schematic of polarized light reflection from a plane surface. Φ is the angle of incidence

The fact that ellipsometry measures the polarization state, rather than the intensity as in reflectometry, makes it inherently a high-precision technique which is relatively unaffected by experimental difficulties caused by source intensity fluctuations or light-scattering defects, which may occur even on the most carefully prepared surfaces. The capability of measuring phase changes directly gives ellipsometry great sensitivity to the presence of thin films on reflecting surfaces, which may be detected to average thicknesses of the order of hundredths of a monolayer.[58,59]

Although one of the main applications of this method is to measure the thickness of thin-films, in this study we use it for different purpose. As I will explain in chapter 4, we use this method to study the electronic properties of TiN film which later will be used as the surface to grow GaN and AlN nanowires. Ellipsometry measurement of the TiN surface, gives us a pseudodielectric function which has a real part ($\langle \varepsilon 1 \rangle$) and an imaginary part ($\langle \varepsilon 2 \rangle$). The $\langle \varepsilon 1 \rangle$ at low energies, when it is crossing zero can be investigated to see if the film shows metallic behavior or not. The other benefit we got from this results in our work, is to determine the Ti/N ratio in TiN_x composition. However, it is not a direct measurement and the references (database) is required to compare the results and only by comparing to the references we can measure this ratio.

The ellipsometry measurements are performed by me and my colleagues at PDI.

2.4.9 4-probe resistivity measurements

A four point probe is a standard simple apparatus for measuring the resistivity of semiconductor samples. By passing a current through two outer probes and measuring the voltage through the inner probes allows the measurement of the sample's resistivity (Figure 2.17). It consists of four probe arranged linearly in a straight line at equal distances from each other. A constant current is passed through the two probes and the potential drop V across the middle two probes is measured. It is an absolute measurement without recourse to calibrated standards and is sometimes used to provide standards for other resistivity measurements. This method is employed when the sample is in the form of a thin wafer, such as a thin semiconductor material deposited on a substrate. An oven is provided with a heater to heat the sample so that behavior of the sample is studied with

increase in temperature. Thin layers are often characterized by their sheet resistance R_{sh} expressed in units of ohms per square. The sheet resistance of the sample is given by[61]

$$R_{sh} = \frac{\rho}{t} = \frac{\pi}{\ln(2)} \frac{V}{I} = 4.532 \frac{V}{I} \tag{2.5}$$

Subject to the constraint $t \leq s/2$ ("t" is the thickness of sample and "s" is the distance between probes of the sample). The sheet resistance characterizes thin semiconductor sheets or layers, such as diffused or ion-implanted layers, epitaxial films, polycrystalline layers, and metallic conductors. The sheet resistance is a measure of the resistivity averaged over the sample thickness.
In this study I performed 4-probe measurements at PDI to measure the TiN resistivity.

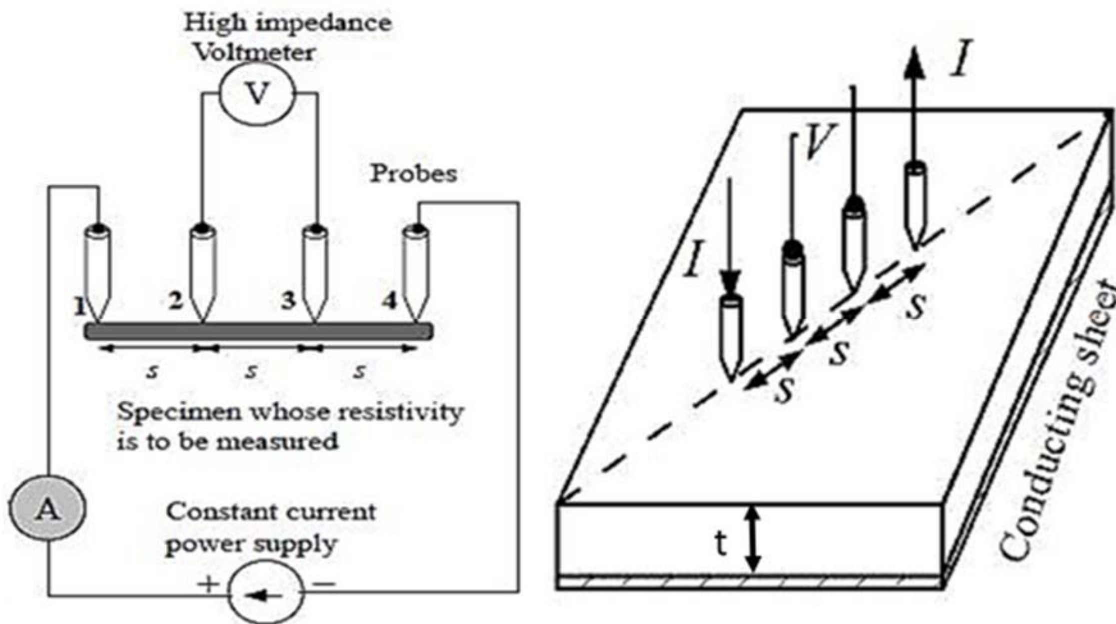

Figure 2.17: The schematic 4-probe measurement apparatus showing the arrangements of probes that measure voltage (V) and supply current (A) to the surface of the crystal. [Adapted from quora.com]

Chapter 3

3. Heteroepitaxial growth of InGaN thin-films on Si(111)

InGaN has very unique properties such as high near band edge absorption, high carrier mobility, surface electron accumulation, and superior radiation resistance. But what puts this material in high demand for many industrial applications is its wide tunability of the band gap which spans from 0.7 to 3.4 eV.

Table 3.1: Some characteristics of InN and GaN

	Parameter	InN	GaN
Lattice constant	a	3.5377 Å	3.1884 Å
Lattice constant	c	5.7037 Å	5.1850 Å
Electron mobility	μ_e	2050 $cm^2/V \cdot s$	900 $cm^2/V \cdot s$
Density	ρ	6.81 g/cm^3	6.15 g/cm^3
Electron effective mass	m_e/m_0	0.07	0.20
Band-gap at 300 K	E_g	0.64-0.70 eV	3.45 eV

In this chapter, heteroepitaxial growth of InGaN thin-films on Si(111) with focus on the central composition is discussed. The fundamental aspects of low-temperature InGaN growth is investigated. The growth mechanism and the influence of different growth parameters, in particular, the influence of III-N ratio on the growth mechanism, morphology, and composition of InGaN thin-films is studied. The existence of metal droplets on the growth surface and relevant role of droplets in determining the InGaN growth dynamics, by analyzing the adatoms and the kinetics of incorporation in the presence of droplets, are exclusively discussed and related mathematical models are proposed. The important role of Vapor-Liquid-Solid (VLS) growth mode that takes place under the droplets in the InGaN epilayer growth is explained and the In incorporation suppression by metal droplets during the growth of InGaN layers is discussed.

Moreover, Raman spectroscopy of InGaN is briefly discussed and by filling the gap of data in the central composition range, the Raman spectra for whole InGaN composition range is calibrated. In this way, a useful reference for the determination of composition of this alloy is provided.
At the end of the chapter, the three different growth regimes: N-rich, Metal-rich and Intermediate regimes are compared. It is shown by accurately controlling the growth parameters, it's possible to grow flat single crystalline $In_{0.5}Ga_{0.5}N$ film on Si(111) substrate which is highly demanded but is considered difficult to reach due to high tendency of phase separation in the central composition range.

3.1 Choosing the substrate

Substrates for different applications must meet stringent requirements related to crystal structure and orientation, lattice constant, thermal expansion coefficient, dielectric constants, and electrical conductivity. In many of these attributes, substrate technologies employed for III-N-based UV optoelectronics are still far from ideal. Ideal substrates allow lattice-matching or strain balancing of overlying epitaxially grown device layers, supporting pseudomorphic growth with low defect densities.[29] The lowest possible lattice mismatch (to minimize the creation of dislocations and defects), chemical stability, similarity in thermal expansion coefficient, low inter-diffusion with the epilayers, good electrical conductivity, and finally a low price for mass production are of the most important properties should be taken into account for choosing the substrate. The most common substrates for the growth of GaN are shown in Table 3.2.

Table 3.2: Principal parameters of conventional substrates used to grow GaN, and their lattice mismatch respect to GaN

Substr.	Crystal Struct.	Lattice Parameters a [Å]	c [Å]	T. Exp. Coeff. $[10^{-6} \cdot K^{-1}]$	Lattice Mismatch
Al_2O_3	Hexagonal	0.4765	1.2982	7.5	16.0%
4H-SiC	Hexagonal	0.3073	1.0053	4.5	3.1%
6H-SiC	Hexagonal	0.3081	1.5117	3.0	3.1%
Si	Diamond	0.5431		2.6	16.9%
GaN	Wurtzite	0.3189	0.5185	5.6	0%

Sapphire is one of the most used substrates for epitaxial growth of semiconductors since high-quality and big wafers are available with reasonable prices and good physical properties, even if the great lattice mismatch is a serious obstacle. However, due to its poor conductivity, contacts must be placed on the top of the substrate and this limits the device design.
Silicon carbide presents the lowest mismatch (excluding GaN templates) and good thermal and electrical conductivity. However, its high price limits its applications. (SiC is not used in this thesis)
GaN templates are the optimal choice for the growth of GaN/InGaN, but its high price and unavailability of high-quality templates in the market limits its application.
Silicon substrates are the principal choice due to good physical properties and its availability in reasonable price, high-quality and big sizes thanks to Czochralski crystal growth process.
InGaN-based optoelectronic devices are mainly grown on expensive GaN/sapphire templates. For their further commercialization the transfer of high quality InGaN layers to cheaper and/or more flexible substrates is highly desired.[32] Since the current microelectronic technology is stablished based on Si, the growth of III-N semiconductors on Si wafers allows for low cost and large mass production. The device design and processing requires compact, and chemically uniform InGaN layers grown directly on Si[9] which have the potential to qualitatively extend many application fields such as InGaN/Si tandem solar cells[12], solar driven photoelectrochemical water splitting[25], and integrated telecom devices.[62]
Considering the above mentioned advantages of direct integration of III-nitrides on Si substrates, in this thesis, Si(111) is used as the substrate to grow InGaN thin-films. In following I explain that before starting the growth, a simple substrate preparation step is required to improve the crystal quality of InGaN.

3.2 Substrate preparation

It is known that the growth of InGaN directly on Si, due to inevitable formation of amorphous SiN interlayer, proceeds under weak epitaxial constraint (weak epilayer- substrate interaction) resulting

in 3D growth mode[32,33]. To overcome this problem, it is shown that a nitridation process at high temperatures (before starting the growth) can improve the epitaxial relation between (In)GaN grown layers and Si(111) substrate. [19,35]

So, also here, I follow the same nitridation procedure. Prior to growth, the growth chamber is pumped down to 5×10^{-10} Torr. The native silicon oxide is removed from the surface by a thermal annealing at 900°C for 20 min in vacuum. After removing native oxide layers from silicon surface at high temperature under UHV condition, the surface atoms rearrange into a more energetically stable configuration called the 7×7 reconstruction. STM and schematic images of Si surface after 7×7 reconstruction is shown in Figure 3.1.

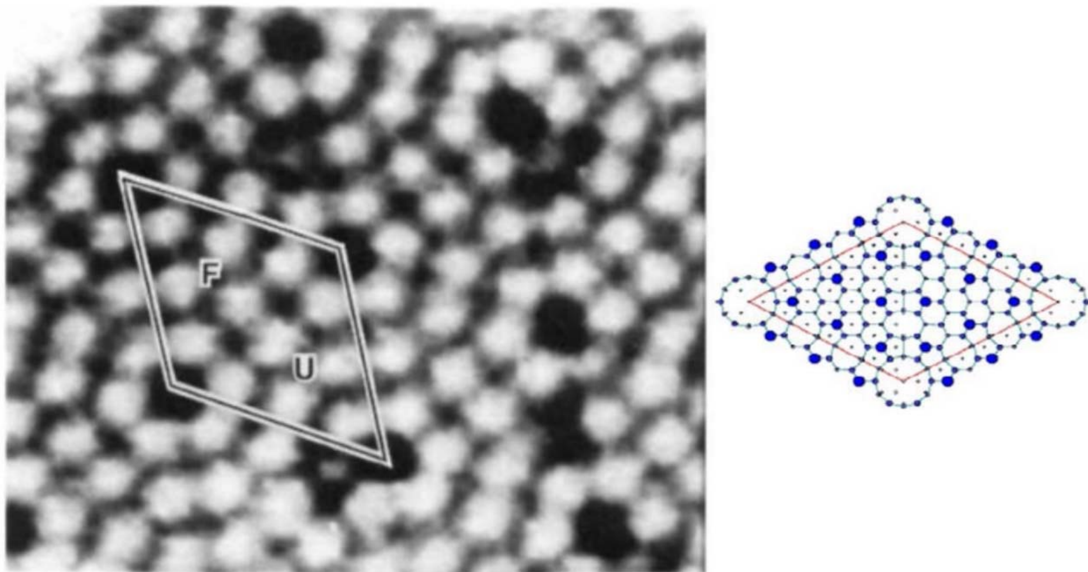

Figure 3.1: STM[63] (on the left) and schematic (on the right) images of Si 7×7 surface reconstruction

Si(111) 7×7 surface reconstruction (Figure 3.2(a)) is observed using RHEED, which is also used to calibrate the substrate temperature by using the 7×7 to 1×1 Si transition temperature (860 °C)[64]. Due to high lattice miss match between InGaN and Si(111) (8% respect to InN and 17% respect to GaN), the direct growth of InGaN on Si(111) leads to polycrystalline InGaN film (Figure 3.2(b)). Hence, prior to the growth, the substrate is exposed to the nitrogen plasma with a flux of 0.9 sccm (standard cubic centimeter per minute) and RF power of 360 W at 850 °C for 5

minutes to make very narrow Silicon Nitride layer (a few nanometers). This procedure was previously established to grow high quality GaN and InGaN epilayers on Si[9,35]. The RHEED pattern (Figure 3.2(c)) indicates the formation of amorphous Silicon Nitride which is consistent with TEM results (Figure 3.3) reported by other groups[19,35]. InGaN layer growth is performed at 450 °C with the same nitrogen-plasma condition and, In/Ga flux equal to one and III/V ratio smaller than one (slightly N-rich). The working pressure is 1.1×10^{-5} Torr with the injection of nitrogen plasma.

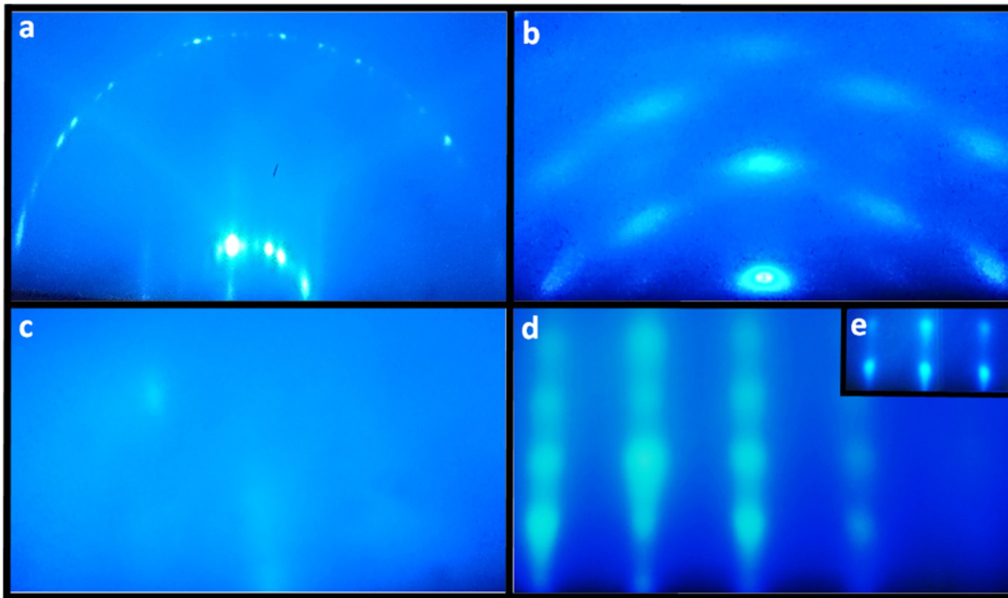

Figure 3.2: RHEED patterns of: (a) Si(111) 7×7 reconstruction indicating successful oxide removal from the surface after heating up to 900°C. (b) InGaN polycrystalline film grown directly on Silicon without nitridation step, after 90 minutes. (c) Amorphous Silicon nitride layer made on Silicon surface just after nitridatating at 850°C for 5 minutes. (d) and (e) Single crystalline InGaN grown on Nitridated surface, after 90 minutes, along the azimutes $\langle 2\bar{1}\bar{1}0 \rangle$and $\langle 10\bar{1}0 \rangle$ respectively.

Figure 3.2(d) and (e), are the RHEED patterns showing single crystalline wurtzite InGaN films grown on silicon nitride layers formed on Si(111) substrates with presumably (it will be proved later by XRD) maintaining the heteroepitaxial relation (InGaN [0001] || Si [111] and InGaN $[\bar{1}\bar{1}20]$ || Si $[1\bar{1}0]$) between epilayers and substrate.

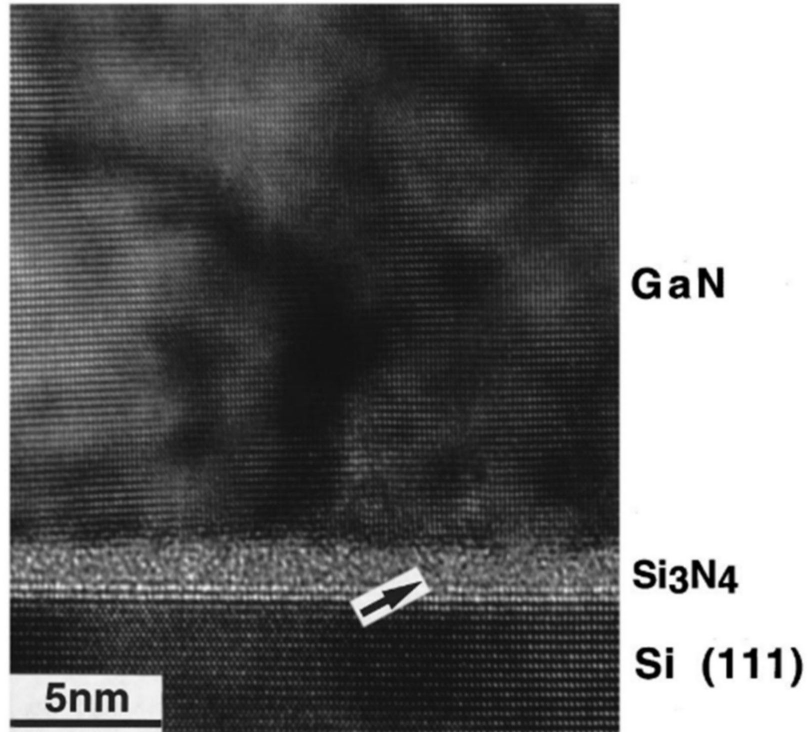

Figure 3.3: HRTEM image showing wurtzite GaN grown on amorphous Si_3N_4 buffer layer on Si(111) substrate. [35]

The cross section SEM image of InGaN thin-film grown on Si(111) is shown in Figure 3.4.

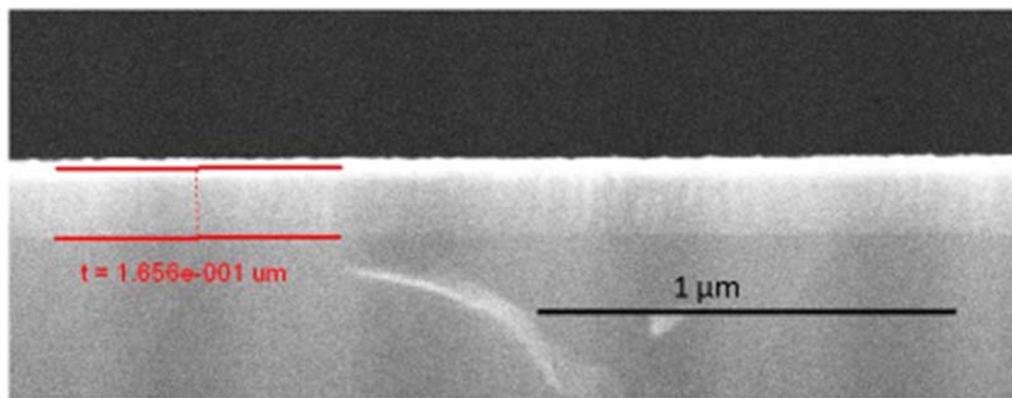

Figure 3.4: Cross section SEM of InGaN thin-film grown on Si(111)

3.3 Droplet effects on growth rate

At low growth temperatures, metal-rich conditions easily lead to the formation of droplets on the surface which affect the film quality[17] and that are difficult to remove metal droplets by thermal treatment, because the In-N dissociation temperature is lower than the onset temperature for the evaporation of In from the In droplets on the InGaN surface[26]. This has been shown to be detrimental to material properties and a major drawback for device applications[65] although there was no clear explanation reported for these phenomena. At higher substrate temperatures, an intermediate Ga-rich regime is observed, leading to smooth droplet-free surfaces[65]. Several method to overcome such drawback have been proposed, based on the alternating sequence of metal-rich and nitrogen-rich conditions at low temperature to take profit of the higher mobility of metal adatoms in metal-rich conditions and to eliminate the metal droplets that form on the surface during the atomic nitrogen irradiation in absence of metal flux.[21,66,67]

In order to study the droplets role in determining growth dynamics in this study, several InGaN samples (I1-I11 as reported in Table 3.3) are prepared using the same preparation and growth condition as explained at the beginning of this chapter, but with different III/V ratio. After growth, the samples are cooled down to room temperature and taken out of the MBE chamber for further characterization. XRD was employed to examine the sample composition. The surface morphology was investigated by both optical microscopy as well as scanning electron microscopy (SEM) using a secondary electron detector. The layer thickness, and in turn the growth rate, was determined via cross-section SEM images of the samples.

Table 3.3: Metal flux (In + Ga with one to one ratio), growth time, and growth rate of samples

Sample	Metal flux (10^{14} atoms $cm^{-2}s^{-1}$)	Growth time (mins)	Metal dose (10^{16} atoms cm^{-2})	Growth rate (ML/s)
I1	0.39	120	28	0.0401
I2	0.78	120	56	0.0740
I3	0.98	120	71	0.1028
I4	1.17	120	84	0.0900
I5	1.41	90	76	0.0802

I6	1.96	45	53	0.0843
I7	2.94	45	79	0.0813
I8	2.94	90	158	0.0874
I9	2.94	150	264	0.1028
I10	3.92	60	141	0.0637
I11	7.83	90	423	0.0510

Figure 3.5(a-e) show the optical microscopy and SEM images taken from samples with different metal fluxes. Epilayer surfaces are smooth and free of metal droplets when the metal flux is not too high, that is, when the growth presumably takes place in slightly N-rich conditions (excess of active N atoms compared to metal atoms reaching the surface).

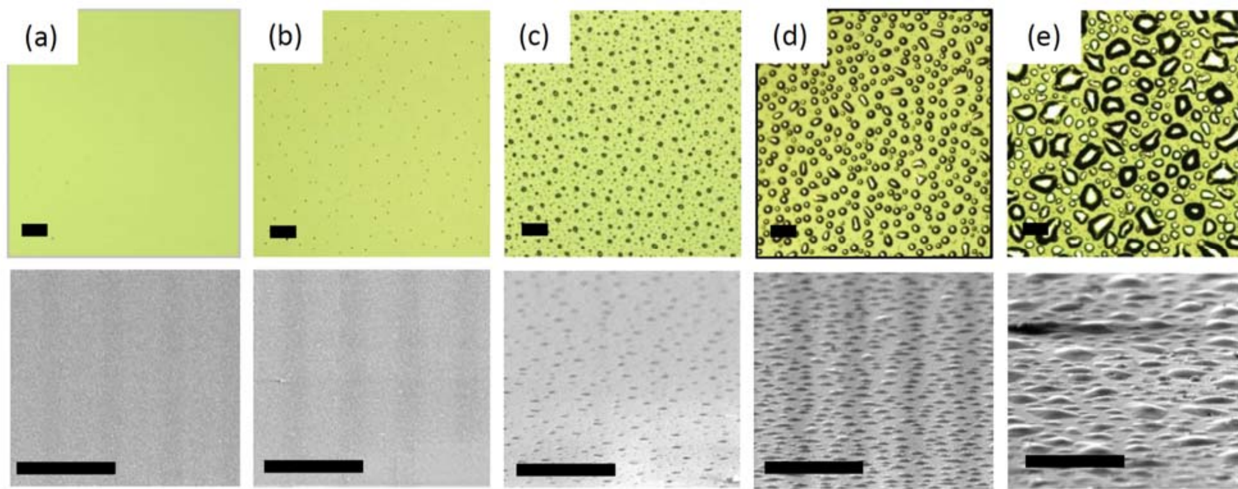

Figure 3.5: (top) Optical Microscope and (bottom) related SEM images (taken at an angle of 70° respect to the sample) of InGaN samples grown at 450 °C under different metal fluxes, from left to right: (a) 0.39×10^{14}, (b) 0.98×10^{14}, (c) 1.41×10^{14}, (d) 3.92×10^{14}, (e) 7.83×10^{14} atoms cm^{-2} s^{-1}. Black line length in all the images is 100 µm.

In this regime the growth rate is proportional to the impinging metal flux (green shaded area in Fig. 2). The droplets start to appear as the ratio of metal flux vs nitrogen flux exceeds the equilibrium point, which in our experiments is $F_T = 0.98 \times 10^{14}$ atoms cm^{-2} s^{-1}. The creation of metal droplets in the metal-rich conditions has been already reported in case of GaN and in general

in the growth of InGaN grown at low temperature.[17,21,22,26,66,68–70]. Here we observed that as the droplets start to appear on the surface, a marked decrease in growth rate (see Figure 3.6) occurs. The growth rate depends strongly on the metal flux, decreasing as the flux increases, and this effect starts as soon as droplets are formed on the surface (Figure 3.6). It is worth mentioning that the total amount of metal stored in the droplets after the growth corresponds, within 20% accuracy, to the total dose of metal deposited, once the fraction incorporated in the InGaN crystal has been subtracted.

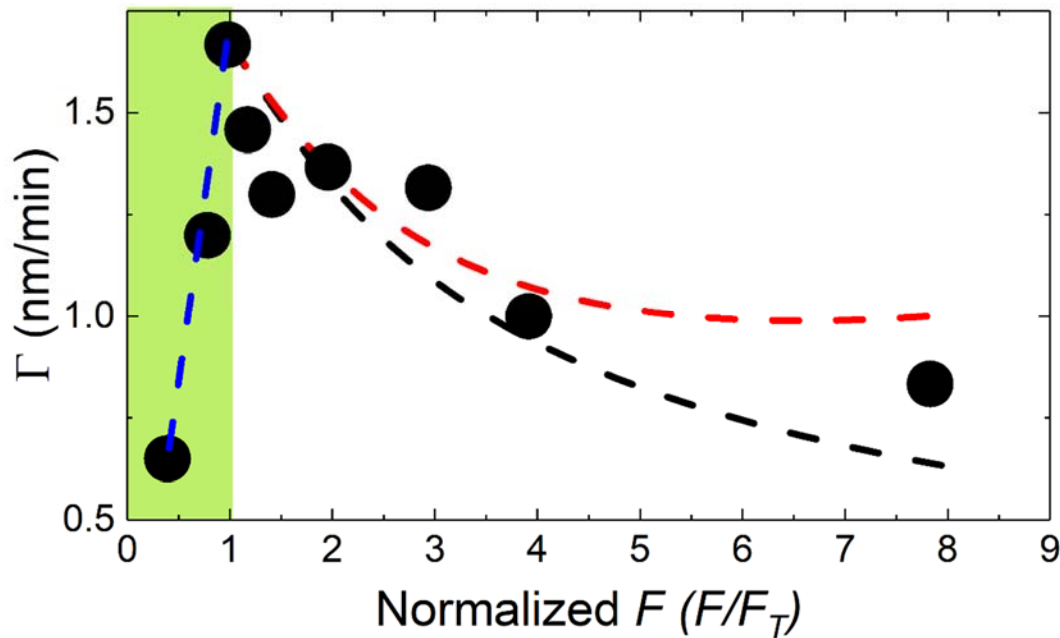

Figure 3.6: Average growth rate as a function of metal flux F normalized by F_T. Black circles represent the experimental data. The dashed lines correspond to the model predictions: Initial linear dependence in absence of droplets (blue), Γ (red) and R_S (black). Model parameters are $R_U = R_S(F_T)$, $\chi_M = 0.6$, $\Gamma_{MAX} = 1.7$ nm/min, $\sigma\rho_0/\mu = 3$, the critical exponent p = 1.6. The model prediction calculated including VLS processes in the model (red curve) give a better description (χ^2= 0.107) respect to the one calculated excluding VLS processes (black curve, χ^2= 0.135).

However, it is found that in presence of droplets, by increasing the time of growth (at the same metal/N ratio), the growth rate increases (Figure 3.8(b)).

To understand the observed behavior, we carefully consider the metal adatom dynamics during the growth in the transition between the N-rich and the metal-rich regimes. Among all growth parameters, the III/N ratio is one of the key points to improve the surface structure and morphology of the grown film. Based on this ratio, two different morphologies have been observed. One is the smooth epilayer structure which is achieved in metal-rich and lightly N-rich conditions and the other is the so-called nano-columnar structure which will appear in case of N-rich growth[28]. Nitride semiconductor films grown with even a slight excess of N during growth (N-stable conditions) display a rough surface morphology with a columnar structure initiated by the formation of stacking faults[27]. This can be explained considering the very different diffusivity for Ga and N adatoms on the surface. While Ga is very mobile at typical growth temperatures, the diffusion of N is slower by orders of magnitude. The presence of excess N strongly increases the Ga diffusion barrier. It has been calculated that the diffusion barrier for Ga adatoms on N-rich surfaces is as high as 1.8 eV, whereas it is only 0.4 eV when the growth is carried out on a Ga-saturated surface. Thus, N-rich growth leads to very low adatom mobility and to an undesired kinetically induced roughening of the surface[71]. GaN growth by PA-MBE is commonly carried out under metal-rich conditions. But it must not be forgotten that in metal-rich regimes where there is the accumulation of metal atoms and creation of droplets on the surface, these very mobile metal adatoms on the surface can join metal droplets instead of participating in the crystal growth.
We observe that the decrease in the growth rate is always accompanied by the presence of metal droplets on the sample surface after the growth. The growth rate decreases more and more with the increase of the metal flux and so does the density and volume of droplets, though the N flux is unchanged. This is in marked contrast to the common assumption that the growth rate under metal rich conditions is determined by the N flux. Hence, the common N flux calibration procedure under metal-rich conditions must be reconsidered. The droplets thus should play a fundamental role in the change of metal adatom incorporation dynamics. As soon as the number of metal atoms exceeds the critical density for droplet formation, the metal atoms start to form droplets and accumulate in them. The presence of droplets on the surface establishes a depletion channel for the metal adatom density on the growth surface, as metal adatoms can be efficiently captured by the droplets. This depletion channel is in competition with the N-driven metal adatom incorporation into the InGaN crystal. This leads, on one hand, to a reduction of the metal adatom incorporation rate into the crystal in the regions not covered by the droplets. On the other hand,

the presence of liquid metal droplets on the surface should allow for the VLS growth of InGaN material under the droplets themselves, via direct incorporation of nitrogen. In summary, three possible processes are available to the metal adatom on the growing InGaN surface in the presence of droplets (see Figure 3.7):

1) Incorporation of metal adatom into the crystal by binding to a N active site on the droplet-free surface
2) Metal adatom attachment to a droplet
3) Desorption

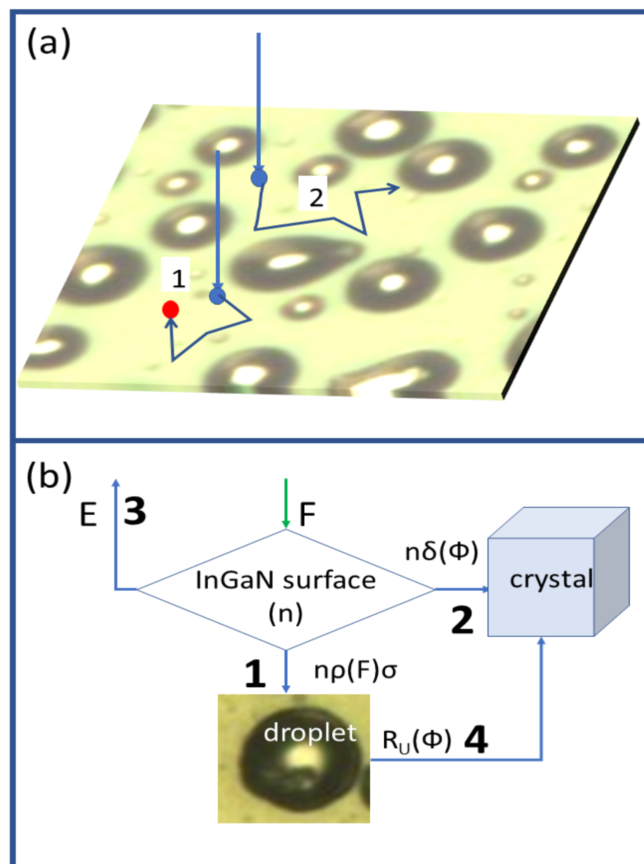

Figure 3.7: (a) Available metal adatom processes. Process 1 leads to metal droplet attachment. Process 2 leads to incorporation into the growing crystal (indicated by the red dot). (b) Schematics of the metal adatom rate equation model highlighting the four available channels for the metal adatoms: 1) droplet attachment; 2) crystal incorporation; 3) desorption; 4) VLS crystal growth under the droplet.

In addition, the metal adatoms incorporated in the droplets can be incorporated in the crystal due to VLS (Vapor-Liquid-Solid) mechanism[72] under the droplet by direct N flux into the droplet (process 4 in Figure 3.7). In general, the growth of a crystal through direct adsorption of a gas phase on to a solid surface is very slow. However the VLS mechanism circumvents this by introducing a catalytic liquid alloy phase which can rapidly adsorb a vapor to supersaturation and from which crystal growth can subsequently occur from nucleated seeds at the liquid–solid interface. VLS growth mechanism is known mainly for the growth of one-dimensional structures, such as NWs, where a catalytic liquid alloy phase rapidly adsorbs the adatoms, and through the direct adsorption of gas phase, accelerate the growth rate at the liquid–solid interface. However, it can also happen under the metal droplets during the growth of thin-films. It is possible then to model the combined effect of the three processes (which are mentioned in Figure 3.7(b)) as a set of rate equations for the metal adatom density *n* and VLS growth rate. The first equation (3.1) describes the kinetics of the metal adatom density *n*, determined by the combined effect of external metal flux, incorporation in to the crystal and attachment to the droplets:

$$\frac{dn}{dt} = F - E - n\delta\left(\frac{\Phi}{F}\right) - n\sigma\varrho(F) \tag{3.1}$$

where *F* is the total (In plus Ga) metal flux, Φ is the active N flux, *E* is the desorption flux, $\delta(\Phi/F)$ the incorporation probability into the crystal on the droplet free surface, which depends on the ratio between active N flux Φ and the metal flux *F*. $\delta(\Phi/F)$ is proportional to the probability, for a metal adatom, to find an active N site for binding. $\rho(F)$ the droplet density and σ the droplet capture cross section. At low temperature in MBE conditions the metal desorption flux is close to zero ($E = 0$). Therefore in the steady state condition, Eq. (3.1) leads to the solution for *n* in Eq. (3.2)

$$n = F \frac{1}{\delta\left(\frac{\Phi}{F}\right) + \sigma\rho} \tag{3.2}$$

And consequently, the bulk growth rate per unit surface area (process 2) R_S that takes place in the regions of the sample where there are no droplets is:

(3.3)

$$R_S(F,\Phi) = n\delta\left(\frac{\Phi}{F}\right) = F\frac{1}{1+\frac{\sigma\varrho_o F^p}{\delta\left(\frac{\Phi}{F}\right)}}$$

Here we explicitly used the expected dependence of the droplet density on the metal flux $\rho(F)=\rho_0 F^p$ [73]. p is the critical exponent for droplet nucleation, whose value is determined by the physics of the nucleation process. As droplet formation happens in the presence of a leak channel for the adatoms, that is the bulk incorporation, we expect to be in the regime of incomplete condensation. In this regime $p > 1$ values are expected. It is worth mentioning that in the N-rich region, where the density of droplets is equal to zero (green region in Fig. 2), Eq. (3.4) reduces to:

(3.4)

$$R_S(F,\Phi) = F$$

In N-rich conditions the predicted InGaN growth rate linearly follows the metal flux, as observed. When the growth turns to metal-rich conditions, as soon as the adatom density n overcomes the critical density for droplet formation, the second depletion channel opens for the metal adatoms (in addition to the incorporation), thus leading to a rapid depletion of the adatom density n. The depletion of n leads a reduction of R_S in the area between the droplets. The effect becomes larger as the metal flux increases, as the droplet density, and thus in turn the metal adatom capture probability by the droplets, increases with F. The transition between the two growth modes takes place around $F_T = 0.98 \times 10^{14}$ atoms $cm^{-2}s^{-1}$.

However, under the droplets, VLS growth can take place, due to the incorporation of nitrogen molecules into the droplets by direct impingement[74]. An additional nitrogen incorporation

mechanism in to the droplet, with subsequent VLS growth at the basis of the droplet, has been identified by means of molecular dynamics simulations by Kawamura et al.[75] and related to N migration on stable InGaN surfaces. The growth rate per unit area under the droplet is $R_U(\Phi)$ and depends on the nitrogen flux Φ, the incorporation probability of N into the droplet and the growth rate at the liquid-solid interface. The total growth rate is therefore the sum of the two contributions, that is the growth rate R_S in the droplet free areas and R_U under the droplets, whose relevance is given by the surface area covered by the droplets (see Figure 3.8(a)). The total growth rate per unit area is then:

(3.5)

$$R_T(F,\Phi,\tau) = (1-\chi)R_S + \chi R_U = R_S + \chi(R_U - R_S)$$

where χ is the relative area covered by the droplets. This depends on the total amount of metal stored in the droplet ensemble and on the droplet density ρ. As long as the droplets do not touch ($\chi \ll 1$), the dependence of χ on the metal flux F, the deposition time τ and the droplet density ρ is:

(3.6)

$$\chi(\tau) = \gamma \left[\frac{(F-R_S)\tau}{\rho}\right]^{\frac{2}{3}} \qquad \rho = \gamma \varrho_0^{\frac{1}{3}} \left(1 - \frac{1}{1 + \frac{\sigma \varrho_o F^p}{\delta\left(\frac{\Phi}{F}\right)}}\right)^{\frac{2}{3}} F^{\frac{2+p}{3}} \tau^{\frac{2}{3}}$$

where γ is a normalization constant which can be derived from experiments by equating the Eq. (3.6) predictions with the observed χ at maximum metal flux. $(F - R_S)\tau$ is the total metal quantity that is stored in the droplet ensemble after the growth time τ. It corresponds to the total metal dose deposited on the substrate minus the amount incorporated in the crystal between the droplets (R_S). We did not consider the decrease in the metal dose available for droplet formation due to the crystallization under the droplet as it is a small correction for $\chi \ll 1$ and it adds complexity to the model. It is worth mentioning that Eq. (3.6) is not valid for long growth times, when $\chi \rightarrow 1$ and the amount of growth proceeding via VLS under the droplets becomes relevant. By combining

equations (3.3)-(3.6) we find the dependence of the total growth rate, at time τ, per unit area to be given by the relation

(3.7)

$$R_T = F\,\frac{1}{1+\frac{\sigma\varrho_o F^p}{\delta(\Phi/F)}} + \gamma\left[\varrho_0^{1/3}\left(R_U(\Phi) - F\,\frac{1}{1+\frac{\sigma\varrho_o F^p}{\delta(\Phi/F)}}\right)\left(1-\frac{1}{1+\frac{\sigma\varrho_o F^p}{\delta(\Phi/F)}}\right)^{2/3} F^{\frac{2+p}{3}}\right]\tau^{2/3}$$

The total growth rate R_T *versus* time dependence is introduced by the change, with the growth time, of the area covered by the droplets. The exact $\tau^{2/3}$ dependence is related to the invariance of the wetting angle of the droplet with its size. In the extreme case of a surface covered by closely arranged droplets, the growth rate will be determined by the N flux only, that is $R_T \propto \Phi$. It is worth mentioning that the growth progressively shifts towards the VLS dominated mode as the growth time increases in metal-rich conditions.

From equation (3.7) the dependence on time of the average growth rate Γ is

(3.8)

$$\Gamma = R_S + \frac{3\gamma}{5}B(F,\Phi)\tau^{\frac{2}{3}}$$

where $B(F,\Phi)$ indicates the complex formula encased in the square brackets in Eq. (3.7). The model predictions, using Eq. (3.7) and (3.8), are reported in Figure 3.6. After the initial linear dependence on F, the predicted curve shows a clear decrease in the growth rate. The good agreement of the model predictions based on the dependence of R_S on F (black curve) indicates that the main factor determining the reduction of the growth rate is the decrease in the adatom density n caused by the opening of the droplet depletion channel. The critical exponent extracted from the model is $p = 1.6$. The observation of an exponent $p > 1$ is the outcome of the droplet nucleation in the regime of incomplete condensation. This is to be expected since in presence of nitrogen, a fraction of the deposited metal flux is incorporated into the crystal, and therefore cannot

contribute to droplet nucleation or to the increase in volume of existing droplets. We find that the probability for a metal adatom to attach to a forming droplet is three times larger with respect to being incorporated in the growing crystal at F_T ($\sigma\rho_0 = 3\delta$). This significant difference in incorporation probability leads to the observed fast decrease of the average growth velocity and its lack of recovery even at high F. Even when VLS growth under the droplet is considered (red curve in Figure 3.6), R_T still decreases with the increasing metal flux, although a sizeable decrease in the curve slope with F, eventually reaching a plateau at high metal fluxes, is clearly present. The VLS growth mode dominates the dynamics when the droplet coverage reaches a sizeable percentage of the surface. According to our experimental observations, the maximum coverage in our samples is $\chi_M = 0.6$ (sample I11, see Table 3.3). One of fitting parameter of the model is the growth rate per unit area under the droplets (R_U). By fitting procedure, we find that R_U is equal, at F_T, to R_S. This suggests that the incorporation rate of N into the droplets and the InGaN surface at the growth temperature of 450 °C and F_T are equivalent.

The model predicts a recovery of the growth rate as the growth time increases, with a $\tau^{2/3}$ dependence. This is due to the increase of the area covered by the droplets whose outcome is the increase in relevance of the VLS mode. To test this expected phenomenon we grew three samples, at $F = 2.94 \times 10^{14}$ atoms cm^{-2}s^{-1}, with different growth times (see Figure 3.8). In this sample series, a clear dependence of the average growth time is clearly observed. The behavior of Γ when τ increases follows the predictions of Eq. (3.8), thus conforming the model predictions that in the metal-rich zone the growth is increasingly dominated by the VLS mode in the regions covered by the droplets. The schematic of crystal growth under the metal droplets through VLS mechanism is shown in Figure 3.9.

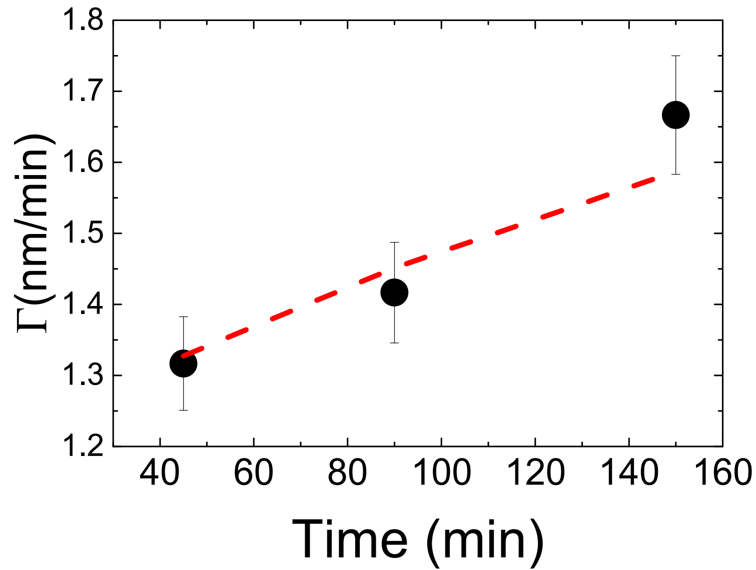

Figure 3.8: Observed dependence of average growth rate from growth time (black dots). The dashed line represents the model predictions [Eq. (3.8)]. Here R_C = 67 nm/h and $3\gamma B/5$ = 15 $nm/h^{1/3}$. Metal flux used in the growth: F = 2.94× 10^{14} atoms $cm^{-2}s^{-1}$.

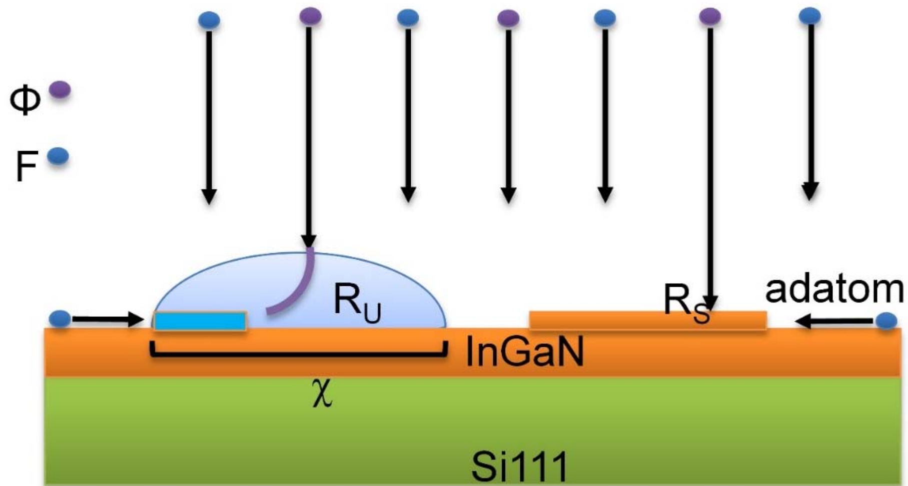

Figure 3.9: Schematic of crystal growth under and between the metal droplets.

3.4 Calibration of Raman spectroscopy for InGaN in the central composition range

The substitution of In and Ga atoms in InGaN alloys has a considerable influence on optical and electronical properties of the material since there is a large difference between the bandgap of InN (0.7 eV)[76] and GaN (3.42 eV).[1] For this reason, the compositional characterization of InGaN is of the great importance.

XRD and photoluminescence have been used as the main characterization methods to define the composition of InGaN alloys[77,78]. However, there are some limitations, especially in case of PL which is only useable for very high quality InGaN (grown at elevated temperatures above 650 °C)[79]. XRD is very robust, but it is unable to probe locally with a resolution better than one micrometer unless using a synchrotron source, hence gives an average of the total scanned area.

These limitations can be overcome by using Raman spectroscopy, which is a non-destructive method that gives the possibility to probe the sample locally with a lab-scale compatible equipment. Moreover, this method is very fast and simpler to interpret than PL and XRD to determine the In amount in the InGaN alloys. For example the interpretation of PL can be complicated by the diffusion of the photogenerated carriers.

In the literature there are already studies on the determination of composition of InGaN by Raman spectroscopy, and several authors[80–84] addressed the interpretation of the Raman spectra, for example in terms of polarization response and resonance effects. However, these works lack of data in the middle composition range (between 30% and 65% In).

Obtaining $In_xGa_{1-x}N$ crystals with high In amount is difficult, as a result of low dissociation temperature of InN and high equilibrium vapor pressure of nitrogen. The different binding energies of In-N and Ga-N are reflected in the different decomposition temperatures[16]. Low-temperature growth has been used to avoid it.[19–22]. However, in low-temperature growth the formation of metal droplets on the surface drastically reduces the Indium incorporation in the crystal[17,85] and causes a vertical compositional gradient.[17] I have previously shown[86] the effect of (In+Ga)/N ratio on the formation of metal droplets and consequently depleting metal adatoms on the surface.

By growing InGaN in the low-temperature regime and by a careful control of the growth parameters to avoid formation of metal droplets on the surface, a good composition control is achievable. I used such high quality InGaN layers to fill the gap in Raman spectroscopy data in

the middle composition range, thus providing a useful reference for the determination of the composition of this alloy by Raman spectroscopy.

For this reason, the composition of the layers is determined by XRD using a PANalytical X'Pert PRO high-resolution diffractometer. A hybrid mirror and 2-bounce Ge monochromator selected the Kα1 line, $\lambda = 0.15406$ nm, of the Cu anode. A high-precision goniometer allowed both translational (x, y and z) and rotational (incidence angle ω, diffraction angle 2θ, sample rotation φ and sample tilt χ) degrees of freedom. A three-bounce Ge monochromator placed in front of the detector was used as an analyser crystal, in order to obtain high precision in 2θ and to reject fluorescence from the sample. To assess the composition, a ω–2θ scan through the InGaN(0002) Bragg peak was carried out, using the Si(111) peak from the substrate as a reference. Asymmetric reciprocal space maps demonstrated that the material was fully relaxed and maintained an epitaxial relationship with the substrate.

Raman spectra were collected at room temperature by a T64000 Jobin Yvon spectrometer in a single spectrometer configuration. The excitation source was a 532 nm laser focused by a 100x 0.90 NA objective with about 1 mW excitation power and ~700 nm spot size on the sample. The power density was checked not to introduce changes in the spectrum due to lowering of the bands due to laser heating. The configuration is in backscattering and the collection is kept without polarizers. Typical Raman spectra can be found in Figure 3.10, where it is possible to observe the presence of the contribution of the epilayers together with the signal from the Si substrate.

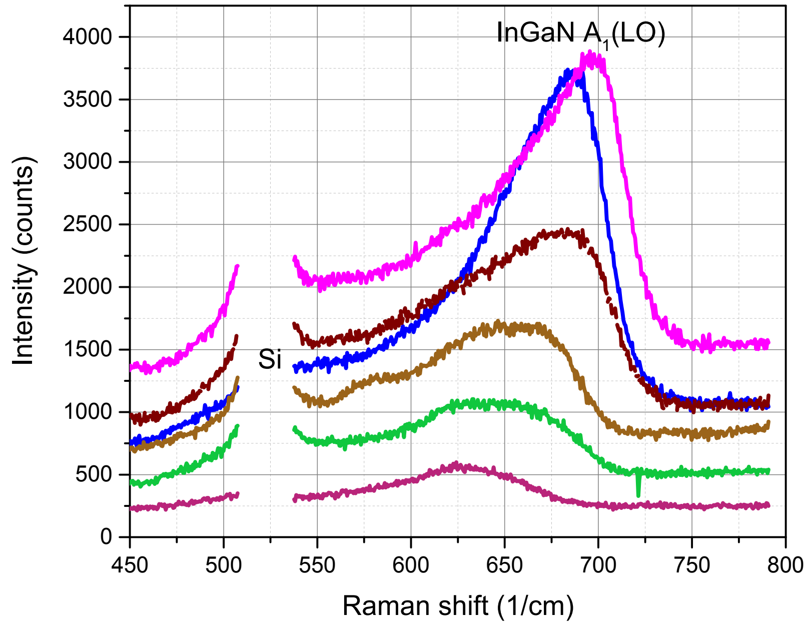

Figure 3.10: Typical A_1 LO peaks of $In_xGa_{1-x}N$ Raman spectra taken from a set of samples with different composition

In Figure 3.11 Raman spectra and XRD, of a set of wurtzite $In_xGa_{1-x}N$ epilayers with Indium fractions ranging from x=0 up to 0.65 are depicted. Except the binary composition (GaN, x=0) which E_2 mode is dominant, in all ternary (InGaN) samples the A_1(LO) mode is the dominant Raman spectra. The position of A_1(LO) peak is characteristic for determining the InGaN composition.

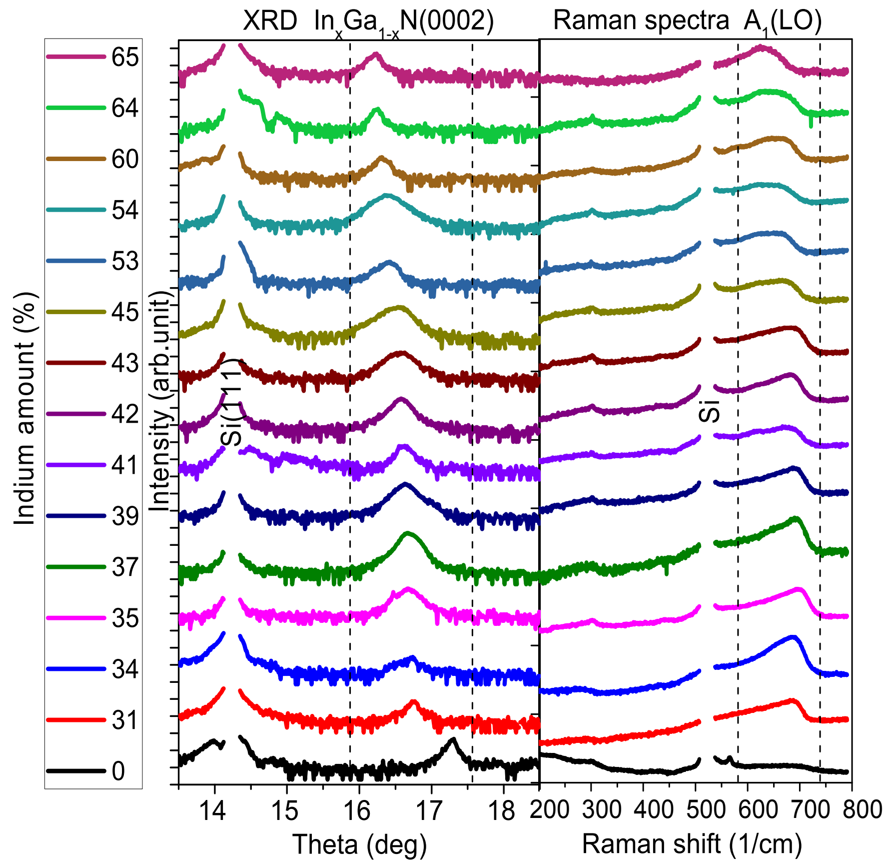

Figure 3.11: Room-temperature Raman spectra and XRD, of a set of wurtzite $In_xGa_{1-x}N$ epilayers grown on Si(111) at 450 °C with Indium fractions ranging from x=0 up to 0.65.

The XRD measurements shown in Figure 3.11 demonstrate a progression to lower θ values as the In content increases, corresponding to an increase in the *c* parameter of the lattice. The mismatch between the in-plane InGaN lattice parameter *a* and the relevant in-plane spacing of the Si(111) surface is very large at about -13% to -17% that no residual strain is expected, and indeed a reciprocal space map around Si(224) and InGaN(1015) for a sample with x = 39% showed full relaxation. This means that the *c* parameter alone can be used in order to ascertain the In content. While XRD itself is a high-precision technique (especially if the substrate can be used as a reference) the accuracy here is limited by the use of a linear interpolation between the lattice parameters of InN and GaN, and by a possible non-uniformity in the deposited material.
Care must be taken therefore to ensure that the micro-Raman laser spot illuminates a representative region of the material. For this reason the same piece of samples which were characterized by XRD, are also used for Raman spectroscopy. Moreover, different spots on these pieces of samples

are examined by micro-Raman to confirm the independency of the results with respect to the position of the laser spot on the samples. Figure 3.11 shows a set of bands in the longitudinal optical region for concentrations ranging from 31% to 65%. The spectra are normalized to maximum amplitude in order to highlight the shape and position of the spectra. These spectra are in the region of the A_1(LO) band of InN and GaN. The E_2 bands, expected around 500 and 550 cm^{-1}, could not be unambiguously detected because of the strong scattering of the silicon background. The main features of the Raman spectra of the InGaN alloys shown in Figure 3.11 could also be affected by the appearance at frequencies lower than A_1 of a shoulder which has been tentatively attributed to a disordered activated B_1-like mode, indicated also as the S-band.

The bands are rather broad, but this is a typical feature of InGaN alloys. The large width of the bands is consistent with the previous results on these alloys in the literature (see for example ref. [Davydov et al.][80]) and it is a result of the fact that the material is a ternary alloy, and therefore due to alloy disorder the selection rules for InN or GaN, requiring a scattering only for the center-zone phonon, are relaxed. This effect is quite evident considering also the asymmetry of the broadening towards low energies. Figure 3.12 shows the full-width at half-maximum (FWHM) of the InGaN LO bands and (0002) Bragg peaks as a function of the In concentration. In case of InGaN (0002) Bragg peaks, although the use of the analyzer crystal removes the broadening of the InGaN peak which arises from misorientation of the (0002) planes with respect to the sample surface (or from the limited lateral crystalline domain size), both vertical and lateral inhomogeneity lead to a broadening of the average diffraction peaks from the material probed by the x-ray beam. The FWHM of both XRD and Raman peaks reach to its maximum where the In concentration is close to 50% (maximum immiscibility of InN and GaN) and reduces by going to lower or higher concentrations.

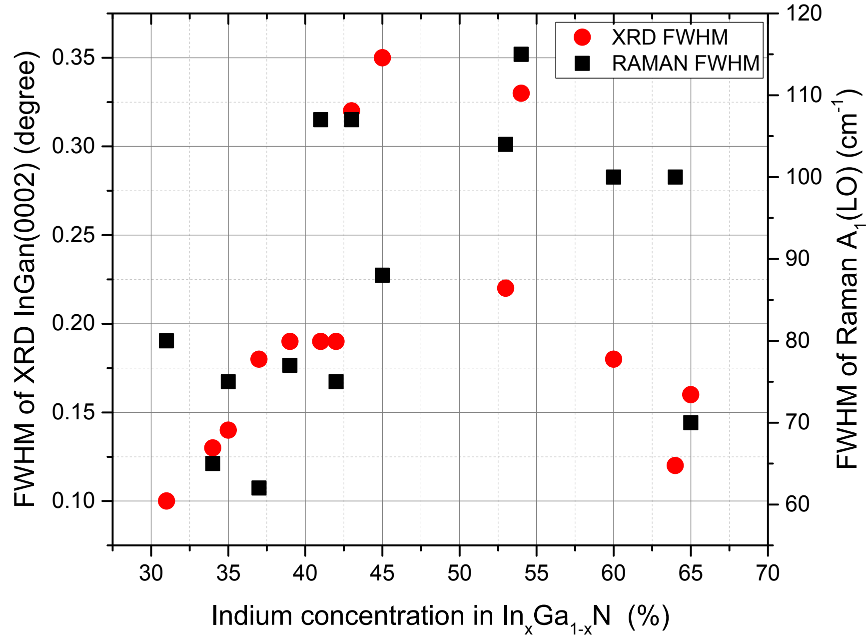

Figure 3.12: FWHM of the LO bands as a function of the In concentration

Although the bands are relatively broad, the composition can be neatly followed by a Polynomial dependence of the maxima with respect to the concentration. Figure 3.13 shows the shift of the A_1 band as a function of the Indium concentration x. In this method we used the centroid (the maximum) of the bands. Notice the uncertainties reported in this plot for the Raman shift do not indicate the FWHM of the bands[82], but rather to the precision in the determination of the maxima. The polynomial fit of the dependence of the Raman A_1(LO) frequency on the In composition, based on the results of this study (central composition range) including the known values of the InN and GaN (GaN is used as a fix point) binary compounds is (see Figure 3.13):

$$\omega_x = (736 - 135x - 24x^2)\ \text{cm}^{-1} \tag{3.9}$$

where x is the Indium concentration in $In_xGa_{1-x}N$ composition. The uncertainty of this calibration for the determination of the relative concentration is around ±5%, which is related to the broadness of the bands. In addition to the linear dependence of A_1(LO) with In fraction, observed experimentally in literature in the case of Ga-rich and In-rich InGaN[81–84] as well as theoretically

predicted by the modified random-element isodisplacement (MREI) model[87], a bowing toward higher frequencies in the middle region is observed in this study. Upward shift of A_1(LO) with respect to predicted values (linear fit) was observed also in other studies[81,82,88] which was attributed to residual compressive strain in the epilayers. However, as it was mentioned earlier, asymmetric reflections in reciprocal space map XRD confirm full relaxation of the epilayers grown in the current study which suggests the previous assumption of linear dependency of A_1(LO) with In fraction in the entire InGaN compositional range must be reconsidered.

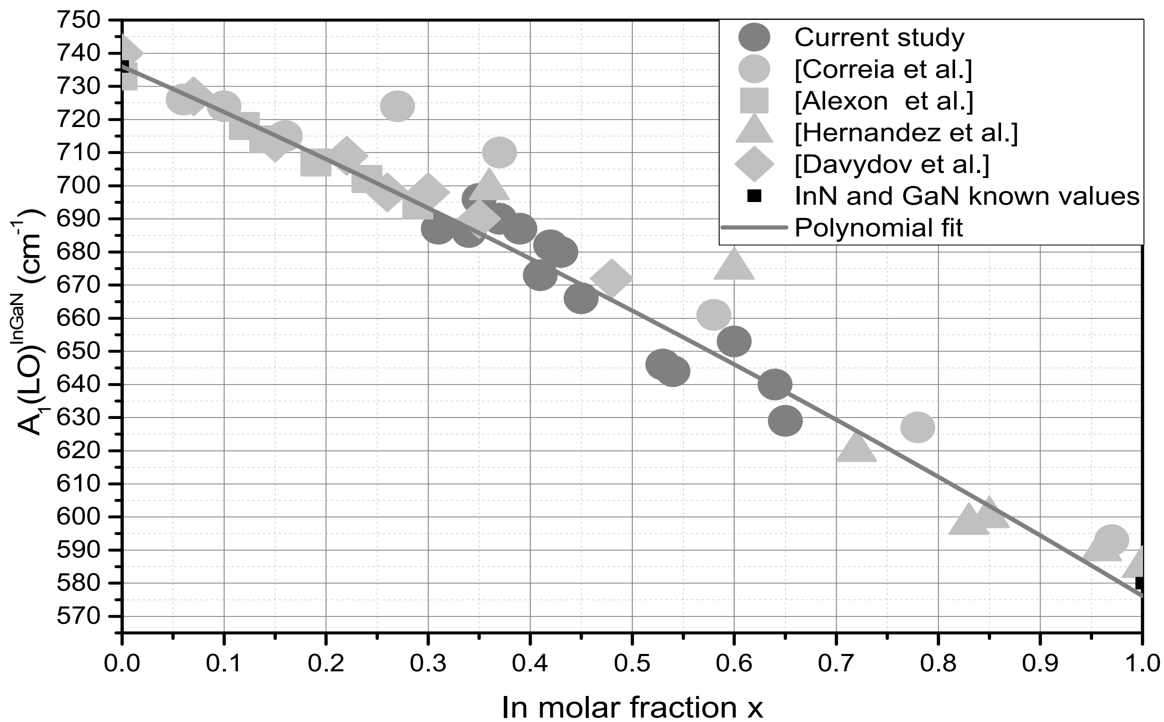

Figure 3.13: Raman shift as a function of the In concentration, for the entire InGaN composition range based on the data measured in the middle composition range (current study), Davydov et al.[80], Hernandez et al. [82], Correia et al.[81], Alexson et al.[83] , and known values for GaN (736 cm^{-1})[89] and InN (580 cm^{-1})[90]. The Polynomial fit based on Eq. (1) (the results of this study and known values for GaN and InN) is plotted as a solid line.

3.5 Droplet effects on Indium incorporation

There are several barriers in the way of increasing In amount in $In_xGa_{1-x}N$ composition. The low dissociation temperature and high equilibrium vapor pressure of nitrogen is the main issue.

Different binding energies of In-N and Ga-N are reflected in the different decomposition temperatures of InN (630°C) and GaN (850°C) [16]. Besides that, InGaN growth is hindered by the lattice mismatch between In-N and Ga-N. The lattice mismatch leads to a miscibility[91] gap which can cause fluctuations of the In content in the epilayer[92,93]. A strong solid phase immiscibility in the InGaN alloy system has been predicted.[92] Also, the effects of strain in the InGaN bimodal and spinodal curves has been calculated and shown that the miscibility problems remain significant for the case of InN mole fraction higher than 0.4.[94] InGaN phase separation has been demonstrated also experimentally, grown by both MBE[95] and Metal Organic Chemical Vapor Deposition (MOCVD) methods.[96]

As mentioned before, the growth in low temperatures, can be considered as a solution to achieve InGaN layers with high In amounts. However, in low-temperature regime, the issue of formation of metal droplets on the surface, must be taken into account. Since the In-N dissociation temperature is lower than the onset temperature for the evaporation of In[26], either we perform the growth in metal-rich condition or in a temperature higher than InN dissociation temperature (but less than In desorption temperature), metal droplets may form on the surface.

In this study we investigate the effect of surface coverage by metal droplets (SCMD) on Indium incorporation in the crystal (Figure 3.14). The In% in the composition is determined by XRD.

The reduction of In incorporation due to creation of metal droplets on the surface also has been observed by others[17,85] although they interpreted this behavior differently. They considered the metal droplets consist of only In droplets as in high (typical) growth temperatures (650 °C), the InN decomposition will occur. Hence, the excess of In atoms on the surface which are due to InN decomposition, will accumulate and make In droplets which entrap impinging In atoms. Instead, we believe the metal droplets on the surface consist of both In and Ga atoms, since our samples are grown in low temperatures (450 °C) below the InN decomposition temperature. We expect almost no InN decomposition, and so the accumulation of metal atoms on the surface is only due to excess of the Ga and In atoms arriving on the surface respect to the number of free N dangling bonds.

In N-rich growth condition where there is almost no droplet on the surface (SCMD = 0), the In incorporation is very close to the stoichiometric composition (50% considering one to one ratio between In and Ga). By increasing the metal flux, droplets start to appear as the ratio of metal flux vs nitrogen flux exceeds the equilibrium point (in our experiments is $F = 0.98 \times 10^{14}$ atoms cm^{-2} s^{-}

[1]). There is a sharp drop in In% in the composition from 53% to 31% as the SCMD increased from 0% to ~1%. The reduction of In incorporation continues linearly with a smaller slope until the SCMD reaches to 37%, corresponding to ~5% In.

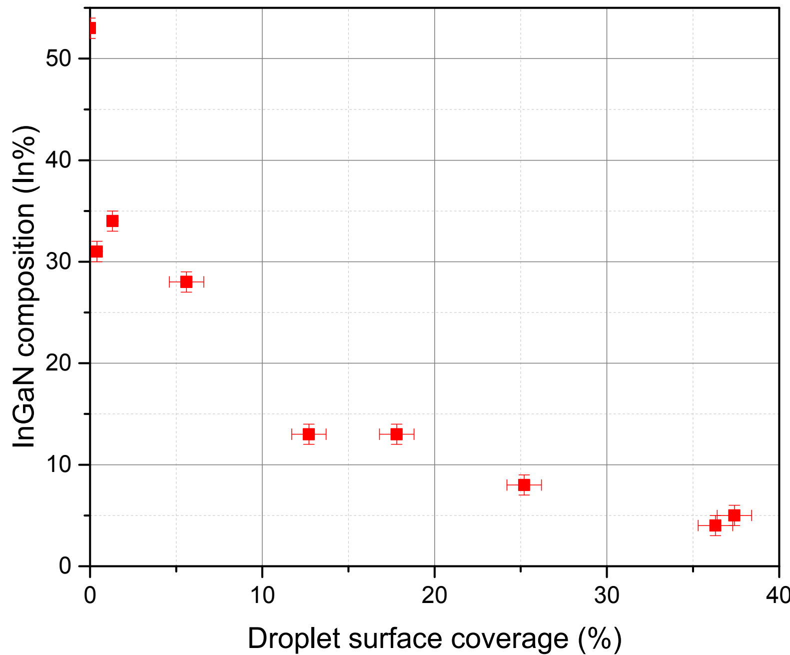

Figure 3.14: Indium incorporation as a decreasing function of surface coverage by metal droplets

In Figure 3.15 the ω–2θ scans of the InGaN samples without metal droplets (varying in the composition) are compared with a sample with metal droplets on the surface (SCMD = 18%). In case of the sample with metal droplets, there is a sharp peak around 16.5° which is known[19,97,98] to be metallic In(101). Although it is likely that a very small amount of Ga is also alloyed with Indium (considering the sample is grown in metal-rich condition with Ga/In flux equal to 1), further measurements and studies are required to prove this assumption. Broadening of the peak in the case of sample with metal droplets, is a result of variation in lattice parameter due to different composition under the droplets respect to the flat area between the droplets (as it has been explained before). This broadening is observed in the case of all InGaN samples with considerable SCMD, and is different from the broadening in the peak which is normally observed in case of InGaN sample with Indium concentration around 50% (see the peak of the sample shown in green in Figure 3.15) which is due to the immiscibility of InN and GaN.

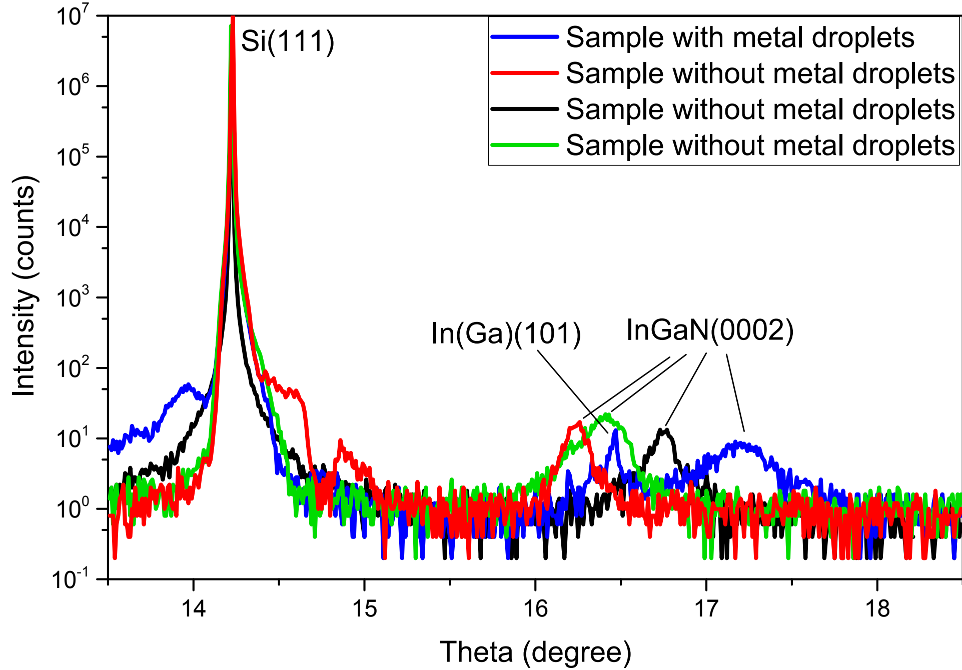

Figure 3.15: ω–2θ scans through the Si(111) peak of the substrate, showing the InGaN (0002) signal of samples without (red, black, and green) and with (blue) metal droplets on the surface. The x axis is labelled with Theta = 2θ/2

We also measure the In% locally by Raman spectroscopy. In case of sample without metal droplets (grown in N-rich regime) the composition measured in different spots of sample is constant. In case of samples which are grown in metal-rich condition, we found the existence of droplets' foot prints on the surface. The droplets' foot prints, are not metallic droplets but the crystalized InGaN grown under the metal droplets which probably are exposed on the surface due to Ostwald ripening[99] of small droplets at the end of growth, during cooling the substrate. So there was no need to use etching to remove the metal droplets in order to investigate the crystallized layer underneath. We found a clear different in the composition between the flat areas and the foot print of metal droplets. The composition under the droplets contains less Indium respect to flat area. In Figure 3.16, Raman line-scan spectra around footprint of a metal droplet shows a shift in the position of A_1 (LO) peak (which is characteristic for the composition) to higher frequencies as the laser beam moves from flat area to the foot print of the droplet (in the figure it is called island). It

suggests, different composition of flat area (In concentration ≈ 17%) respect to the composition under the droplet (In concentration ≈ 7%).

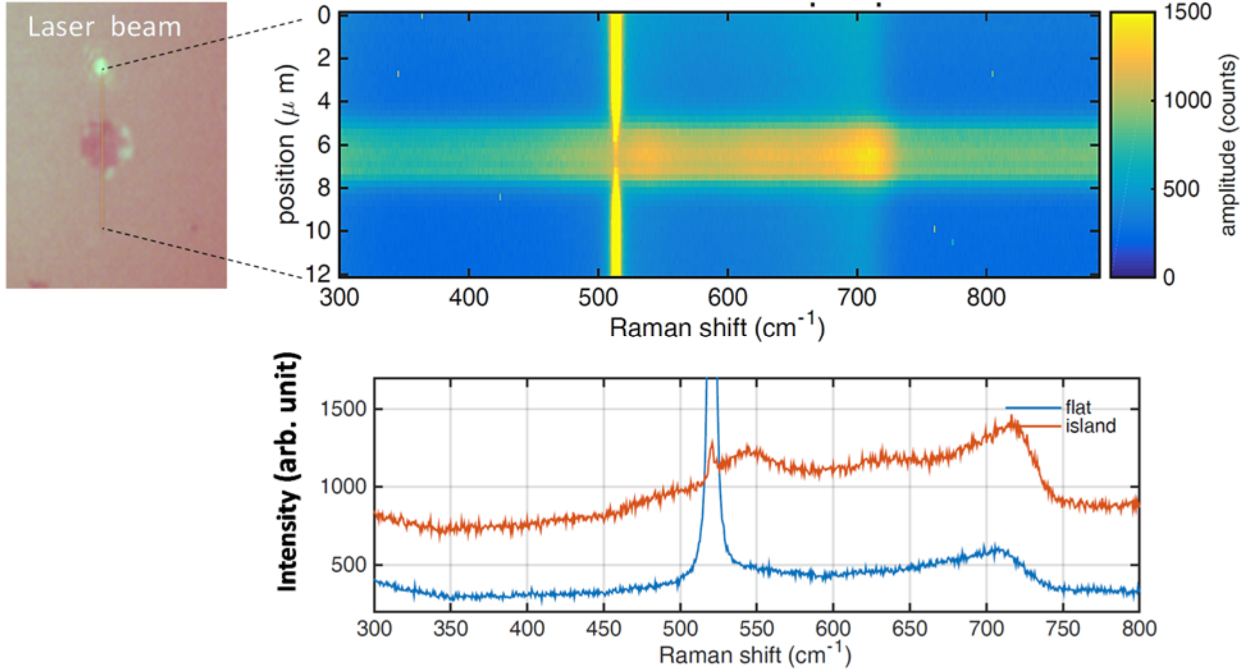

Figure 3.16: Raman line-scan spectra around footprint of a metal droplet (island) and individual spots in and out of the island.

This phenomenon is in good agreement with our previous study on droplet controlled growth dynamics. As we explained, by increasing the ratio between metals flux and N flux, from some point (equilibrium point) the excess of metal adatoms start to accumulate on the surface, generating metal droplets. The vapor-liquid-solid (VLS) growth takes place under the droplets due to nitrogen atoms directly impinging into the droplets. It can explain the reduction of In in the composition by increasing the SCMD. Similar to the case of AlGaAs[100], were under the metal droplets, VLS growth is reported to be Al-rich, in case of InGaN, VLS growth under the droplets, where there is the abundance of metal atoms respect to few number of N atoms, would be Ga-rich. Moreover, the higher diffusion length of In adatoms respect to Ga adatoms, increases the probability of In adatoms to be captured by metal droplets which further reduces the In incorporation in to the crystal.

Nevertheless, at the end of growth, there is an overall Ga-rich film, not only under the droplets but also between the droplets. It happens because during the growth, the droplets are mobile.

3.6 Growth regimes: Metal-rich, N-rich, and Intermediate

Growth kinetics play a vital role in controlling InGaN film quality by determining the preference between InGaN incorporation and indium segregation[85]. Nitride semiconductor films grown with even a slight excess of N during growth (N-stable conditions) display a rough surface morphology with a columnar structure initiated by the formation of stacking faults[27]. This can be explained considering the very different diffusivity for Ga and N adatoms on the surface. While Ga is very mobile at typical growth temperatures, the diffusion of N is slower by orders of magnitude. The presence of excess N strongly increases the Ga diffusion barrier. It has been calculated that the diffusion barrier for Ga adatoms on N-rich surfaces is as high as 1.8 eV, whereas it is only 0.4 eV when the growth is carried out on a Ga-saturated surface. Thus, N-rich growth leads to very low adatom mobility and to an undesired kinetically induced roughening of the surface[71,101,102]. It was found in RF-MBE growth of GaN and InN films under slightly metal-rich condition enhances the migration of metal atoms[102,103]. However it can cost in the phase separation of the InGaN films[102,104]. Later we explained how the growth in metal-rich condition leads to generation of metal droplets on the surface. Consequently, phase separation and reduction in both the growth rate and In incorporation occurs. On the other hand, $In_{0.5}Ga_{0.5}N$, whose bandgap lies in the near-infrared spectral region, is the most critical composition for the growth of high-quality epitaxial layers due to the strong tendency of phase separation in InGaN materials[8]. We compare the three different growth regimes: N-rich, Intermediate, and Metal-rich conditions. We show by precisely controlling the III/V ratio and growing in very low growth rate, there is a very narrow window where is possible to grow high quality, compact, and smooth InGaN single crystal on Silicon substrate without any buffer layer.

To grow device quality InGaN by MBE it is important to appreciate that there are three distinctive growth regimes: Metal-rich (sometimes called the metal droplet regime), N-rich, and Intermediate. What sets these regions apart is a combination of metal flux to active nitrogen ratio and substrate temperature. In low growth temperatures (like current study), since the growth temperature is below the In and Ga desorption temperature, we assume the excess of metal adatoms remains on

the surface. In this study we compare the morphology and composition of these three regimes. Table 3.4. Shows a summary of different growth conditions used in this study as well as surface roughness (RMS: Root Mean Square) of the samples.

In order to investigate the influence of III/V ratio on the films properties, samples I12 I13, and I14 are grown in Intermediate, N-rich, , and metal-rich conditions respectively while the ratio between Ga and In is kept equal to one.

Table 3.4: Growth parameters, RMS, and SCMD of InGaN samples

Sample	III/V ratio	Nitrogen flux (sccm)	Plasma power (W)	Growth time (mins)	Growth rate (nm/min)	RMS (nm)	SCMD (%)
I12	1	0.9	250	90	1.1	0.86	0
I13	0.8	0.9	250	90	1	4.85	0
I14	1.2	0.9	250	90	1	1.57	~1

Surface morphology of the InGaN layers is characterized using scanning electron microscopy (SEM). The surface structure at nanoscale is studied via atomic force microscopy (AFM) using an ultra-sharp tip with a curvature radius of 2 nm in tapping mode. The composition of grown layers as well as the epitaxial relationship with substrate are investigated by X-ray diffraction (XRD) using Kα1 radiation from the Cu anode ($\lambda = 0.15406$ nm).

Figure 3.17 is a comprehensive and comparative image of samples I12, I13, and I14, showing the surface morphology (SEM and AFM images), and RHEED pattern along ‹21¯1¯0› azimuth of the samples (from left to right) grown in N-rich, Intermediate, and metal-rich conditions. In case of sample I13, very rough surface structure (SEM and AFM images) and bright spotty RHEED pattern, all confirms the 3D growth mode which is known for N-rich growth condition and from the application point of view is believed to be detrimental to optical and electronic properties[27,65,105]. While in case of sample I12 and I14 analyses indicate very smooth surface and streaky RHEED pattern with some bright spots are indicative for a mixed 2D/3D growth mostly dominated by 2D growth mode.

However, in case of metal-rich growth, the excess of metal ad atoms respect to Nitrogen atoms leads to accumulation of metal atoms on the surface and generation of metal droplets that

consequently leads to reduction in growth rate and In incorporation, as well as inhomogeneity in the composition due to the VLS growth under the droplets (as explained before). While in N-rich and intermediate growth regimes the composition stands near to stoichiometric point and there is no sign of phase separation.

Our findings show that the regime, close to the onset of metal droplet formation, permits the growth of a compact layer of InGaN with adequate flatness (RMS = 0.86 nm).

Figure 3.18 displays the XRD ω–2θ scans through the Si(111) peak of the substrate for the samples I12, I13, and I14, showing the InGaN (0002) signal. While the peaks of samples I12 and I13 show the composition close to the stoichiometric composition ($In_{0.5}Ga_{0.5}N$) there is a dramatic shift of the peak toward higher angles for the sample I14 indicating the reduction of In incorporation in the crystal when the growth is carried in metal-rich condition. This is explained in our previous study and also in other works[17,35,85]. In case of sample I14 also there is an additional narrow peak (around 16.5°) which has been observed for all the samples grown in metal-rich condition and as it was mentioned before, is known[19,97,98] to be In (101).

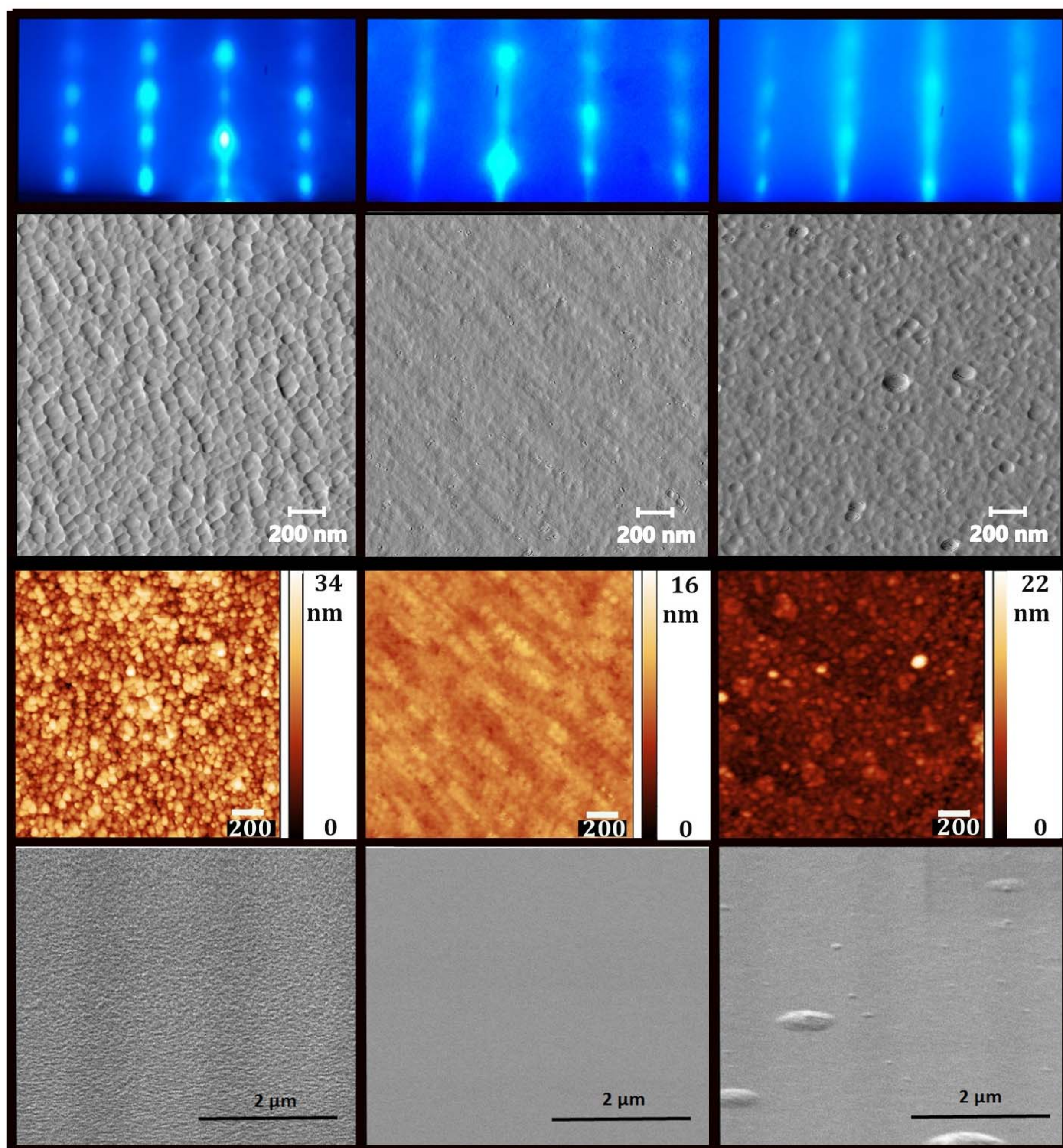

Figure 3.17: From left to right, Samples grown in N-rich (sample I13), Intermediate (sample I12), and Metal-rich (sample I14) regimes. From top to down, RHEED pattern along $\langle 2\bar{1}\bar{1}0 \rangle$ azimuth, AFM image deflection (amplitude) and topography (height) images (tapping mode), and SEM image using secondary electrons detector of each sample respectively.

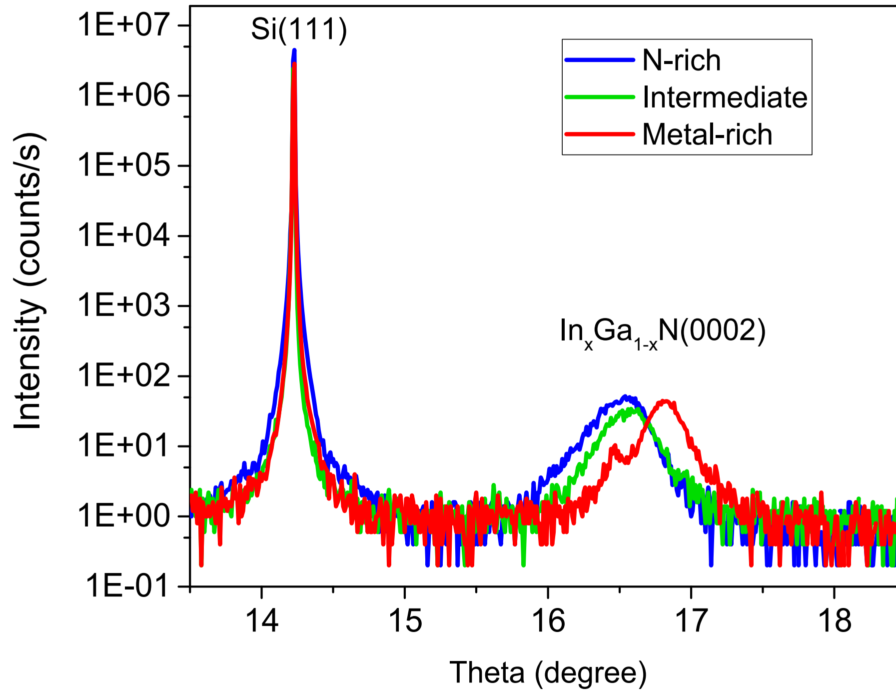

Figure 3.18: ω–2θ scans through the Si(111) peak of the substrate, showing the InGaN (0002) signal of samples (green) I12, (blue) I13, and (red) I14 (SCMD ≈ 1%). The x axis is labelled with Theta = 2θ/2

In order to proof the epitaxial relation of Si substrate with InGaN grown layers, supplementary XRD measurements is carried out. Reciprocal space map around the InGaN (0002) Bragg peak is carried out, using the Si(111) peak from the substrate as a reference. However, the existence of a InGaN(0002)||Si(111) relation does not guarantee that the material is epitaxial. (It is known, for example, that Si eventually forms (111) columns even on amorphous substrates or after the collapse of epitaxy on Si(001)[106]. For this, asymmetric reflections must be identified[32], for example the InGaN(1015) near the Si(224). Only in this case the basal plane lattice parameter, a, can be measured, and the In content and strain be unambiguously ascertained. Reciprocal space is defined such that

(3.10)

$$q_{\perp} = 2/\lambda \sin\theta \cos(\theta - \omega)$$

$$q_{\parallel} = 2/\lambda \sin\theta \sin(\theta - \omega)$$

and for the Si(111) surface, $q_{\perp}$||[111] and $q_{||}$||[112]. Hence, Si(224) is found in an asymmetric "grazing incidence" (i.e. $\omega < \theta$) geometry. Figure 3.19(a) and (b) the reciprocal space map, shows InGaN(0002)||Si(111) Bragg peak and also InGaN(1015) close to Si(224), demonstrating the epitaxial relationship between the InGaN and the Si. It worth to mention that this proof applies only in case of samples which are grown on nitridated surface, and we could not observe this relation in case of the sample which is grown without nitridation step.

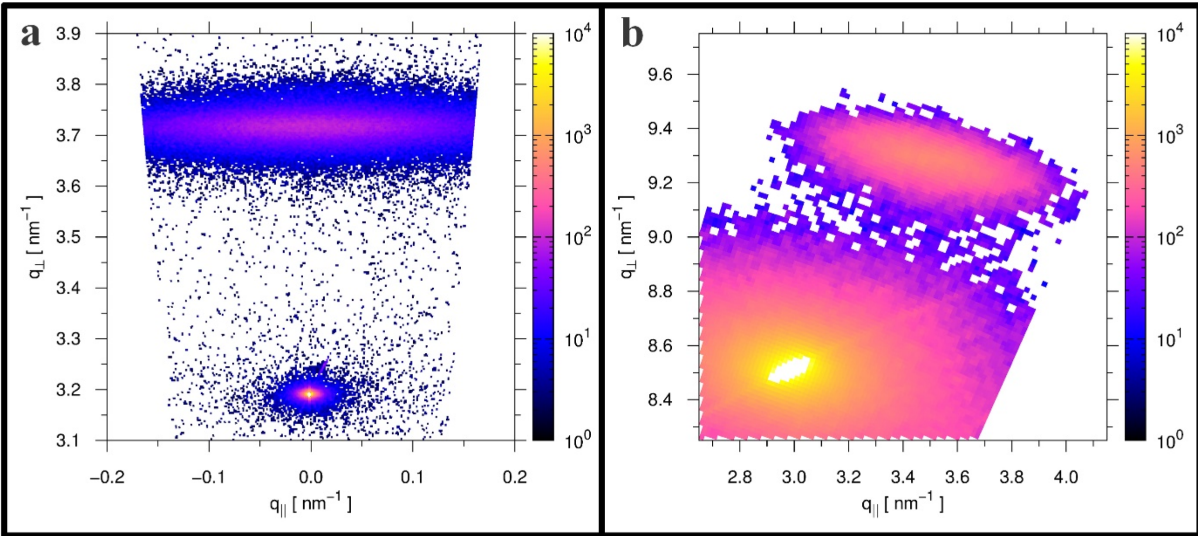

Figure 3.19: XRD Reciprocal space map (a) along the Si(111) and (b) close to Si(224), demonstrating the heteroepitaxial relationship between InGaN thin film grown on Si.

Chapter 4

4. Growth and characterization of self-assembled GaN and AlN NWs on TiN_x-sputtered sapphire

To solve the problem with lack of lattice-matched substrates, growing 3D structures like NWs seems an attractive solution as they can release the epitaxial strain through a lateral plastic relaxation[36]. They have attracted much interest in recent times because of their great potential for the fabrication of electronic and optoelectronic devices.[107–109] The growth of semiconductor NWs is a rapidly expanding field driven in part by the unique functionality of NWs and their high crystalline quality despite high degrees of epitaxial or thermal mismatch strain, particularly for group III-N semiconductors. The majority of NWs are grown with catalyst nanoparticles, usually a metal such as Au or Ni, which enhances growth at the nanowire tip through supersaturation of reactant species within the catalyst droplet. On the other hand, growing self-assembled NWs is becoming more important considering their much higher structural and optical quality than those grown with the use of external catalyst. Different techniques such as MOCVD[110],PA-MBE[111,112] and chemical beam epitaxy[113] have been used to grow different semiconductor NWs with extremely high crystalline quality.[114] In this regard, MBE has the advantage to permit the growth of high quality, stacking fault-free, GaN NWs without using any external catalysts in comparison to MOCVD which generally requires the use of metallic catalyst, with the possible risk of metal contamination. In contrast to conventional methods for NWs growth which are mostly based either on catalyst seeds [72,115] or on pre-patterned masks [116] GaN NWs under suitable conditions in MBE (N-rich and elevated temperatures), spontaneously grow on various substrates without the need for any foreign material [117–120]. The potential of GaN NWs was recognized in the late 1990s, when several groups reported their self-assembled growth and their supreme crystal quality[119,121], although, semiconductor wires perpendicular to a substrate and having micrometric diameters were first fabricated more than 50 years ago.[72] Now, using modern epitaxy techniques, homogeneous wires with much smaller diameters are grown.

As previously mentioned in the first chapter, growing GaN NWs instead of thin films, seems a promising solution to overcome the issue with high TDs density which are usually formed due to growing on lattices mismatched substrates. However, it should not be forgotten that solving the

problem of lattice-mismatched substrates by growing NWs, does not necessarily mean the freedom in substrate choice. There are still many parameters left to be considered in choosing the substrate, depend on growth condition, nanowires composition, and the application. So far, finding a proper substrate for III-N NWs growth which fulfills all the expectations has been very challenging.

In this chapter, I discuss my research work in department of epitaxy in PDI institute, on a very promising approach to grow high quality GaN and AlN NWs. I introduce here, TiN_x-sputtered sapphire as an excellent surface to grow GaN and AlN NWs.

4.1.1 Sputtering TiN_x on sapphire by reactive magnetron sputtering

Titanium nitride sputtering have attracted considerable attention not only from fundamental scientific interest but also from practical point of view in many industries. It is used as anti-reflective coating and as diffusion barrier[122] in the microelectronics industry.

In current work, I sputter TiN_x film on sapphire, to be used later as a surface to grow GaN and AlN NWs. In order to sputter TiN, I have used a magnetron sputtering system. Inside the sputtering chamber, a high purity 3-inch Ti plate (target) is placed opposite to the substrate (2-inch sapphire wafer). The background pressure in the chamber is ~10^{-10} Torr, using a turbo molecular pump and a cryo pump. For the TiN sputtering, the chamber is filled with a mixture of argon/nitrogen gasses which are separately controlled by mass flow controllers. Sputtering of TiN is carried out by injecting Ar and N fluxes and applying a DC power to generate the plasma. This plasma consists of positively charged argon/nitrogen ions and free electrons. The positively charged ions are accelerated towards the negatively charged Ti plate (cathode). They collide with the surface of the Ti plate with a high kinetic energy of up to several hundred electron volts (eV). This causes the argon/nitrogen ions to dislodge atoms from the surface of the Ti plate. A potential applied between the chamber and the substrate, accelerates the Ti particles from the target toward the substrate. The optimum condition for the TiN sputtering (depend on the application), can be tuned by changing sputtering parameters such as: Plasma power, Ar and N fluxes, substrate temperature, and bias voltage. To change stoichiometry of the TiN_x composition, the ratio of Ar/N fluxes can be tuned. The higher Ar + N flux means the higher number of Ti particles will be ejected from the target which will increase the sputtering rate. On the other hand, the higher Ar/N ratio, will increase the Ti/N ions ratio, so the final TiN_x composition would be Ti-rich. By changing the Ti/N ions ratio,

also morphology of the TiN_x sputtered films changes which can later affect the NWs nucleation process. Based on our experiments, $TiN_{0.85}$-sputtered film is considered as the optimum substrate to grow GaN NWs while stoichiometric TiN-sputtered film is required for the growth of AlN NWs. In Figure 4.1 and Figure 4.2 the color and microstructure of both the stoichiometric TiN-sputtered sapphire and the $TiN_{0.85}$-sputtered sapphire can be seen. The golden color can be used as the very primary inspection of stoichiometric TiN film[122]. The side view SEM images indicate smoother structure for $TiN_{0.85}$ film. 4-probe measurement of $TiN_{0.85}$-sputtered film revealed a low resistivity of 4×10^{-4} Ωcm.

Further characteristics of TiN_x-sputtered films as well as growth and characteristics of NWs are discussed in following.

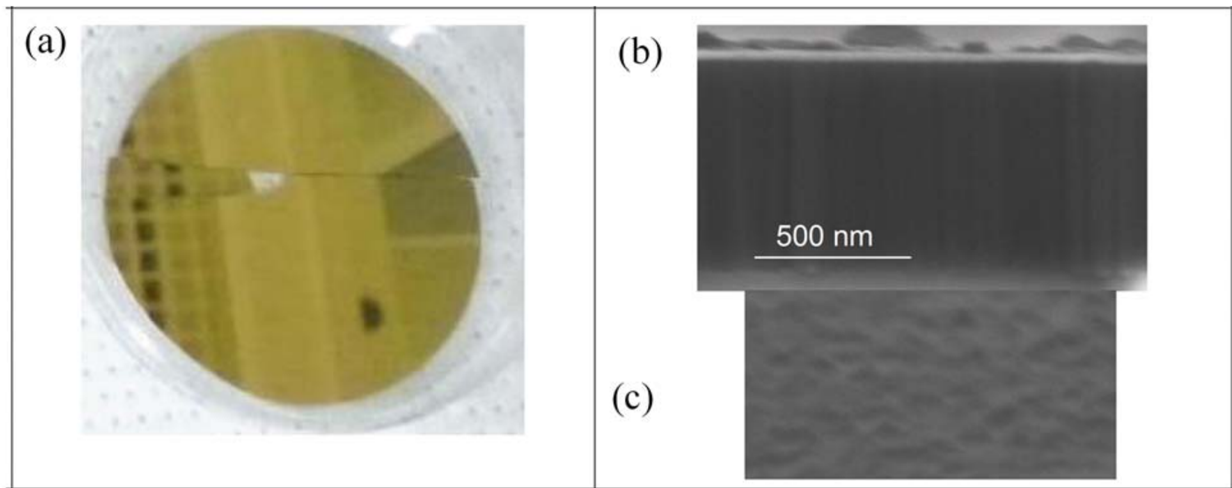

Figure 4.1: (a) A stoichiometric TiN-sputtered sapphire (~ 0.8 µm), and (b) and (c) side view and top view SEM images of that.

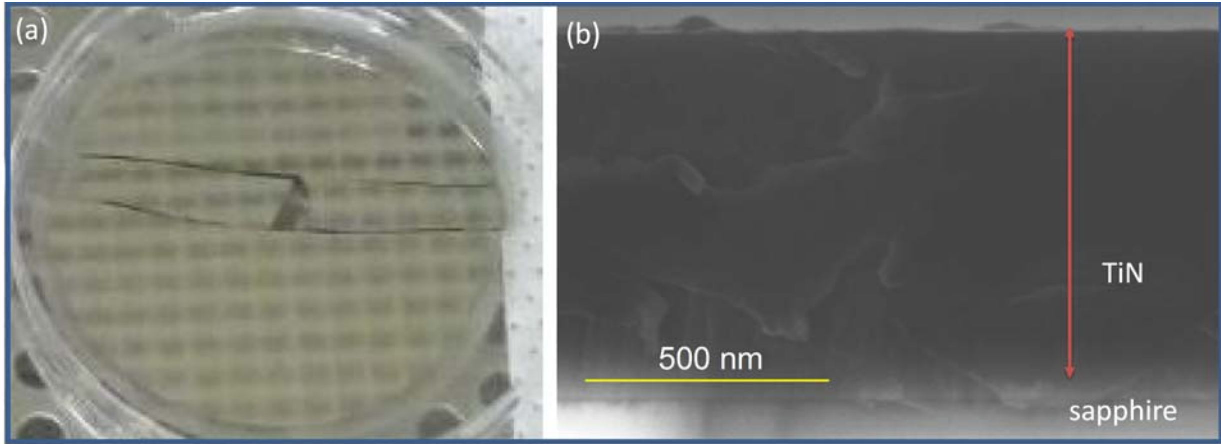

Figure 4.2: (a) A $TiN_{0.85}$-sputtered sapphire, and (b) side view SEM image of that.

4.1 Self-assembled GaN NWs growth on TiN_x-sputtered sapphire

As mentioned before, GaN NWs under suitable conditions in MBE (N-rich and elevated temperatures), spontaneously grow on various substrates without the need for any foreign material [117–120]. In the most common case, GaN NWs successfully are grown on Si. However due to high densities of NWs, longer deposition times leads to a massive coalescence of closely spaced NWs.[123,124] Brubaker et al. suggested introducing an AlN buffer layer on Si to reduce the density of NWs[125]. However, on AlN, in addition to the NWs, a rather thick parasitic GaN layer forms. Besides that, such an AlN buffer layer (which is tens of nm thick)[126] as an insulator is detrimental for the III-N/Si heterojunction electrical functionality. Recently Ti foil and Ti-sputtered sapphire have been successfully used as substrates to grow self-assembled GaN NWs with low NW densities[118,127,128]. In this approach, first ∼1 µm Ti film is sputtered on sapphire wafer. Then the surface of Ti becomes nitridated during the growth (or before the growth, in case of preforming pre-nitridation process) and a very thin TiN layer (∼50 nm) is formed on top of Ti film. Using PA-MBE, GaN NWs are grown on this thin TiN surface. These Ti substrates are very promising with respect to electrical as well as thermal conductivity and optical reflectivity which is beneficial for applications like LEDs based on NW ensembles[129–131]. However, in elevated temperatures, inter-diffusion of Al and O at the Ti/Al2O3 interface is reported[132] which results in formation of $Al_xTi_yO_{1-x-y}$ and Ti_xO_{1-x} compounds. Furthermore, O incorporation into NWs degrades their luminescence by heavy n-type doping. Although TiN is very effective diffusion barrier[122] due to

its strong bonds, it seems, in the mentioned approach, the thickness of TiN layer formed on top of Ti film was not enough to suppress the O diffusion. So, nor the thin TiN layer, nither the ~1 μm thick Ti film, could not prevent the O diffusion.

In order to overcome this previously reported problems, in this thesis, I sputter TiN instead of Ti, to benefit from strong Ti-N bond. In case of Ti-sputtered film, because of self-passivation phenomenon, the thickness of TiN layer (which is formed due to nitridation of Ti in the MBE chamber) is limited to some tens of nm. However, by directly sputtering of TiN, depend on the requirements, several microns thick TiN films are easily achievable.

Such a thick TiN, would be enough to block the diffusion of impurities from substrate to GaN NWs as will be discussed in following.

In this study, 0.8 μm thick TiN_x film is sputtered onto a 2-inch sapphire [α-Al_2O_3(0001)] wafer in a dc magnetron sputtering system with 3×10^{-10} Torr base pressure. The deposition is performed for 40 min in a sputtering pressure of 10^{-3} Torr by injecting 13.5 ± 0.2 sccm Ar and 1.5 ± 0.18 sccm N fluxes and applying a DC power of 500 W to generate the plasma. During the sputtering an additional 100 V bias voltage is applied to the substrate to improve the physical properties of the film[133]. After sputtering TiN_x film on the substrate, the sample is transferred in ultra-high vacuum into a MBE chamber (with a background pressure of 8×10^{-11} Torr) where it is heated up to 810 °C and exposed for 25 min to active nitrogen which is generated by a radio-frequency plasma source operating at 500 W and 2.5 sccm N_2 flux. The substrate temperature is measured by a pyrometer facing the center of the substrate (taking in to account the emissivity of TiN and absorption of view port). To calibrate the pyrometer the 7×7 to 1×1 Si transition temperature (860 °C)[64] is used. The nucleation and growth of GaN NWs require a high substrate temperature and a N/Ga adatom density ratio (local V/III ratio) above unity.[28,134] The GaN NWs nucleation procedure is started by opening Ga shutter at 810 °C and simultaneously reducing the substrate temperature (with a cooling rate of 40 °C/min) to 730 °C which is then kept constant for the whole duration of the growth. The growth is performed under pressure of 4×10^{-5} Torr, and active nitrogen to Ga ratio of ~3 (Ga flux of 6.6×10^{14} atoms/cm^2.s and N flux of 2.1×10^{15} atoms/cm^2.s). The typical wurtzite RHEED pattern of GaN is observed after one minute (at 730 °C).

To investigate GaN NWs ensembles grown on TiN-sputtered sapphire, two samples, G1 and G2, are prepared using the same growth conditions with different growth durations of 90 and 150 min respectively.

In Figure 4.3 bird-view SEM image of sample G1 is shown. As can be seen, the NWs are grown homogenously and vertically. This homogeneity of NWs observed all over the sample from center to the edge.

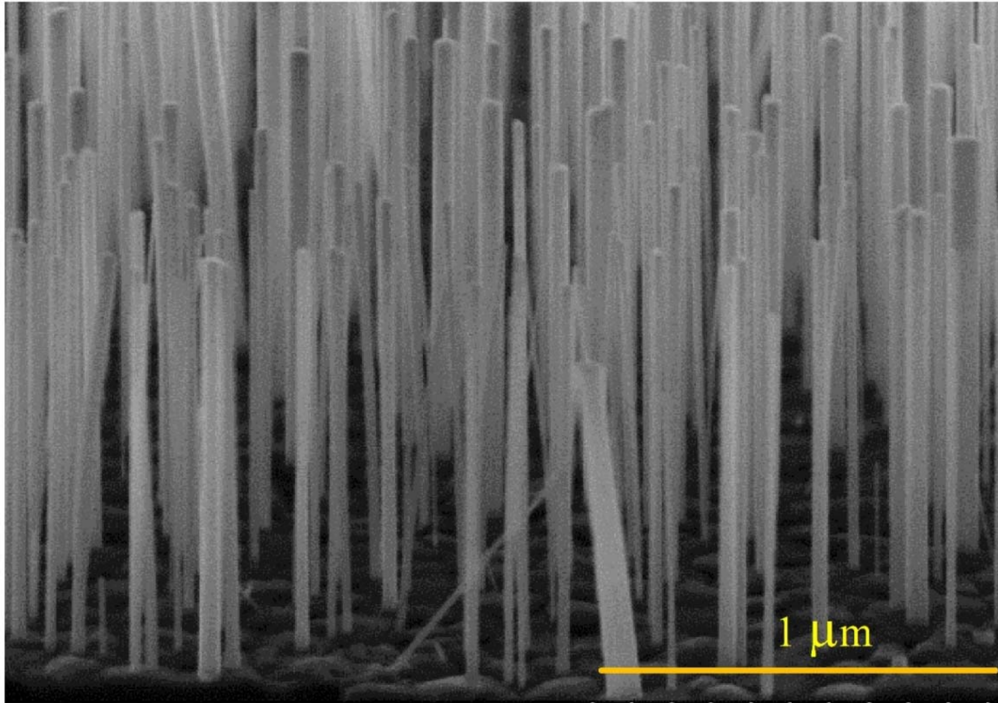

Figure 4.3: Bird view SEM image of sample G1

To determine and compare the length, diameter, and the density of NWs, cross-view and top-view SEM images of the two samples are depicted in Figure 4.4. Using the top view SEM images, the density of NWs is measured. No relation is found between the density of NWs and the growth time. NWs average length and diameter are measured by using the cross-section SEM images. The size and density of NWs are compared in Table 4.1. In both samples the coalescence degree is almost zero (although it is possible that some thicker NWs, are formed by combination of two or more very closely located NWs).

Table 4.1: Comparison between sample G1 and G2

Sample	Growth time (min)	Average length (µm)	Average diameter (nm)	Density of NWs (cm^{-2})	Filling factor (%)
G1	90	1.15	30	2×10^9	4
G2	150	1.85	50	2×10^9	5

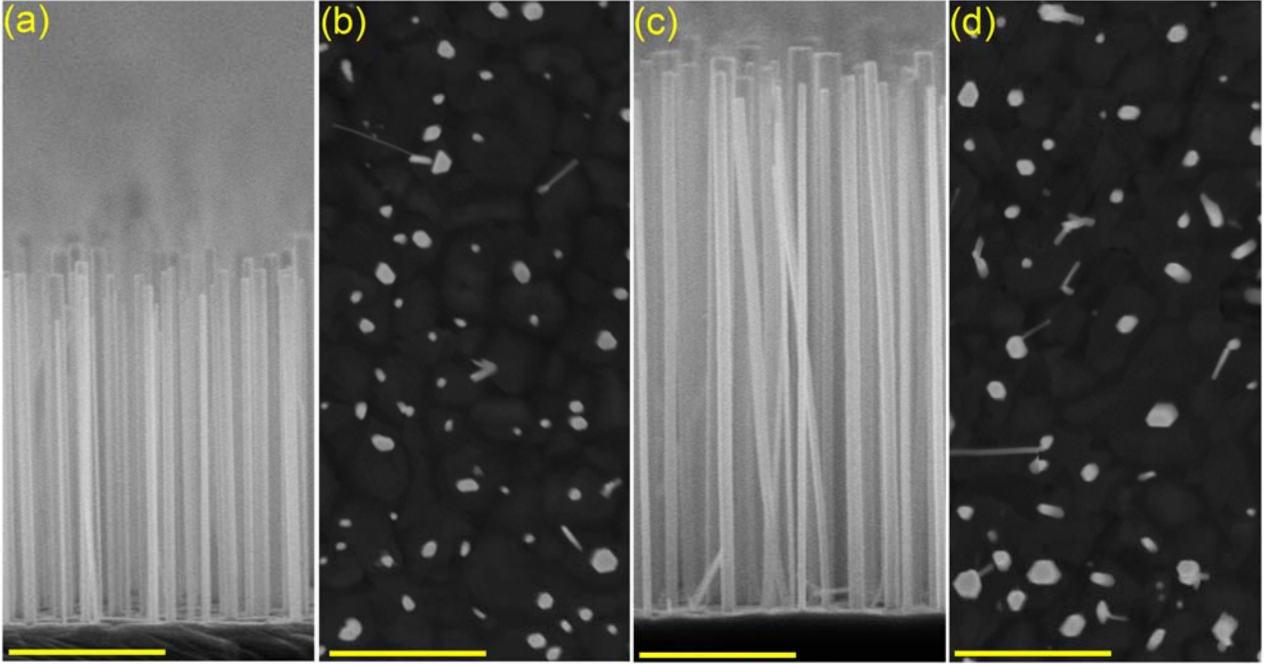

Figure 4.4: Cross view and top view SEM images of sample G1 (a and b), and sample G2 (c and d). The yellow line length for all the images is 500 nm.

The characteristics of TiN film and GaN NWs are investigated using RHEED, variable-angle spectroscopic ellipsometry, and Raman spectroscopy.

Figure 4.5 (a) And (b) show the RHEED pattern of sample G1 after sputtering and after the NWs growth respectively. The streaky-spotty RHEED pattern in Figure 4.5(a), demonstrates that the TiN_x-sputtered film has cubic single crystalline structure with [111] out-of-plane orientation such that TiN⟨111⟩‖Al2O3⟨0001⟩. Figure 4.5(b) Shows wurtzite RHEED pattern of GaN NWs. The diffracted electrons from NWs side-facets, form horizontal lines on the RHEED screen, which indicate low-density, narrow, vertical NWs with well-defined facets. In order to investigate the Ti/N ratio, variable-angle spectroscopic ellipsometry is employed. The behavior of ⟨ε1⟩ (real

part) and ⟨ε2⟩ (imaginary part) of the pseudodielectric function at low photon energies is characteristic for a metal. Moreover, comparing the value of photon energy when ⟨ε1⟩ crossing zero (which is shifted to higher photon energy), with literature[135,136], confirms the sputtered TiN_x is Ti-rich. Considering the results of ellipsometry measurement (the values of photon energy when ⟨ε1⟩ cross zero) and Raman spectroscopy (the values of low frequency acoustic phonons, TA and LA (more importantly TA)), before and after GaN NWs growth, we see the TiN_x composition evolution from Ti-rich toward the stoichiometry is occurred. This is due to nitridation of TiN_x film before starting the growth (during nitridation process) and also during GaN NWs growth. Comparing to Ref.[Spengler1978][137], an approximately quantitative measurement of Ti/N of sputtered film can be determined considering the position of low frequency acoustic phonon peak (TA), after sputtering (240 cm^{-1}) and after GaN NWs growth (245 cm^{-1}) corresponding to $TiN_{0.85}$ and $TiN_{0.95}$ respectively. As for GaN peaks in Raman spectra, the E_2 (high) is known to be the only usable phonon mode for accurate determination of the GaN strain components[138]. GaN E_2 (TO) mode at 566.2 cm^{-1} in Figure 4.5(e) is in good agreement with strain-free GaN reported in the litrature[138] which confirmers the NWs are relaxed.

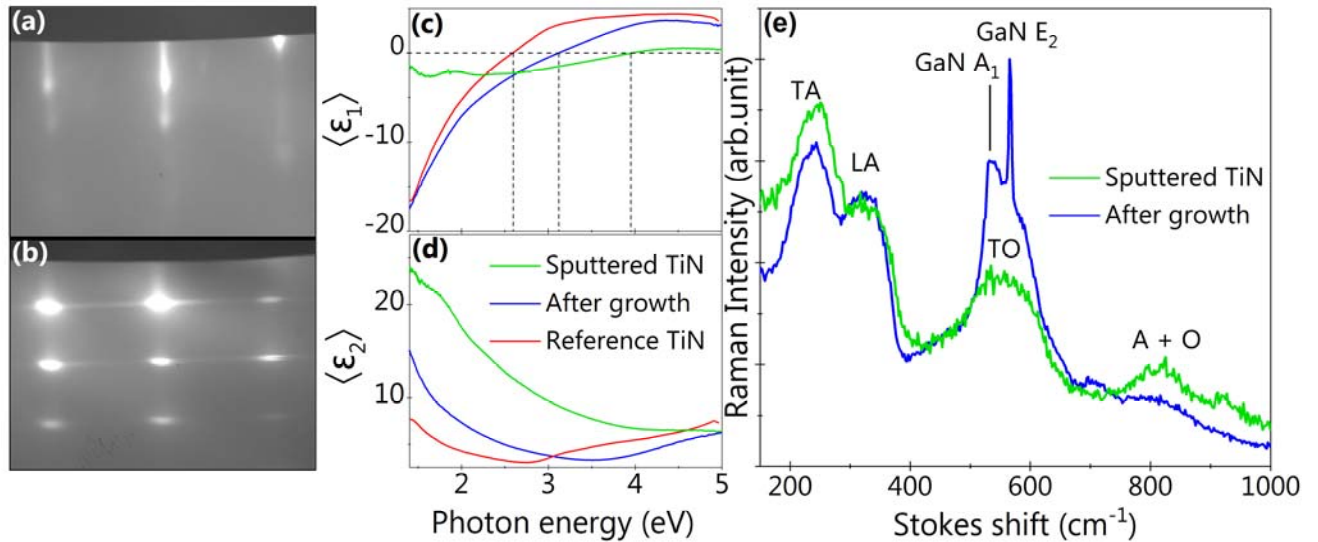

Figure 4.5: Sample G1, (a) RHEED pattern of TiN_x film prior to exposure to Ga. (b) RHEED pattern after the growth of GaN NWs. (c) Real and (d) imaginary part of the pseudodielectric function obtained by spectroscopic ellipsometry after sputtering (green), after NWs growth (blue), and stoichiometric TiN studied by Ref.[139] (red). (e) Raman spectra after sputtering TiN_x and after GaN NWs growth.

ω–2θ scan XRD measurements of sample G1 around the GaN(0002) Bragg peak is carried out, using Al_2O_3(0006) peak from the substrate as the reference. Figure 4.6 demonstrates wurtzite GaN(0002) grown in C-direction perpendicular to the substrate, and cubic TiN_x(111) planes parallel to Al_2O_3(0001).

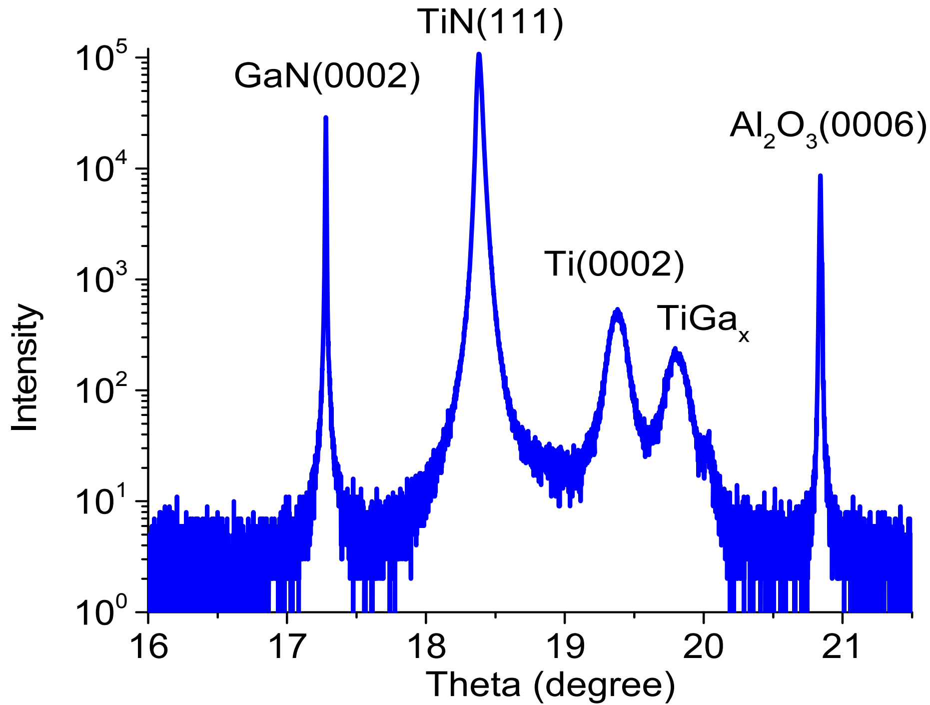

Figure 4.6: ω–2θ scan through the Al_20_3(0006) peak of the substrate, showing The x axis is labelled with Theta = 2θ/2.

The GaN(0002) shows an extremely sharp diffraction peak with FWHM of 25 arcsecond. Also TiN_x(111) and Al_2O_3(0006) peaks show FWHM of 118 and 32 arcsecond respectively. A very important point is that no signal from TiO or Ti_2O is detected, which indicates TiN_x successfully damps the oxygen diffusion from Al_2O_3 to the GaN NWs. This is one of the main improvements reached using TiN_x-sputtered substrate in comparison to previously reported NWs grown on Ti-sputtered substrates[127,128,132].

The Ti(0002) peak found in the composition is due to the excess of Ti atoms respect to N atoms, which probably are diffused toward the surface (to minimize the strain) during heating the sample.

There is also a weak $TiGa_x$ peak present in the XRD spectra, which is due to intermixing of Ga atoms with the excess of Ti atoms present on the TiN_x surface. However, the amount of this $TiGa_x$ alloy is negligible compared to the amount reported in case of GaN NWs growth on Ti-sputtered film. With tuning the setup of QMS, it is possible to measure desorption flux of elements on top of the sample's surface with high accuracy. In this way we can do quantitatively real-time monitoring of GaN nucleation and desorption. Using QMS (Figure 4.7) I measured the temporal evolution of Ga desorption flux (Φ^{des}) at the early stage of the NWs growth to check the amount of consumed Ga before the nucleation of GaN (which is monitored by RHEED). Comparing the Ga Φ^{des} of sample G1 (NWs grown on TiN_x-sputtered sapphire) and a sample grown on Ti-sputtered sapphire[132], it is quite clear that the amount of Ga-Ti intermixing in sample G1 is negligible. In Figure 4.7, the change in the Ga Φ^{des} of the two above mentioned samples, exactly after opening the Ga shatter at the beginning of growth procedure and during growth is shown. In case of sample G1 which is depicted in blue line, by opening the Ga shutter, the Ga Φ^{des} reaches to its maximum immediately. As mentioned before the Ga shutter is opened at 810 °C which makes the incubation time infinity. When I reduce the temperature to 730 °C, the nucleation of GaN NWs occurs (after one minute) and you can see the reduction in Ga Φ^{des} which is due to Ga incorporation in to the crystal. From this point, GaN nucleuses (and later NWs) capture the Ga adatoms and so for the rest of the growth, the Ga Φ^{des} is almost constant. This behavior is very similar to our previously observed droplet effect in chapter 3, where metal droplets on InGaN surface capture the In and Ga adatoms like a sink and prevent them to incorporate in the flat area between the droplets. Here instead, there is no metal droplet, but GaN initial nucleuses (and later GaN NWs) are capturing Ga adatoms.

However, the story is very different for the NWs growing on the Ti-sputtered sapphire (red line in Figure 4.7). By opening the Ga shutter in this sample, the Ga Φ^{des} does not reach to its maximum immediately, but instead, it gradually increases from 0 to ~0.22 ML/s. This gradual rise instead of immediate rise (which observed for TiN_x-sputtered sample) indicates a considerable Ga incorporation into the sample. However, as it is reported in Ref.[132], the GaN diffraction spots in the RHEED pattern do not appear until a growth time of 92 min. From this, we can conclude during this time, Ga was not incorporating to GaN, but to the Ti film. A strong Ga consumption of 560 MLs has been measured before GaN nucleation. It is found detrimental for the NWs growth, since

this Ga-Ti alloys later form hillocks on the surface[132] (Figure 4.8). Such hillocks is not observed in case of GaN NWs grown on TiN_x-sputtered sapphire.

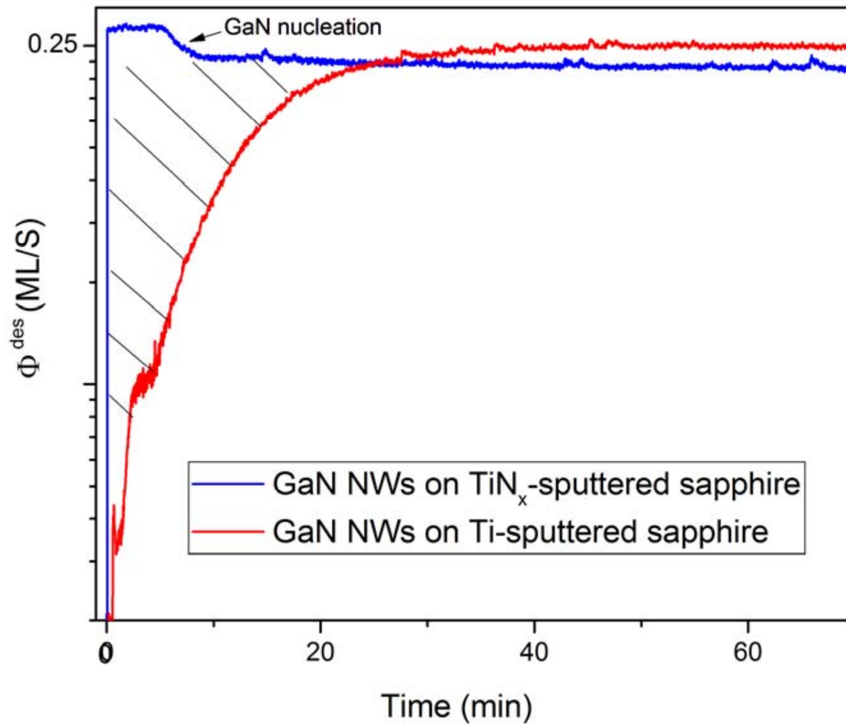

Figure 4.7: Monitoring the GaN incorporation by QMS during the nucleation and growth of GaN NWs of sample G1 (GaN NWs grown on TiN_x-sputtered sapphire) and comparing it to reported results in Ref.[132] (GaN NWs grown on Ti-sputtered sapphire).

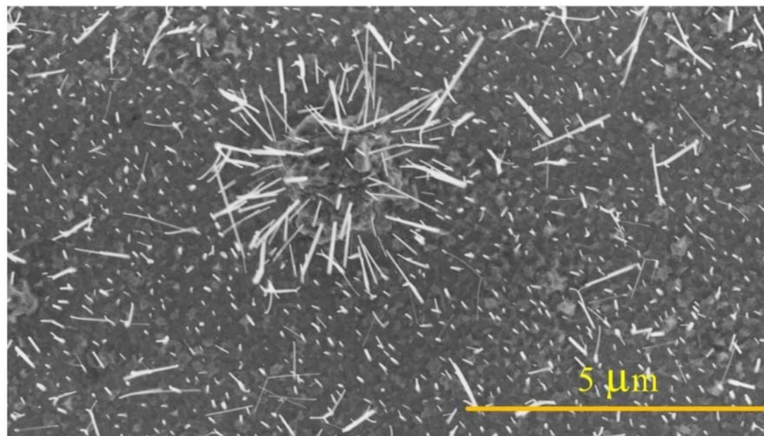

Figure 4.8: Formation of hillocks during the growth of GaN NWs on Ti-sputtered sapphire (SEM image by Gabriele Calabrese, Paul Drude Institute).

Furthermore, XRD rocking curves around GaN(0002) and GaN($1\bar{1}00$) taken from sample G1, reveals GaN NWs average tilt and twist of 0.64 and 0.54 degree respectively (Figure 4.9) which is relatively low.

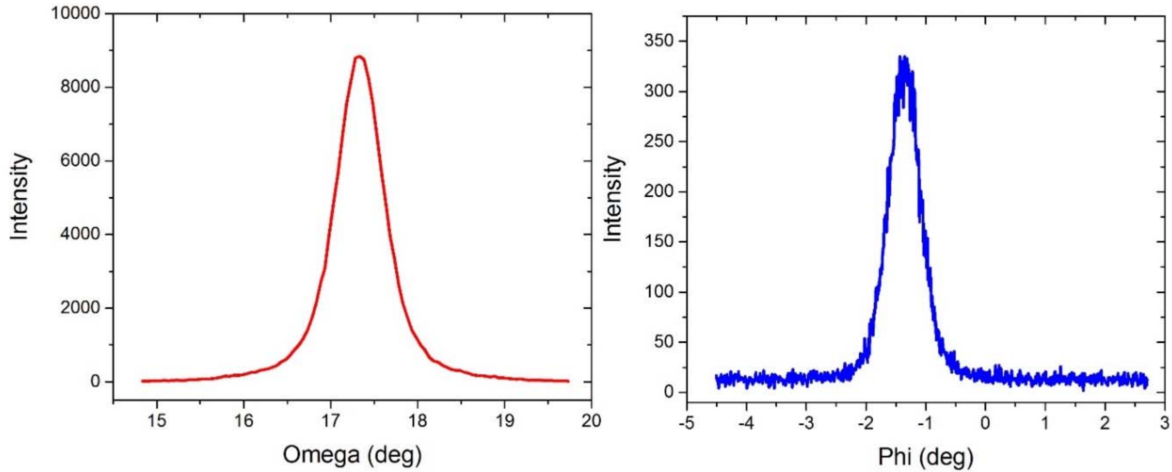

Figure 4.9: XRD Omega and Phi scan of sample G1, demonstrating the tilt and twist of NWs.

In order to study the luminescence properties of the NWs, low-temperature μ-PL measurements of both samples (G1 and G2) are performed. Figure 4.10 displays the normalized μ-PL spectra of the two samples obtained at 10 K, using a 325 nm wavelength laser perpendicular to the sample and the averaged optical power about 2 mW. The spectra are dominated by the recombination of A excitons bound to neutral donors (D^0, X_A) at 3.4725 eV. In the energy range of 3.40 to 3.43 eV, a weak broad peak (a set of peaks) is observed, which is attributed to the radiative recombination of excitons bound to I_1 stacking faults in GaN.[140] This type of stacking fault was shown to be induced by the coalescence of GaN NWs.[141] Although, from SEM images (Figure 4.3and Figure 4.4) no coalesced NWs can be detected, it is still possible at some minor cases where NWs are nucleated very close to each other, they coalesce by lateral growth and make a thicker NWs. This is in agreement with slightly higher observed intensity of broad peaks at 3.40 to 3.43 eV in case of sample G2 respect to sample G1. Since the growth duration of sample G2 is longer, the lateral growth of NWs and consequently the coalescence possibility is higher.

However, the stacking faults may also form during the nucleation phase of GaN on TiN_x. To clarify that, detailed microscopic investigations of the interface between the TiN_x film and the GaN NWs

will be required. It worth noting that no PL signal is detected in a spectral range between 2 to 3.40 eV.

In the inset of Figure 4.10, Time-resolved PL transients of the (D^0, X_A) are shown. The measurements are performed at a periodic time of 13 ns between the 200 fs pulses, which translates to an energy density of 66 mJ/cm^2 per pulse and a carrier density of 1.1×10^{14} cm^{-2}. Using the optical lens reduce the spot size on the sample to 40 μm which results in an energy density of about 2.1 mJ/cm^2 per pulse and a carrier density of 3.4×10^{14} cm^{-2}.

Considering the 40 μm laser spot size on the sample and the measured average density of NWs of about 2×10^9 cm^{-2}, it can be estimated that about 800 NWs are located under the laser focus.

TRPL provides useful information about the quality of the material since the existence of non-radiative sites like defects or impurities in the crystal, will reduce the TRPL life time. For commercial freestanding GaN homoepitaxial layers grown by vapor phase epitaxy on GaN bulk single crystals, the TRPL lifetime at low temperatures (< 10K), for donor bound excitons (I_2), reaches ~1 ns, whereas it is normally around 35–100 ps in heteroepitaxial layers and 200–300 ps for epitaxial lateral overgrowth (ELO) GaN (limited by deep traps).[142] It was suggested that the bound exciton decay of thin GaN NWs is governed by non-radiative surface recombination (even at low temperatures).[143] However this short lifetime which evidences the presence of a strong non-radiative channel in GaN NWs, is attributed to point defects rather than structural defects or surface recombination.[37]

In spite of their high structural perfection, the excitonic lifetime of state-of-the-art GaN NW ensembles grown on Si substrates by MBE, does not exceed ~250 ps at 10 K. These non-radiative point defects may either originate from deep impurities such as Ca stemming from the ex-situ substrate preparation[38] or be formed by native defects. It makes the use of a higher growth temperature desirable. At these high temperatures, however, Si substrates may start to decompose.[39]

As it is shown in Figure 4.10 inset, the GaN NWs grown on TiN-sputtered film which are only 30-50 nm thick , exhibit 400 ps radiative lifetime of the (D^0, X). This is much longer than the ~250 ps (the state-of-the-art GaN NWs grown on Si) which was the longest exitonic lifetime observed in case of GaN NWs. Comparing the two samples, no considerable size-dependent influence can be detected from the TRPL measurements.

The decay process, is very sensitive to additional non-radiative recombination channels, as well as to excitation transfer processes at higher doping levels.[60] Hence, this long radiative lifetime suggests that the density of dislocations in the GaN NWs grown on TiN_x-sapphire is quite low. This is due to the effective plastic relaxation of NWs. Moreover, it confirms very pure GaN NWs which means TiN_x buffer layer successfully prevented the O and other impurities to diffuse from the substrate to NWs. The obtained lifetimes are still shorter than the radiative lifetime of the (D^0,X_A) transition of ~1 ns reported from thick strain free nominally undoped bulk GaN.[60] Hence, for the NWs a non-radiative channel seems to be active.

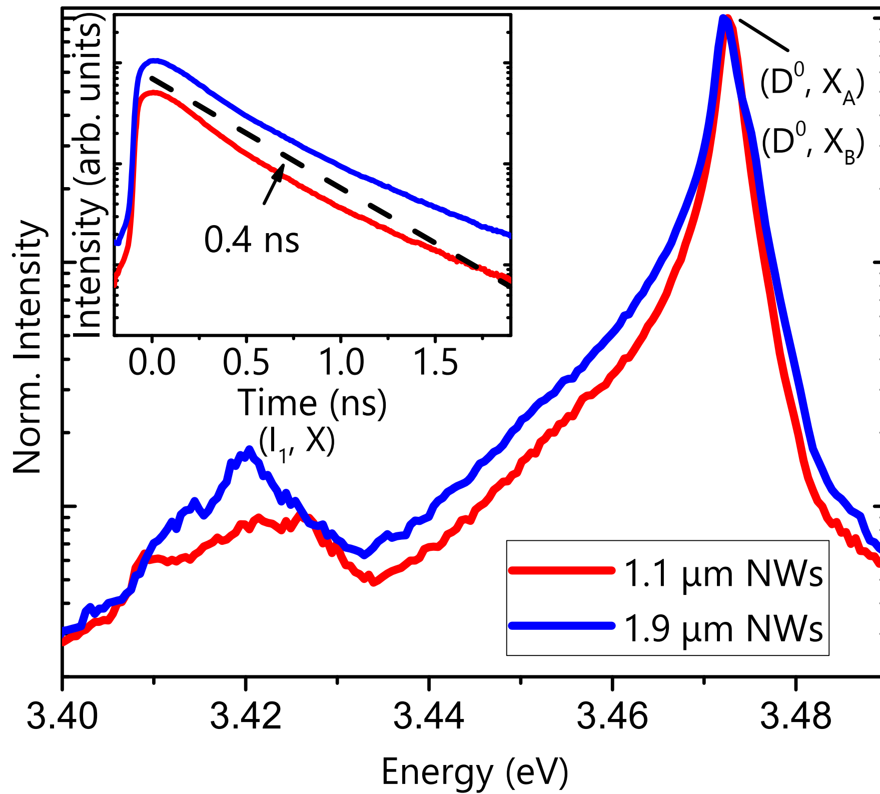

Figure 4.10: Normalized low-temperature (10 K) μ-PL spectra of the GaN NWs grown on TiN_x (Sample G1 (red) and sample G2 (blue)). Both samples are dominated by the recombination of A excitons bound to neutral donors $[(D^0,X_A)]$. Time-resolved PL transients of the (D^0, X) transition and the linear fitting (dashes) corresponding to 0.4 ns (dashes) are shown in inset.

4.1.1 Two-step growth, the key for high-temperature growth of GaN NWs on TiN_x film

After achieving very promising results with GaN NWs grown on TiN_x, I tried to even improve the crystal quality of GaN NWs further by performing additional experiments using higher growth temperature. As for it, keeping the previous Ga and N fluxes, I increased the growth temperature to 750 °C (sample G3). However, the result was not as it was expected. As in bird view SEM image in Figure 4.11(a-c) is shown, there are lots of tilted NWs. This is undesired since they might coalesce together and generate crystal defects. The density of NWs in the center of the sample is much less than middle and edge since the temperature in the center is higher (due to geometry of the heater). At this temperature the flux of desorbed Ga atoms from the sample is considerably increased but still less than the arriving Ga flux to the sample (otherwise no growth would happen on this sample). The incubation time (measured by RHEED) is 3 min which is three times longer than the one measured for the samples G1 and G2. It means, due to higher substrate temperature, longer time is required to form stable GaN nucleus. This longer incubation time, means longer absence of GaN nucleuses which increases the risk of Ga-Ti intermix. To prove this idea and solve the problem of tilted NWs, I stablished a two-step growth experiment. In this experiment, at first step, I open the Ga and N shutters at 730 °C for 2 min (short incubation time), in order to quickly form the GaN nucleuses (which minimizes the Ga-Ti intermixing due to cross capturing of Ga adatoms by initial GaN nucleuses). Then after seeing the RHEED pattern of GaN, I increase the substrate temperature to 750 °C and continuing the growth for 2 hrs. In this way, it is possible to perform higher temperature GaN NWs growth without increasing the amount of tilted NWs. In Figure 4.11(d-f) the bird view SEM images of vertical GaN NWs grown by two-step growth is shown. Comparing to Figure 4.11(a-c), it is possible to see the considerable improvement in the growth of vertical NWs (and avoiding tilted NWs), by simply doing two min low-temperature nucleation.

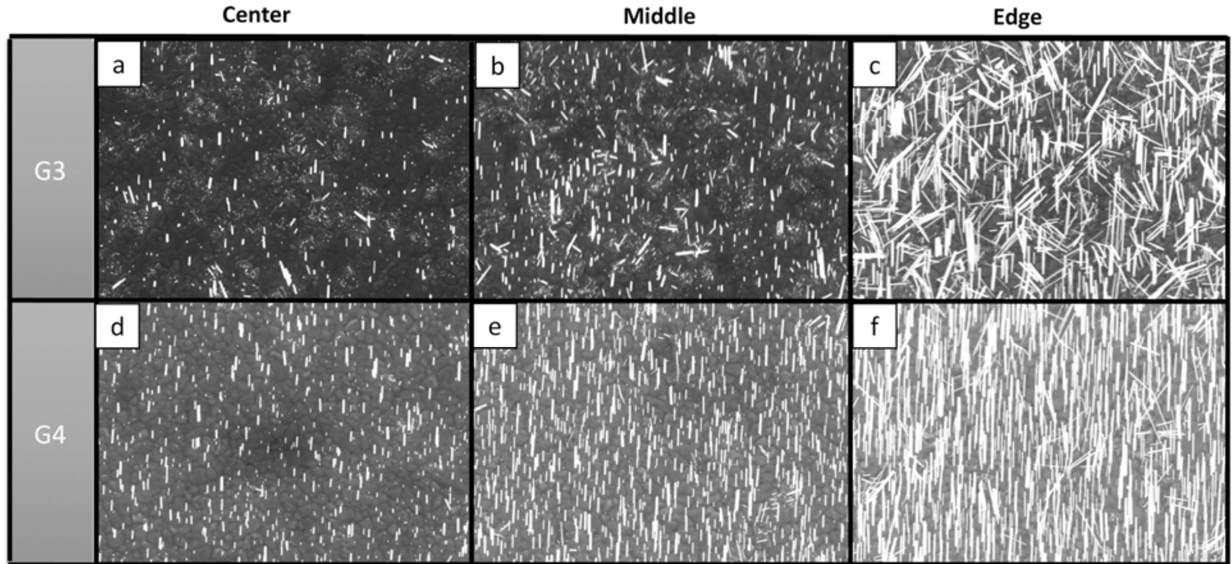

Figure 4.11: GaN NWs Bird view SEM images taken from center, middle, and edge of: (a-c) sample G3, and (d-f) sample G4. The amount of tilted NWs is reduced drastically in sample D due to two-step growth.

After this improvement in NWs morphology by benefiting from two-step growth procedure, I decided to grow another sample (sample G5) in higher temperature. Since samples G3 and G4 have been already grown with very low density (in the center), slightly increase in the temperature can prevent the growth (the Ga desorption rate becomes faster than Ga incorporation). Hence, I increase the Ga flux to 2.6 $\times 10^{15}$ atoms/cm^2.s (which is the maximum flux can be provided by simultaneously using both Ga cells in our MBE system) to compensate the desorbed Ga flux in the higher temperature. So to grow sample G5, at first I open the shutter of the first Ga cell (supplying similar flux to previous samples) for 2 min to do the fast nucleation at 730 °C. Then I increase the substrate temperature to 780 °C and wait until the GaN RHEED pattern become weak (but not disappeared). Then I open the shutter of second Ga cell to increase the total Ga flux to 2.6 $\times 10^{15}$ atoms/cm^2.s and continue the growth for ~4 hrs. The Bird view SEM image of sample G5 is shown in Figure 4.12. NWs are grown vertically, homogenously, and without coalescence.

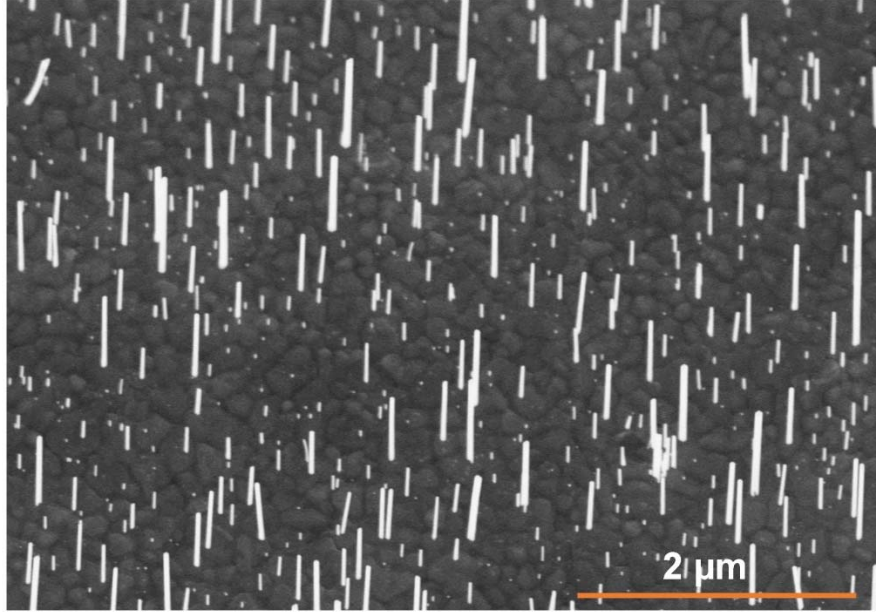

Figure 4.12: Bird view SEM image of sample G5 (GaN NWs grown on TiN_x at 780 °C).

In order to investigate the luminescence properties of the NWs, low-temperature PL and TRPL measurements are performed under the same condition which is used to measure sample G1 and G2. As can be seen in Figure 4.13, similar to sample G1 and G2, the spectra is dominated by the recombination of A excitons bound to neutral. But two sharp peaks clearly can be recognized in this sample. One at 3.4730 eV which is attributed to (O^0, X_A) and the other peak at 3.4744 eV which is attributed to (Si^0, X_A). The source of the Si bond is probably from the residual amount of Si in the chamber from the experiments done before. In the inset, the TRPL of sample G5 is shown. The sample shows 0.52 ns excitonic lifetime which is the longest lifetime has ever been observed in case of GaN heteroepitaxial growth. Comparing to samples G1 and G2, the excitonic lifetime increased, which means by increasing the growth temperature, the amount of defects (or impurities) in GaN NWs is successfully reduced. It confirms that even at such a high temperature, TiN_x-sputtered film effectively blocks the O diffusion from sapphire.

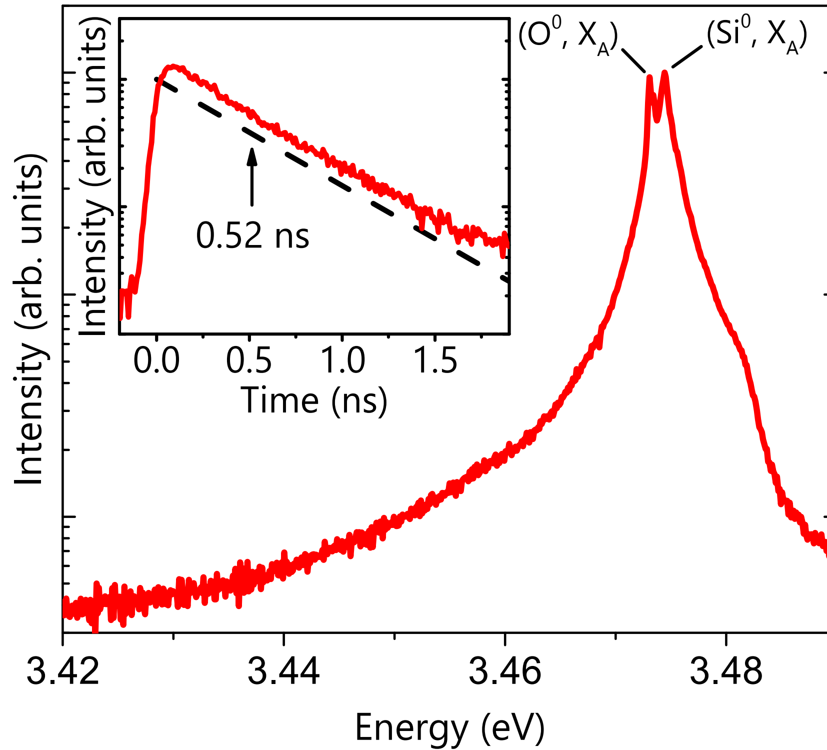

Figure 4.13: Low-temperature (10 K) μ-PL spectra of the GaN NWs grown on TiN_x at 780 °C temperature (Sample G5). It is dominated by the recombination of A excitons bound to neutral donors [(O^0,X_A , Si^0,X_A)]. Time-resolved PL transients of the (D^0, X) transition is shown in inset which is the longest lifetime has ever been observed in case of GaN heteroepitaxial growth.

The long range PL spectra of samples G1 and G5 are compared in Figure 4.14. In contrary to sample G1 (and G2), in the energy range of 3.40 to 3.43 eV, no peak is detected for sample G5. It is possibly due to successfully reduced density of stacking faults by reducing the density of NW and consequently avoiding coalesced NWs.

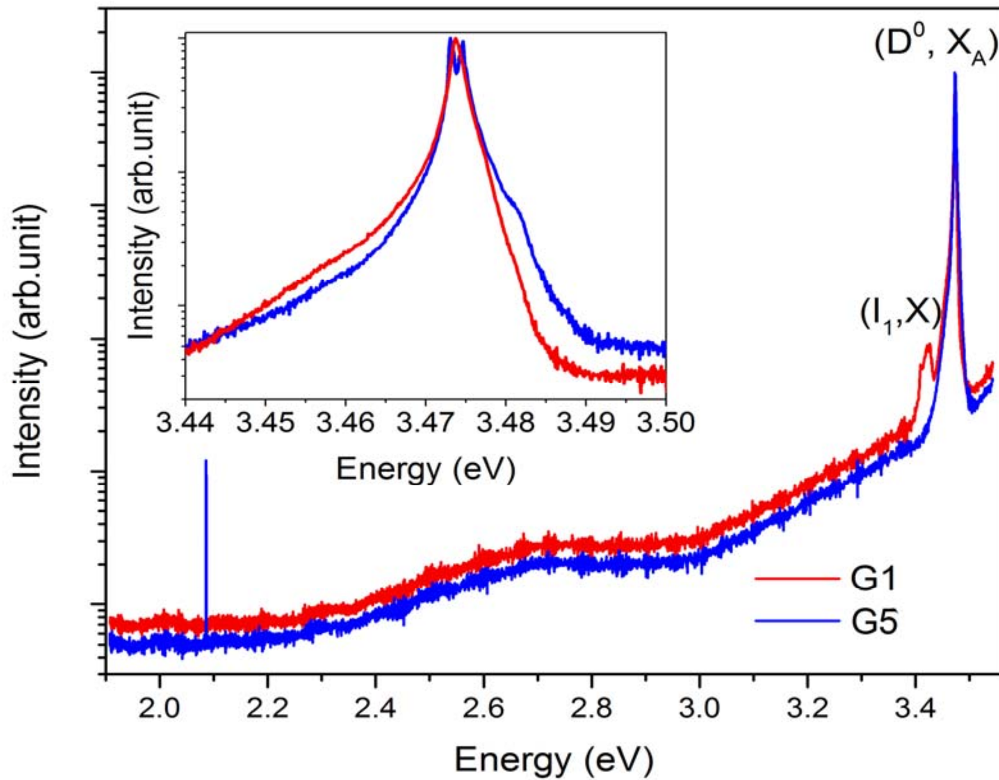

Figure 4.14: Low-temperature (10 K) μ-PL spectra of the GaN NWs grown on TiN_x at 730 °C (sample G1) (red line), and GaN NWs grown on TiN_x at 780 °C (Sample G5) (blue line). Inset: high-resolution spectra at near band edge.

4.2 Self-assembled AlN NWs growth on TiN-sputtered sapphire

Within the family of nitride semiconductors, AlN stands out owing to its large bandgap (> 6 eV), which is well suited for devices operating in the ultra-violet (UV) spectral range (360–200 nm). Having the ability for band gap engineering by alloying to Ga and In, large exciton binding energy, small electron affinity, and high thermal conductivity, AlN is an attractive material of choice for many applications such as: deep ultraviolet (DUV) optoelectronic devices, surface acoustic wave devices, microwave generation devices, and high-power electronic applications[144–147].

Analogously to the well-known case of GaN case, the lack of lattice-matched substrates significantly constrains the heteroepitaxial growth of high-quality AlN films and the related devices usually need to cope with a large density of extended defects.[148–150] An interesting

workaround is the growth of AlN in the shape of NWs. The large surface to volume ratio of these nanostructures provides an efficient channel for strain relaxation, which minimizes the formation of extended defects. However, solving the problem of lattice-mismatched substrates does not grantee the freedom in substrate choice. Finding a proper substrate for AlN NWs growth is very challenging due to the need for extremely high growth temperature. There has been only a few works using MBE to grow self-assembled vertical AlN NWs with high crystal quality and optical properties. Due to lower mobility of Al adatoms compare to Ga, higher growth temperature is required to grow AlN NWs.[40] There is yet no ideal platform for NW based UV devices, since they all rely on an initial GaN nanowire template[42], which would absorb the UV light and increase the device resistivity. Si might seem an attractive option as the substrate to grow AlN NWs on. However, the incidence matching between AlN(0001) and Si(111) lattices which is found beneficial to use AlN as buffer layer to grow GaN film on Si[151], is detrimental for the three-dimensional growth of AlN NWs on Si(111) substrate[152]. Daudin et al.[40] tried to grow AlN NWs on Si(001) by introducing an amorphous SiO_2 layer as buffer layer to get advantage of Volmer-Weber (VW) growth mode. Although they succeed to grow strain-free NWs, the NWs suffered from severe coalescence. Besides that, oxygen impurities from SiO_2 decomposition at elevated temperatures is very likely. In a different approach, Yanxiong et al.[41] grew AlN NWs on Si_3N_4 on Si(111) layer. However they faced Si incorporation in Al NWs and also limitation in the density of NWs. Besides that, Si and Al are known to have a low eutectic temperature[153] (for instance, in industry Al-Si alloy is used as brazing compound) which adds restriction to the aluminization process. Zhao et al.[154] used GaN NW template on Si substrate to grow AlN NWs. It was found that there is a growth temperature limitation (800 °C) as GaN NWs partially decomposed at the high growth temperature required for the growth of AlN NWs.

In search for a proper substrate to grow AlN NWs, TiN seems very promising, considering its high temperature stability (melting point = 2930 °C)[155], excellent electrical and thermal conductivity[133,156], and high optical reflectivity up to the UV range, which is beneficial for applications like LEDs based on NW ensembles.[127,129–131] Moreover, TiN sputtering technology has been well-developed.[136,157] By attaching the sputtering chamber to the MBE, we can open up the possibility of growing NWs on a surface which is produced in vacuum and never exposed to air.

In this work, I benefit from TiN high thermal stability as the substrate to do high-temperatures growth of self-assembled AlN NWs.

The same sputtering and MBE systems which are used for GaN NWs growth are used here to grow AlN NWs. To prepare the substrate, 0.8 μm thick TiN film is deposited on 2-inch Al_2O_3 (0001) substrate, using a magnetron sputtering system with 3×10^{-10} Torr base pressure. Sputtering of TiN is carried out for 40 mins at 10^{-3} mbar sputtering pressure by injecting 12 ± 0.2 sccm Ar and 3 ± 0.18 sccm N fluxes and applying a DC power of 500 W to generate the plasma. A 3-inch Ti disk is used as the target. During the sputtering an additional 100 V bias voltage is applied to the substrate to improve the physical properties of TiN film[133]. Without exposing to air, the TiN-sputtered sapphire is transferred to the growth chamber of a plasma-assisted MBE with a base pressure of 8×10^{-11} Torr. In the MBE, the growth of AlN NWs on the TiN film is performed. To measure the substrate temperature, the pyrometer is calibrated using the 7×7 to 1×1 Si transition temperature (860 °C)[64]. To grow AlN NWs two different recipes are used. At first, sample A1, for 5 hours at a substrate temperature of 1160 °C (measured by pyrometer facing the center of the substrate considering 0.23 as the emissivity of TiN at this temperature[158]) using an Al flux of 1.4 $\times10^{14}$ atoms/cm^2.s (0.06 ML/s) supplied by a conventional Knudsen cell, and an active N flux of 2.2 $\times10^{15}$ atoms/cm^2.s (1.07 ML/s), supplied by RF plasma source operating at 500 W and 2.5 sccm N_2. However, the AlN NWs grown by this recipe, show rather cone shape than NWs (Figure 4.15). They had also very rough facets, as can be seen in cross view TEM image shown in Figure 4.15b.

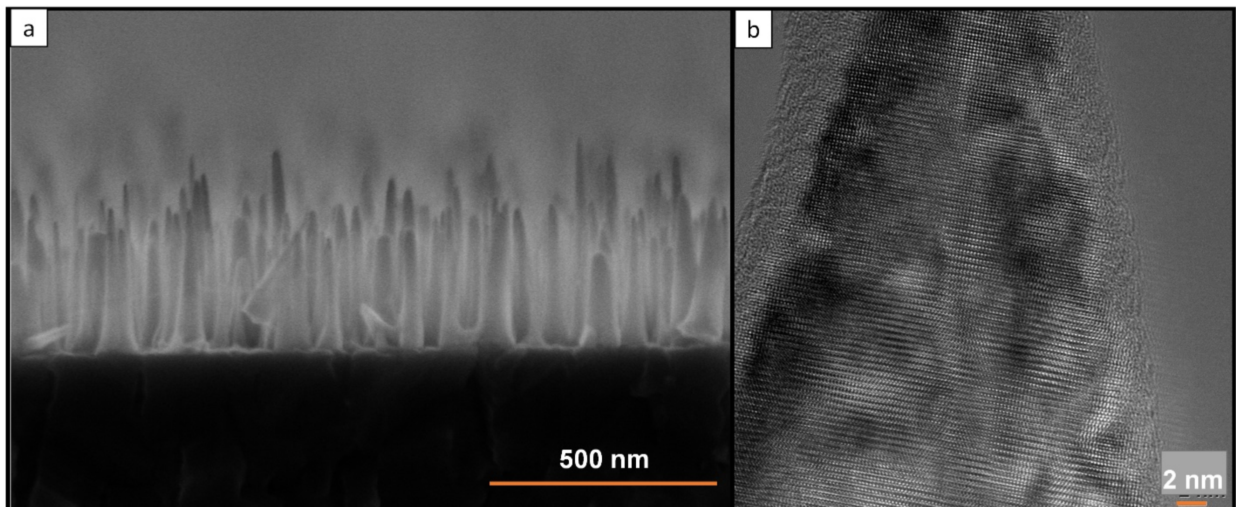

Figure 4.15: (a) Cross view SEM and (b) High resolution TEM images of sample A1.

To improve the morphology of NWs, an additional sample (sample A2) is grown for 5 hrs at substrate temperature of 1180 °C using an Al flux of 2.9 $\times 10^{14}$ atoms/cm^2.s (0.14 ML/s) and the same N flux as sample A1. Prior to growth of AlN NWs, the TiN was nitridized for 25 mins starting at 930 °C while continually increasing the substrate temperature to 1180 °C. The Al shutter is then opened and the first AlN related diffraction spots are observed by RHEED, 20 mins later. It evidences the existence of an incubation time as typically reported for GaN NWs growth[159,160].

As it is shown in Figure 4.16, there is a significant difference in the shape of NWs by increasing the growth temperature and Al flux.

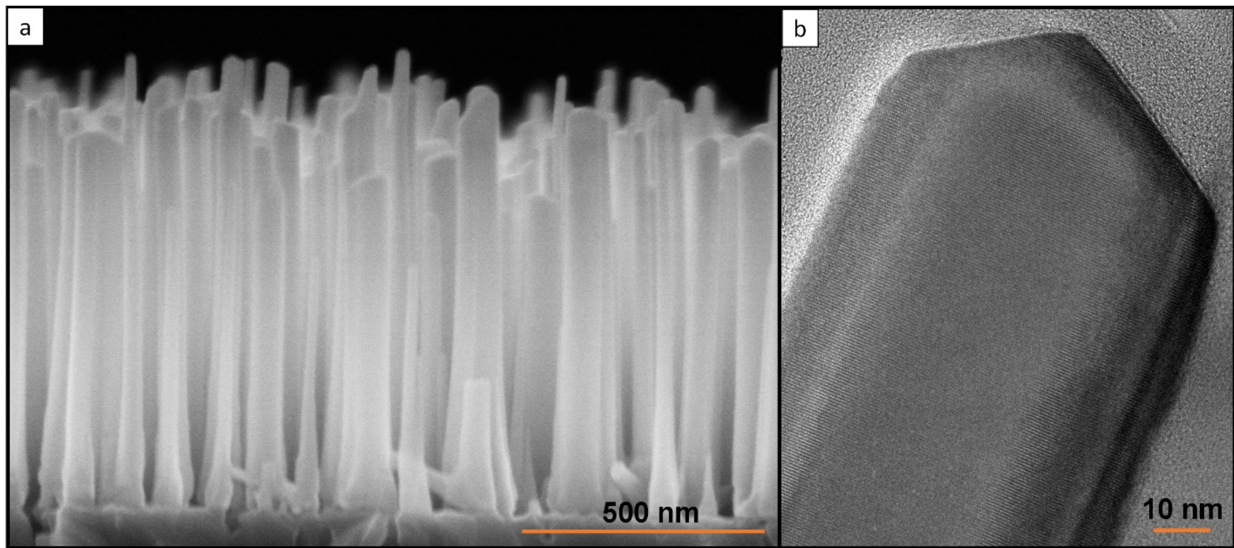

Figure 4.16: (a) Cross view SEM and (b) TEM images of sample A2.

After the growth, the sample characteristics are studied, investigating: the morphology and density of the NWs by SEM; microstructure and crystal quality of dispersed NWs by TEM at 200 kV; the crystalline phases as well as strain, tilt, and twist of NWs by XRD using Cu Kα1 radiation (wavelength $\lambda = 1.54056$ Å) and a diffractometer equipped with a Ge(220) hybrid monochromator; strain in AlN NWs as well as Ti/N ratio in TiN sputtered film by room temperature Raman spectroscopy using laser energy of 2.62 eV; the TiN film electrical properties by Variable-angle spectroscopic ellipsometry at room temperature and 4-probe Van der Pauw measurements; To study luminescence properties of AlN NWs, the wavelengths of lasers which are available in PL

lab of PDI are not sufficient to excite AlN (due to its very wide band gap). So instead of PL, CL (low-temperature, at acceleration voltage of 5 kV) is used in this study.

SEM Bird's eye and top view images of AlN NWs grown on TiN film are shown in Figure 4.17(a) and Figure 4.17(b), respectively. The growth of NWs is perfectly homogenous (from center of sample to edge), with NWs density about 2×10^{10} cm^{-2} and filling factor of 35%. As it can be seen, the NWs are aligned vertically to the substrate. They are 850 nm high on average and their mean diameter is 55 nm. As the growth of NWs is done in N-rich condition, the growth rate is limited by Al flux. However from the length of NWs, it is found that the NWs growth rate is ~33% higher than what was expected for AlN planar growth (even by considering the planar growth in full condensation regime). It means, in addition to the direct impingement of atoms at the tip of the NWs, there is a significant contribution of adatoms diffusion through the sidewalls towards the tip. This phenomenon was explained previously in case of GaN NWs growth[161,162]. However when it comes to the AlN NWs grown on GaN NWs, the story was different due to the temperature limitation as Songmuang et al.[161] reported, the Al adatoms diffusion through the sidewalls found to be negligible at 790 °C, which caused to AlN NWs gradual diameter increase from ~30 to ~200 nm.

Following the method proposed by Brandt et al.[163] I extract from the circularity of the NWs top facet a coalescence degree of 30--47 %, by respectively using a threshold value of 0.653--0.762. Such coalescence degree is lower than for typical GaN NWs grown on bare Silicon[163], but is larger than for GaN NWs grown on Ti-sputtered sapphire[127]. It suggests that lower coalescence degree can be obtained for AlN NWs through a systematic optimization of the growth parameters.

In order to investigate the microstructure of AlN NWs, a HRTEM is employed. Although the TEM images from the interface of AlN/TiN (not shown here) indicates some defective (mostly dislocations) areas which are extended to the bottom of NWs, they become free of dislocations by moving toward the tip of NWs. Figure 4.17(c) shows the side view bright field TEM image taken from top of an individual AlN NW. It looks defect-free and with well-defined side-facets.

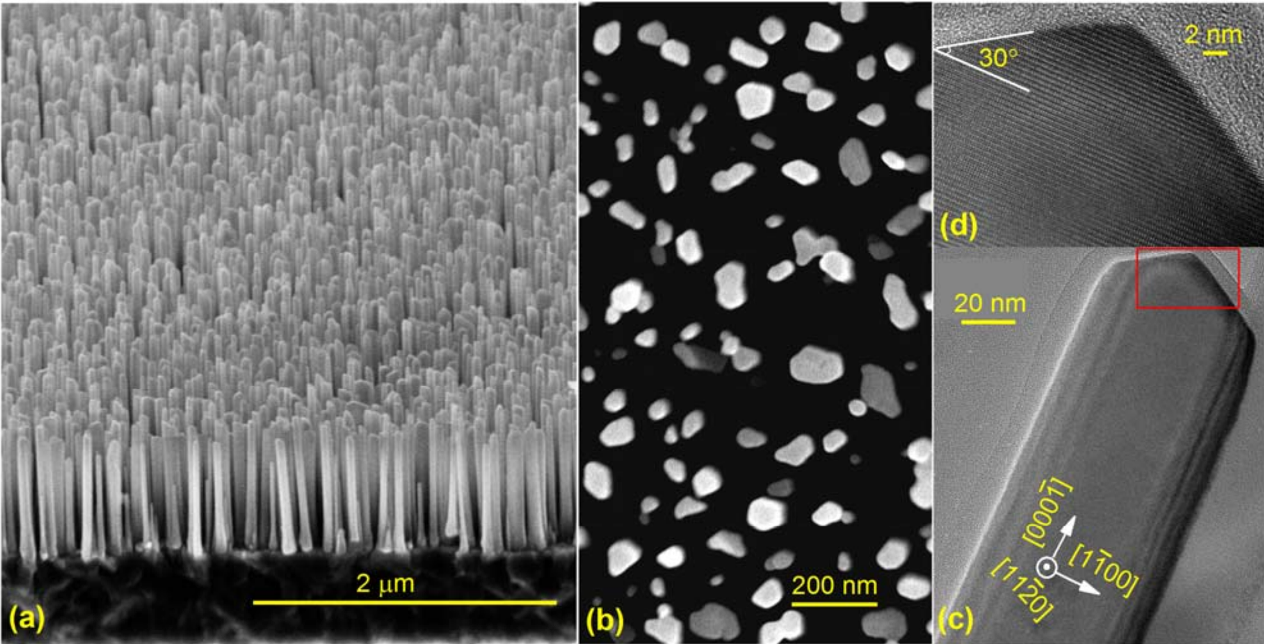

Figure 4.17: (a) Bird's view and (b) top view SEM images of AlN NWs grown on TIN film (sample A2), (c) Cross section bright field, (d) High-resolution TEM images from the tip of a dispersed AlN NW.

As shown in Ref.[164], the combination of SEM imaging and X-ray pole figures of the NWs allows to identify the NW facets (Figure 4.18). Remarkably, $\{11\bar{2}0\}$ side-walls are found, although the surface energy of these planes is larger to than $\{1\bar{1}00\}$ according to the calculations done in Ref.[165]. It also contrasts with the case of GaN NWs. It suggests a strong kinetic control during the AlN NW growth.

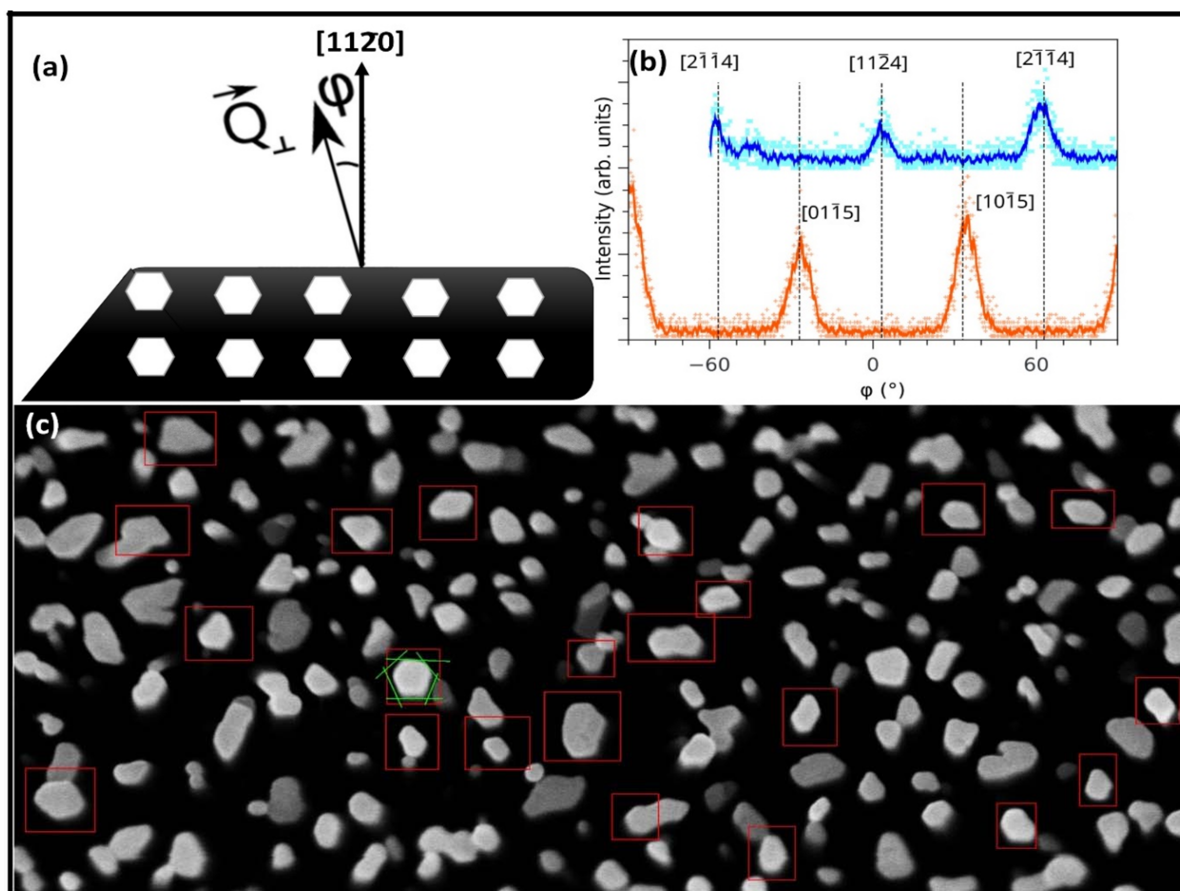

Figure 4.18: (a) Schematic of a piece of sample A2, used for SEM and XRD measurement showing the cleaved edge crystallographic direction. (b) XRD phi scan demonstrating the cleaved edge (mounted at 0°) is parallel to [11$\bar{2}$4] plane. (c) Top view SEM image of AlN NWs taken under the same twist (Φ) used in XRD measurement. The details of this method is reported in Ref. [164].

In Figure 4.17(d), High resolution TEM image from tip of the AlN NW (zoomed on the selected area by red rectangular in Figure 4.17(c)) demonstrates defect-free single-crystalline wurtzite structure. Considering the top facets with 30° (±1°) angle respect to growth direction, the top facets can belong to {11$\bar{2}\bar{5}$} or {1$\bar{1}\bar{0}\bar{3}$} family of planes with respectively 29° and 31.64°angle respect to {0001} as depicted in Figure 4.20(a-c).

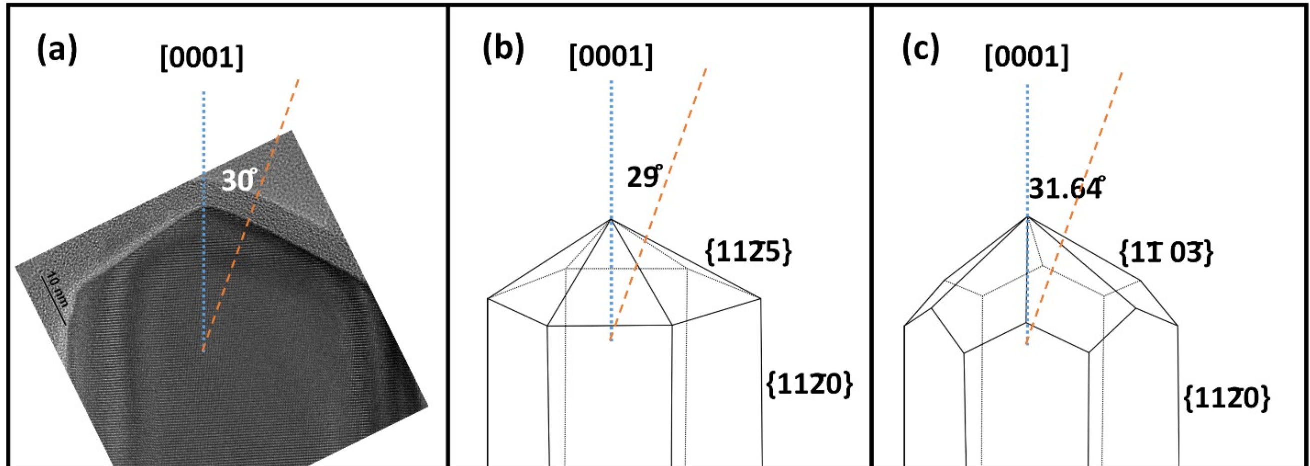

Figure 4.19: (a) Cross view high-resolution TEM image from AlN NW's tip. (b) And (c) the schematic of two possible families of planes corresponding to the NWs top facets.

Since AlN have the hexagonal wurtzite structure, it consist of alternating layers of Al-N pairs, stacked along the [0001] direction in an ABABAB sequence. Thus, the basal plane (i.e. the (0001) plane) can be either N- or group Al polar. The crystal polarity can be identified after wet etching since the amount of material removed and the resulting surface morphology is polarity dependent[166]. Polarity dependence of etching behavior for an AlN epitaxial layer grown on sapphire substrate were reported by Jasinski et al. The etch rate of the Al-polar crystal was much slower than that of the N-polar crystal in a 50 wt.% aqueous KOH solutions at 80 °C.[167]

Similarly, I used KOH etching method in order to determine polarity of the grown AlN NWs. As for it, a small pieces of sample, is soaked in 70° C, 5 Molar KOH for 30 s, 60 s, and 120 s. From cross view SEM images (Figure 4.20), we can easily see how fast the NWs are etched. After 2 min there is no NW remained on the surface. From this experiment I conclude the NWs are N-polar.

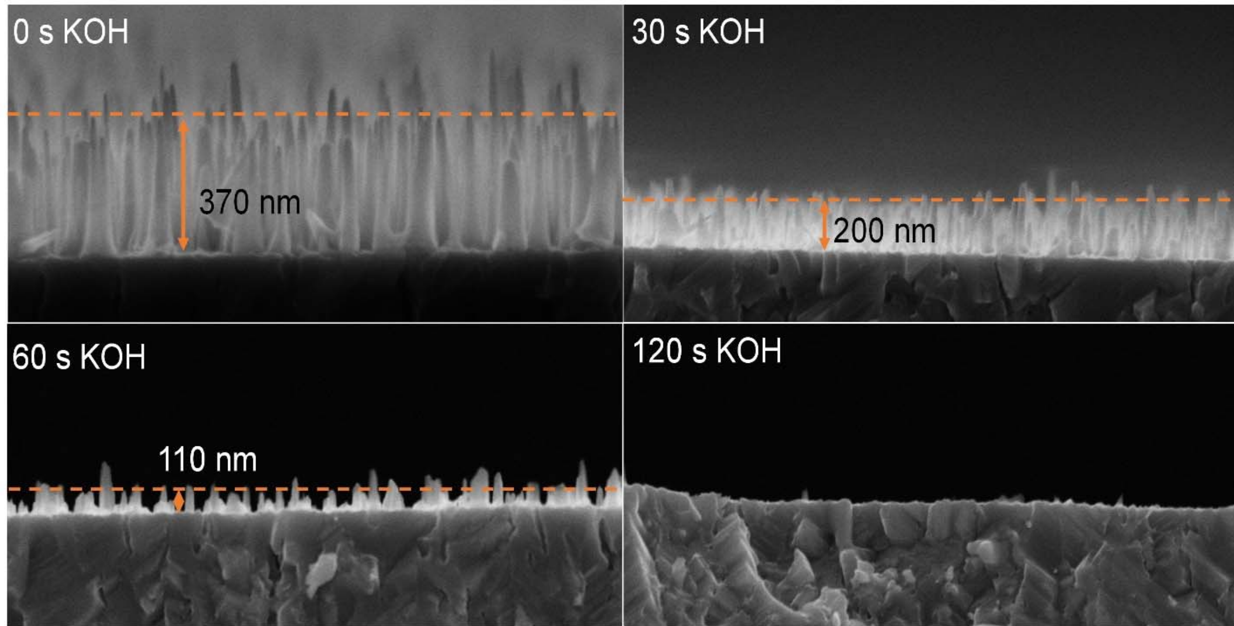

Figure 4.20: Cross view SEM images from AlN NWs after: 0, 30, 60, and 120 s etching in 5 M KOH solution to determine NWs polarity.

Figure 4.21 Demonstrates (a) real part (⟨ε1⟩) and (b) imaginary part (⟨ε2⟩) of pseudodielectric function of TiN sputtered film measured by variable-angle spectroscopic ellipsometry. The behavior of ⟨ε1⟩ and ⟨ε2⟩ at low photon energies is characteristic for a metal. Moreover, comparing the value of photon energy (≈ 2.6 eV) when ⟨ε1⟩ crossing zero, with literature[135,136] confirms the TiN sputtered film is stoichiometric. The stoichiometry of TiN sputtered film is also confirmed by Raman spectroscopy of the sample after the growth of AlN NWs (Figure 4.21(c)), considering the position of low frequency acoustic phonon peak (TA) at 200 cm^{-1}, in agreement with Ref.[Spengler1978][137]. It is explained the position of low frequency acoustic phonon is characteristic for determination of TiN_x composition. The non-stoichiometric TiN_x peak will shift to higher or lower frequencies by changing the composition toward Ti-rich or N-rich, respectively. Another important information can be extracted from Raman spectroscopy, is the high-frequency E_2 mode peak position of AlN which is sensitive to the strain in the crystal as explained in litrature[168,169]. Compering this sharp E_2 mode peak of our AlN NWs at 655.5 cm^{-1} with their results confirms the NWs are relaxed.

The sputtered TiN film resistivity as low as 3×10^{-4} Ωcm is measured in room temperature using 4-probe method which is consistent with previously reported values of TiN[133,156] and confirms the

metallic conductivity of TiN-sputtered film. Having NWs grown on a metallic substrate is very important for their applications since it makes possible NWs back contact.

XRD Measurements around the AlN(0002) Bragg peak is carried out, using Al_2O_3(0006) peak from the substrate as reference. ω–2θ scan of sample A2 is shown in Figure 4.21(d) demonstrating wurtzite AlN(0002) sharp diffraction peak at θ=18.009° (corresponds to c_AlN lattice constant of 0.498 ± 0.002 nm) with FWHM of 40 arcsecond and TiN(111) diffraction peak at θ=18.362° with FWHM of 180 arcsecond. As was expected, TiN film has cubic structure grown in [111] direction. No signal from TiO or Ti_2O is detected, which indicates TiN successfully damps the oxygen diffusion from Al_2O_3 to the AlN NWS even at such a high temperature.

By including more than one Bragg reflection for the AlN nanowires and the substrate, which allows for a precise lattice parameter determination, the c[AlN] = 0.49835 +- 0.00005 nm is determined, which is slightly higher (strain = 5E-4) than the recent values reported for bulk or freestanding AlN (c[AlN] = 0.49808 nm, reported by Nilsson et al[170]).

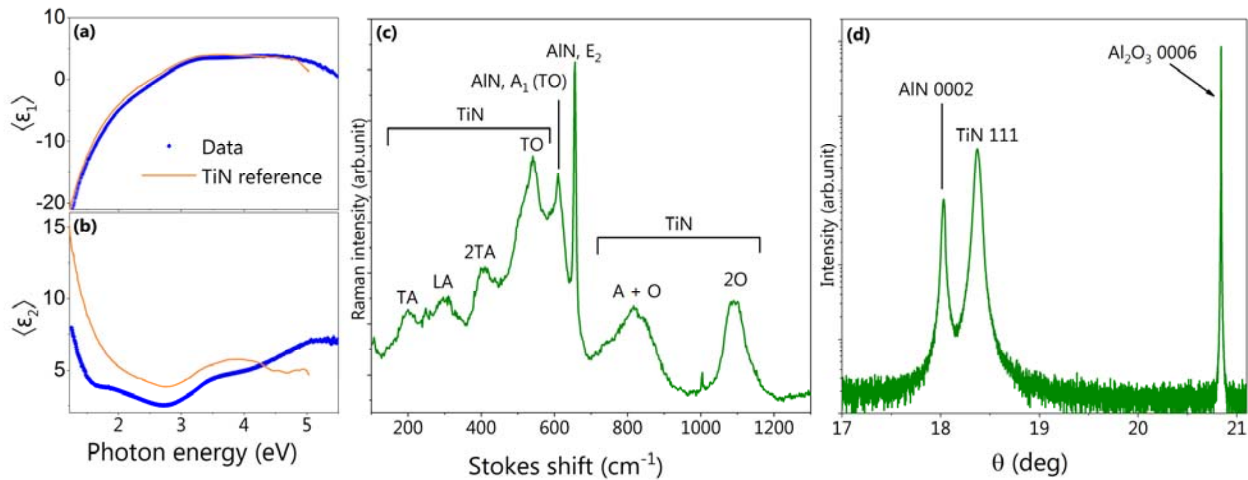

Figure 4.21: (a) Real and (b) Imaginary parts of the pseudo dielectric function obtained by spectroscopic ellipsometry for TiN sputtered film (blue line) and studied by Langereis et al.[139] (c) Raman spectroscopy and d) X-ray diffraction of the sample after growth of AlN NWs.

Furthermore, XRD rocking curves (Figure 4.22) around AlN(0002) and AlN($1\bar{1}00$) reveals an average tilt and twist about 1.7 and 2.1 degrees respectively.

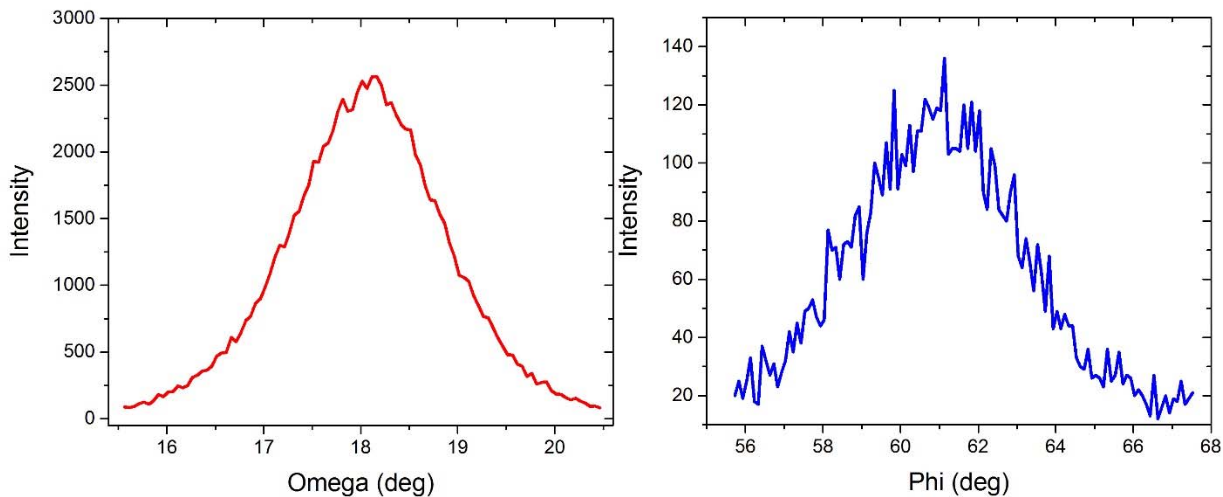

Figure 4.22: XRD Omega and Phi scan of sample A2, to determine the tilt and twist of AlN NWs grown on TiN.

Since the required energy to excite AlN is very high, instead of PL, CL spectroscopy is used to investigate the luminescence properties of the AlN nanowires. The measurements are carried out with a Gatan MonoCL4 system fitted to a Zeiss Ultra55 field-emission SEM. The SEM is operated at 5 kV with a beam current of around 20 nA. The samples are cooled at 10 K and their luminescence is collected using a parabolic mirror, dispersed using a spectrometer (focal length of 30 cm; 1200 lines mm^{-1} grating blazed at 250 nm; slits of 0.1 and 0.3 nm for the bulk (as the reference) and NW samples, respectively), and detected with a high sensitivity photomultiplier tube. Even though, the system is equipped with reflective optics for improved UV light transmission, the responsivity in the UV spectral range is significantly reduced. Therefore, the reported overview spectra are corrected using the instrument response function.

The sample is measured side-by-side with a piece of free-standing bulk AlN [courtesy of M. Bickermann, Leibniz Institute for Crystal Growth] featuring narrow excitonic lines with well reported energies[171], allowing for a precise calibration of the energy scale. The 10 K CL spectra of both the bulk sample and the AlN nanowires are shown in Figure 4.23. The band-edge CL of the AlN nanowires can be fitted by taking into account a dominant donor-bound exciton (D^0,X_A) at 6.01 eV and a minor free A exciton (X_A) at 6.03 eV accompanied by two optical phonon (OP) replica spaced at about 85 meV. Oxygen is likely acting here as shallow donor in the AlN

nanowires (O^0X at 6.006 eV[172]). The phonon replica can correspond to surface-optical phonons rather than longitudinal-optical (LO) phonons as already reported by Wang et al.[154] for NW ensembles. Luminescence from a deep state is visible at 3.9 eV both for the AlN nanowires and the bulk AlN and is attributed to C substitutional to N atoms[173].

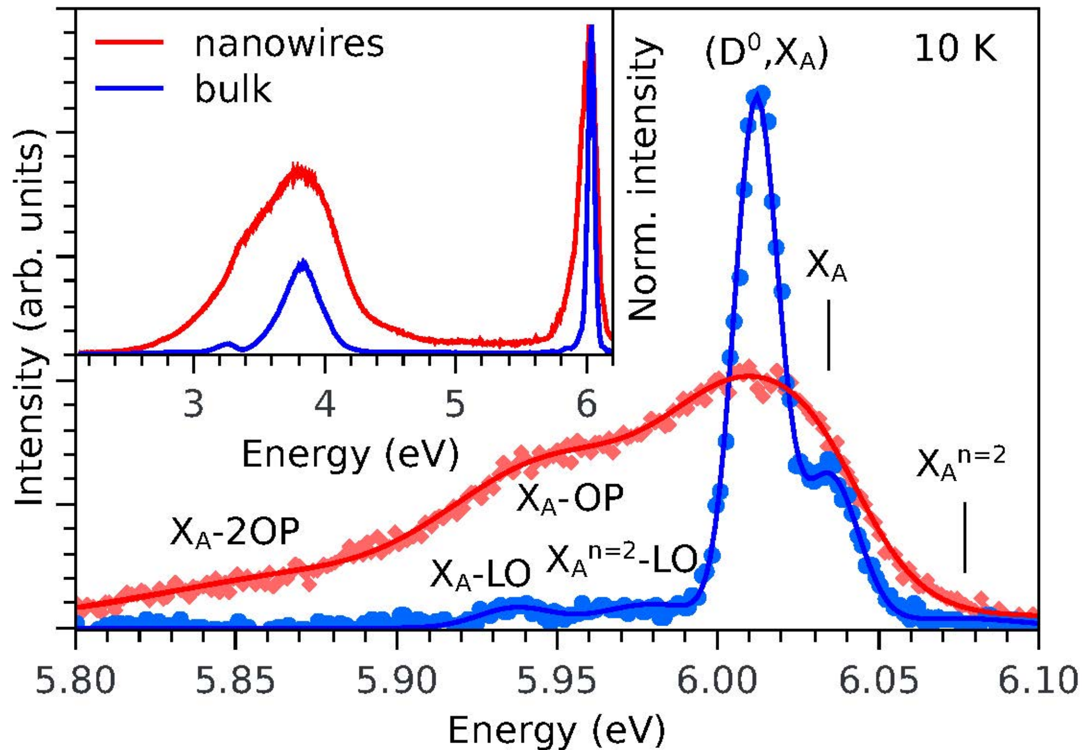

Figure 4.23. Low temperature CL spectra of the ensemble of AlN NWs grown on TiN (sample A2) (red line) compared with the one of bulk AlN. The attribution of the excitonic lines in the bulk AlN is based on Ref.[171].

Summary, Conclusions, and Outlook

In this thesis the PA-MBE growth and characteristics of different families of III-N semiconductors are discussed. The two main issues preventing realization of III-N full potential are addressed to be the difficulty in obtaining high-In-composition InGaN crystals, and the existence of huge densities of defects in heteroepitaxially-grown III-N semiconductors.

In case of InGaN thin-films grown on highly lattice-mismatched Si(111) substrate, the properly removing native oxides from Si surface and then nitridation at high temperature, is shown to effectively improve the crystallinity of InGaN layers.

As a solution to obtain high-In-composition InGaN thin-films, low-temperature growth is explained. In this approach a good composition control is easily achievable by keeping the III/N ratio below unity. However this condition promotes the columnar growth and consequently very rough surface. On the other hand the InGaN thin-films grown by III/N ratio above unity show very flat surface but suffer from metal atoms accumulation on the surface and formation of metal droplets. The formation of these metal droplets strongly affect adatom incorporation dynamics, making the growth rate a decreasing function of metal flux impinging on the surface. This is in marked contrast to the common assumption that the growth rate under metal rich conditions is determined by the N flux. Hence, the common N flux calibration procedure under metal-rich conditions has to be reconsidered.

Moreover, the presence of the droplets on the surface activates the VLS crystal growth under the droplet. This relates to direct impingement of N onto the droplet. Our findings show that this growth method is faster than the normal crystal incorporation and promotes, at long times, a recovery of the growth rate in samples with high droplet coverage. The VLS growth mode dominates the dynamics when the droplet coverage reaches a sizeable percentage of the surface. I explain this phenomenon via a model that takes into account droplet effect as depletion sites on the incorporation of metal adatoms into the crystal.

It is found that metal droplets also strongly effect the InGaN composition. A drastic reduction of In incorporation into InGaN crystal is observed, as soon as metal droplets are formed. The higher surface is covered by metal droplets, the less In is incorporated into the InGaN crystal. I attribute this phenomenon to: First, VLS growth under the droplets (because of preferential Ga-N binding

respect to In-N), and Second, the higher In atoms mobility on the surface that increases the possibility of being captured by metal droplets (and not incorporate into InGaN crystal).

There is only a narrow window where is possible to grow droplet-free and flat InGaN thin-film while having a good control on the composition. The best epilayer characteristics, in terms of surface roughness, are found in the samples grown at metal flux just below the onset of droplet formation (Intermediate regime). In this regime there is no metal droplet on the surface and the surface morphology is flat and homogenous. The microstructure of this sample shows RMS roughness as small as 0.86 nm in a scan field of 4 μm^2. Finding the growth window where is possible to form a droplet-free and flat InGaN surface, opens up the way to a more sophisticated engineering of InN QDs on InGaN, and is of great importance for applications like: photo electrochemical water splitting, bio-sensors, and green and red LEDs.

Raman spectroscopy as a fast and simple alternative method for XRD and PL, with ability of local measurement, can be used to measure the InGaN composition. In this study, by filling the gap of data in literature for the x values (Indium percentage) between 30%-65%, it is found that in contrary to the linear dependence of A_1 (LO) with In fraction reported in the literature, in the central zone of InGaN it follows a polynomial relationship with a bowing toward higher frequencies in the middle region. These results complete the available literature and add a convenient method for the determination of local properties of InGaN films and nanostructures within this region of composition.

In the second part of my thesis (chapter 4), I discussed the fabrication of GaN and AlN nanowires on sputtered TiN. In-situ prepared TiN film, makes very promising substrate to grow III-N NWs in high temperature. High-quality self-assembled vertical GaN NWs and AlN NWs are grown on TiN_x-sputtered sapphire. In contrast to the common unintentional doping problem of NWs by impurity-diffusion from substrate, TiN film prevents the impurity diffusions from sapphire to NWs even in extremely high growth temperatures. Benefiting from refractory TiN and its compatibility to the growth condition, it is possible to increase the growth temperature which leads to improvement in crystal quality of NWs. Moreover, TiN films exhibits metallic conductivity and forms an Ohmic contact to NWs which can be used as back contact or mirror.

The self-assembled vertically grown non-coalesced GaN NWs on TiN_x-sputtered film, have shown the longest excitonic life-time (0.52 ns) has ever been achieved by heteroepitaxially grown GaN. This unprecedentedly long lifetime indicates a reduced density of non-radiative point defects

and/or reduced surface electric fields promoting excitons dissociation, both as a consequence of the absence of contamination from the substrate. We thus advocate the use of in situ sputtered TiN_x films as a nucleation layer for the high temperature growth of uncoalesced GaN NWs with minimized impurity incorporation and reduced density of native point defects. These GaN NWs can make promising templates for the realization of well-defined GaN QDs embedded in GaN-AlN core-shell heterostructures, whose properties may prove useful for applications such as single-photon emitters.

Moreover, self-assembled vertically aligned AlN NWs are grown on TiN-sputtered sapphire. AlN NWs are grown nearly free of coalescence and homogenously all over the sample. The incubation time of AlN on TiN in 1180 °C is found to be 20 mins. A significant contribution on growth rate by Al adatom diffusion along the NW sidewalls is observed. They have single-crystalline defect-free wurtzite structure with side and top facets. In contrasts with the case of GaN NWs, AlN NWs side facets are determined to be $\{11\bar{2}0\}$ (a-planes) which has higher surface energy respect to $\{1\bar{1}00\}$ (m-planes) which suggests a strong kinetic control during the growth.

For AlN NWs top facets (with 30° (±1°) angle respect to growth direction) two possible families of planes $\{11\bar{2}5\}$ or $\{1\bar{1}0\bar{3}\}$ are recognized.

Due to lack of suitable substrate, such high temperate heteroepitaxial growth of AlN has not been achieved before. AlN NWs grown on TiN, exhibit optical properties dominated by band-edge emission. Such self-assembled AlN NWs grown on TiN films constitute a promising quasi-substrate to host high quality AlN/(Al,Ga)N heterostructures for the realization of efficient devices operating in the deep UV range.

Failures

'Success only comes by persevering despite failure'

Here I list some of the failed experiments during my PhD work.

- The MBE growth of InGaN on Si(111) without properly removing the native oxides from the Si surface, ended to polycrystalline InGaN. Observation of 7×7 Si surface reconstruction can grantee the oxide layers are properly removed.

- The MBE growth of InGaN on Si(111) without nitridation process ended to polycrystalline InGaN (explained in chapter 3).

- To grow GaN NWs, at first I tried the stoichiometric TiN (sputtered on sapphire). In typical growth temperatures the nucleation of GaN on stoichiometric TiN film didn't occur (the incubation time was infinity). After reducing the substrate temperature to lower temperatures, nucleation happened, but instead of NWs, GaN grew in the shape of thick blocks (Figure F1).

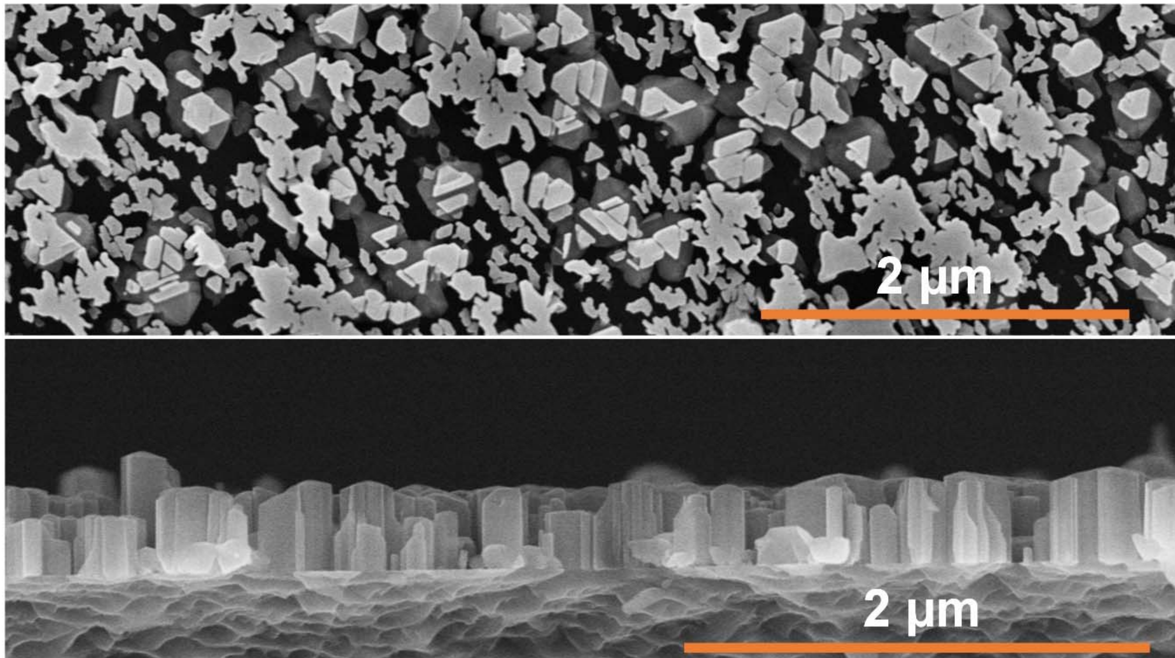

Figure F1: SEM image top view (top) and cross view (bottom) of GaN blocks grown on TiN.

- After failing to grow GaN NWs, I tried to have two-step sputtering process. At first step I sputtered 0.8 μm stoichiometric TiN on sapphire as the barrier to prevent oxygen diffusion from sapphire to NWs (as explained before, the problem of oxygen diffusion from sapphire to NWs is considered as the major problem with GaN NWs grown on Ti-sputtered[132] sapphire). At second step I sputtered 0.8 μm Ti film on top of the sputtered TiN film. The reason of this second layer is we were expecting GaN NWs should grow on Ti without any problem (sine many papers have already reported the growth of GaN NWs on Ti[127,128,132]). But surprisingly there was not possible to nucleate on this surface. The reason is not clear for us and needs further studies. I repeated this two-step sputtering process with 0.8 μm stoichiometric TiN and a very thin Ti film (about 50 nm) on top of that. But it failed again.

- In case of AlN NWs, after successful results of growing self-assembled AlN NWs on TiN-sputtered sapphire, to benefit from direct integration on Si, I tried to grow AlN NWs on TiN film sputtered on Si(111) substrate (just replacing sapphire with Si). However, due to very high growth temperature, Si surface was degraded and peeled off.

Publications and conferences

Articles

1- M. Azadmand et al. **Droplet controlled growth dynamics in molecular beam epitaxy of nitride semiconductors**. Sci. Rep. 8, 11278 (2018).
2- M. Azadmand et al. **Raman spectroscopy of epitaxial InGaN/Si in the central composition range**, (article submitted to JJAP).
3- M. Azadmand et al. **Heteroepitaxial growth of smooth InGaN single crystalline layers on Si(111)**. (article ready to submit).
4- M. Azadmand et al., **Indium incorporation suppression by metal droplets during InGaN MBE growth**, (article ready to submit).
5- M. Azadmand et al. **High-quality self-assembled GaN nanowires on sputtered TiN_x** (article ready to submit).
6- M. Azadmand et al. **High-temperate growth of self‐assembled AlN nanowires on sputtered TiN**. (article ready to submit).

Abstracts

1- M. Azadmand et al. **High-temperate growth of self-assembled AlN nanowires on sputtered TiN**. (accepted as poster in Eurombe2019).
2- T. Auzelle, M. Azadmand et al. **Directly sputtered refractory TiN_x films as substrates for high-quality GaN nanowires** (accepted as poster in Eurombe2019).
3- M. Azadmand et al. **Heteroepitaxial growth of flat InGaN single crystalline thin layer on Si(111)**, E-MRS 2018 Fall Meeting, (selected as the best oral presentation of symposium U), (2018).
4- M. Azadmand et al. **Raman spectroscopy of InGaN in the central composition range**, Poster, IWN2018, (2018).
5- M. Azadmand et al. **Heteroepitaxial growth of flat InGaN Single crystalline layers on Si(111)**, Poster, IWN2018, (2018).

6- M. Azadmand et al. **Growth dynamics of nitride semiconductors in presence of metal Droplets**, Poster, IWN2018, (2018).
7- M. Azadmand et al. **Growth suppression by metal droplets of In0. 5Ga0. 5N/Si(111) at low temperatures**, Poster, Italian Crystal Growth (IGC2017), (2017).
8- M. Azadmand et al**. Growth Suppression by Metal Droplets of In0. 5Ga0. 5N/Si (111) at Low Temperatures**, 19th International Conference on Molecular-Beam Epitaxy (2016).

Awards

- E-MRS (European Materials Research Society) Graduated Student Award, Warsaw, (2018).

References

1. Yam FK, Hassan Z. InGaN: An overview of the growth kinetics, physical properties and emission mechanisms. *Superlattices Microstruct*. 2008;43(1):1-23. doi:10.1016/j.spmi.2007.05.001.
2. Aharonovich I, Englund D, Toth M. Solid-state single-photon emitters. *Nat Publ Gr*. 2016;10(10):631-641. doi:10.1038/nphoton.2016.186.
3. Northup TE, Blatt R. Quantum information transfer using photons. *Nat Publ Gr*. 2014;8(5):356-363. doi:10.1038/nphoton.2014.53.
4. Buckley S, Rivoire K, Vuˇ J. Engineered quantum dot single-photon sources. 2012. doi:10.1088/0034-4885/75/12/126503.
5. Alvi N ul H, Soto Rodriguez PED, Aseev P, et al. InN/InGaN quantum dot photoelectrode: Efficient hydrogen generation by water splitting at zero voltage. *Nano Energy*. 2015;13(MARCH):291-297. doi:10.1016/j.nanoen.2015.02.017.
6. Heber J. Nobel Prize 2014: Akasaki, Amano & Nakamura. *Nat Phys*. 2014;10:791. http://dx.doi.org/10.1038/nphys3147.
7. Walukiewicz W, Li SX, Wu J, et al. Structure and electronic properties of InN and In-rich group III-nitride alloys. *J Phys D Appl Phys*. 2006;39(5):R83. doi:10.1016/j.jcrysgro.2004.05.041.
8. Soto Rodriguez PED, Gómez VJ, Kumar P, Calleja E, Nötzel R. Near-infrared InN quantum dots on high-In composition InGaN. *Appl Phys Lett*. 2013;102(13):131909.
9. Aseev P, Rodriguez PEDS, Gómez VJ, et al. Near-infrared emitting In-rich InGaN layers grown directly on Si: Towards the whole composition range. *Appl Phys Lett*. 2015;106(7):072102. doi:10.1063/1.4909515.
10. Alvi NH, Soto Rodriguez PED, Gómez VJ, et al. Highly efficient potentiometric glucose biosensor based on functionalized InN quantum dots. *Appl Phys Lett*. 2012;101(15):153110. doi:10.1063/1.4758701.
11. Alvi NUH, Rodriguez PEDS, Gómez VJ, Kumar P, Willander M, Nötzel R. Highly sensitive and fast anion-selective InN quantum dot electrochemical sensors. *Appl Phys Express*. 2013;6(11):115201. doi:10.7567/APEX.6.115201.
12. Hsu L, Walukiewicz W. Modeling of InGaN/Si tandem solar cells. *J Appl Phys*.

2008;104(2). doi:10.1063/1.2952031.

13. Pearton SJ, Zolper JC, Shul RJ, Ren F. GaN: Processing, defects, and devices. *J Appl Phys*. 1999;86(1):1-78. doi:10.1063/1.371145.
14. Pearton SJ, Ren F, Zhang AP, Lee KP. Fabrication and performance of GaN electronic devices. *Mater Sci Eng R Reports*. 2000;30(3-6):55-212. doi:10.1016/S0927-796X(00)00028-0.
15. Denbaars SP. Gallium-nitride-based materials for blue to ultraviolet optoelectronics devices. *Proc IEEE*. 1997;85(11):1740-1749. doi:10.1109/5.649651.
16. Ambacher O. Thermal stability and desorption of Group III nitrides prepared by metal organic chemical vapor deposition. *J Vac Sci Technol B Microelectron Nanom Struct*. 1996;14(6):3532. doi:10.1116/1.588793.
17. Böttcher T, Einfeldt S, Kirchner V, et al. Incorporation of indium during molecular beam epitaxy of InGaN. *Appl Phys Lett*. 1998;3232(22):3232-3234. doi:10.1063/1.122728.
18. Shimizu M, Hiramatsu K, Sawaki N. Metalorganic vapor phase epitaxy growth of (InxGa1-xN/GaN)n layered structures and reduction of indium droplets. *J Cryst Growth*. 1994;145(1-4):209-213. doi:10.1016/0022-0248(94)91052-9.
19. Aseev P, Rodriguez PEDS, Kumar P, et al. Uniform Low-to-High In Composition InGaN Layers Grown on Si. *Appl Phys Express*. 2013;6(11):115503. doi:10.7567/APEX.6.115503.
20. Kumar P, Rodriguez PEDS, Gómez VJ, Alvi NH, Calleja E, Nötzel R. First demonstration of direct growth of planar high-In-composition InGaN layers on Si. *Appl Phys Express*. 2013;6(3):035501. doi:10.7567/APEX.6.035501.
21. Fabien CAM, Gunning BP, Alan Doolittle W, et al. Low-temperature growth of InGaN films over the entire composition range by MBE. *J Cryst Growth*. 2015;425:115-118. doi:10.1016/j.jcrysgro.2015.02.014.
22. Yamaguchi T, Uematsu N, Araki T, Honda T, Yoon E, Nanishi Y. Growth of thick InGaN films with entire alloy composition using droplet elimination by radical-beam irradiation. *J Cryst Growth*. 2013;377:123-126. doi:10.1016/j.jcrysgro.2013.05.009.
23. Matsuoka T, Yoshimoto N, Sasaki T, Katsui A. Wide-gap semiconductor InGaN and InGaAln grown by MOVPE. *J Electron Mater*. 1992;21(2):157-163. doi:10.1007/BF02655831.
24. Alvi NUH, Gómez VJ, Soto Rodriguez PED, et al. An InN/InGaN quantum dot

electrochemical biosensor for clinical diagnosis. *Sensors (Basel)*. 2013;13(10):13917-13927. doi:10.3390/s131013917.

25. Alvi NH, Soto Rodriguez PED, Kumar P, et al. Photoelectrochemical water splitting and hydrogen generation by a spontaneously formed InGaN nanowall network. *Appl Phys Lett*. 2014;104(22). doi:10.1063/1.4881324.
26. Ivanov S V., Shubina T V., Jmerik VN, Vekshin VA, Kop'ev PS, Monemar B. Plasma-assisted MBE growth and characterization of InN on sapphire. *J Cryst Growth*. 2004;269(1):1-9. doi:10.1016/j.jcrysgro.2004.05.027.
27. Tarsa EJ, Heying B, Wu XH, Fini P, DenBaars SP, Speck JS. Homoepitaxial growth of GaN under Ga-stable and N-stable conditions by plasma-assisted molecular beam epitaxy. *J Appl Phys*. 1997;82(11):5472-5479. doi:10.1063/1.365575.
28. Fernández-Garrido S, Grandal J, Calleja E, Sánchez-García MA, López-Romero D. A growth diagram for plasma-assisted molecular beam epitaxy of GaN nanocolumns on Si (111). *Appl Phys*. 2009;106(111):126102. doi:10.1063/1.3267151.
29. Mi Z, C. Jagadish. *III-Nitride Semiconductor Optoelectronics*.; 2017.
30. Jain SC, Willander M, Narayan J, Overstraeten R Van. APPLIED PHYSICS REVIEWS. 2005;965(2000). doi:10.1063/1.371971.
31. Ruterana P, Albrecht M, Neugebauer J. *Nitride Semiconductors: Handbook on Materials and Devices*.; 2006. doi:10.1002/3527607641.
32. Gómez VJ, Gačević Z, Soto-Rodríguez PED, et al. Comparative study of single InGaN layers grown on Si(111) and GaN(0001) templates: The role of surface wetting and epitaxial constraint. *J Cryst Growth*. 2016;447:48-54. doi:10.1016/j.jcrysgro.2016.04.007.
33. Consonni V, Hanke M, Knelangen M, Geelhaar L, Trampert A, Riechert H. Nucleation mechanisms of self-induced GaN nanowires grown on an amorphous interlayer. *Phys Rev B*. 2011;83(3):35310.
34. Zhang B, Egawa T, Ishikawa H, Liu Y, Jimbo T. High-bright InGaN multiple-quantum-well blue light-emitting diodes on Si (111) using AlN/GaN multilayers with a thin AlN/AlGaN buffer layer. *Jpn J Appl Phys*. 2003;42(3A):L226.
35. Nakada Y, Aksenov I, Okumura H. GaN heteroepitaxial growth on silicon nitride buffer layers formed on Si (111) surfaces by plasma-assisted molecular beam epitaxy. *Appl Phys Lett*. 1998;73(6):827-829. doi:10.1063/1.122014.

36. Glas F. Critical dimensions for the plastic relaxation of strained axial heterostructures in free-standing nanowires. *Phys Rev B*. 2006;74(12):1-4. doi:10.1103/PhysRevB.74.121302.
37. Hauswald C, Corfdir P, Zettler JK, et al. Origin of the nonradiative decay of bound excitons in GaN nanowires. *Phys Rev B*. 2014;90(16):165304.
38. Young EC, Grandjean N, Mates TE, Speck JS. Calcium impurity as a source of non-radiative recombination in (In, Ga) N layers grown by molecular beam epitaxy. *Appl Phys Lett*. 2016;109(21):212103.
39. Zettler JK, Hauswald C, Corfdir P, et al. High-temperature growth of GaN nanowires by molecular beam epitaxy: toward the material quality of bulk GaN. *Cryst Growth Des*. 2015;15(8):4104-4109.
40. Landré O, Fellmann V, Jaffrennou P, et al. Molecular beam epitaxy growth and optical properties of AlN nanowires. *Appl Phys Lett*. 2010;96(6):061912. doi:10.1063/1.3315943.
41. Yanxiong E, Hao Z, Yu J, et al. MBE Growth of AlN Nanowires on Si Substrates by Aluminizing Nucleation. *Nanoscale Res Lett*. 2015. doi:10.1186/s11671-015-1083-0.
42. Zhao S, Connie AT, Dastjerdi MHT, et al. Aluminum nitride nanowire light emitting diodes: Breaking the fundamental bottleneck of deep ultraviolet light sources. *Sci Rep*. 2014;5:1-5. doi:10.1038/srep08332.
43. Grele RJ. MBE deserves a place in the history books. *Oral Hist Rev*. 2007;34(2):121-123. doi:10.1525/ohr.2007.34.2.121.
44. Cho AY. Film deposition by molecular-beam tecgniques. *J Vac Sci Technol*. 1970;8:S31.
45. Arthur Jr JR. Interaction of Ga and As2 molecular beams with GaAs surfaces. *J Appl Phys*. 1968;39(8):4032-4034.
46. Kendrick CE. Revisiting Nitride Semiconductors : Epilayers , p-Type Doping and Nanowires. 2008;(September).
47. Somaschini C, Bietti S, Koguchi N, Sanguinetti S. Coupled quantum dot–ring structures by droplet epitaxy. *Nanotechnology*. 2011;22(18):185602.
48. Watanabe K, Koguchi N, Gotoh Y. Fabrication of GaAs quantum dots by modified droplet epitaxy. *Jpn J Appl Phys*. 2000;39(2A):L79.
49. Bietti S. Nanostructured III-V epilayers on silicon substrate for optoelectronic applications. *PhD thesis*. 2010.
50. Kelly PJ, Arnell RD. Magnetron sputtering: a review of recent developments and

applications. *Vacuum*. 2000;56(3):159-172.

51. Search H, Journals C, Contact A, Iopscience M, Address IP. UHV sputter deposition with a research-scale DC magnetron. 1988;1029.
52. Ichimiya A, Cohen P. Reflection High Energy Electron Diffraction. 2004:353.
53. Thesis D, Eduardo P, Soto D. INVESTIGATIONS ON III-N ITRIDES NANOSTRUCTURES : APPLICATION TO R ENEWABLE E NERGIES AND B IO -S ENSING. 2016.
54. Dobson PJ, Joyce BA, Neave JH, Zhang J. Current understanding and applications of the RHEED intensity oscillation technique. *J Cryst Growth*. 1987;81(1-4):1-8.
55. Lengeler B, Jiilich K, Oberflfichenanalytik M Der, Gruehn R, Universitgt D, Durchstrahlungs-elektronenmikroskopie H. Plenary lectures Surface and microrange analysis. 1989:781-782.
56. O'Donnell KP, Mosselmans JFW, Martin RW, Pereira S, White ME. Structural analysis of InGaN epilayers. *J Phys Condens Matter*. 2001;13(32):6977.
57. Levinshtein ME, Rumyantsev SL, Shur MS. *Properties of Advanced Semiconductor Materials: GaN, AIN, InN, BN, SiC, SiGe*. John Wiley & Sons; 2001.
58. Fujita EFE, Gonser EU, Panish RMOMB, Lotsch MEHK V. *Molecular Beam Epitaxy Fundamentals and Current Status*. Springer Series in Materials Science
59. *MATERIAL AND DEVICE SEMICONDUCTOR Third Edition*.
60. Monemar B, Paskov PP, Bergman JP, et al. Transient photoluminescence of shallow donor bound excitons in GaN. *Phys Rev B - Condens Matter Mater Phys*. 2010;82(23):1-10. doi:10.1103/PhysRevB.82.235202.
61. Schroder DK. *Semiconductor Material and Device Characterization*. John Wiley & Sons; 2006.
62. Winden A, Mikulics M, Grützmacher D, Hardtdegen H. Vertically integrated (Ga, In) N nanostructures for future single photon emitters operating in the telecommunication wavelength range. *Nanotechnology*. 2013;24(40):405302.
63. Hamers RJ, Tromp RM, Demuth JE. Surface electronic structure of Si (111)-(7×7) resolved in real space. *Phys Rev Lett*. 1986;56(18):1972-1975. doi:10.1103/PhysRevLett.56.1972.
64. Yokota K, Tamura S, Huang D, et al. Related content First Observation of the Si (111) -7 × 7 ↔ 1 × 1 Phase Transition by the Optical Second Harmonic Generation. *Jpn J Appl Phys*.

1993;32(111):L610-L613.

65. Heying B, Averbeck R, Chen LF, Haus E, Riechert H, Speck JS. Control of GaN surface morphologies using plasma-assisted molecular beam epitaxy C. 2005;1855(2000). doi:10.1063/1.1305830.

66. Yamaguchi T, Nanishi Y. Indium droplet elimination by radical beam irradiation for reproducible and high-quality growth of InN by RF molecular beam epitaxy. *Appl Phys Express*. 2009;2(5). doi:10.1143/APEX.2.051001.

67. Clinton EA, Vadiee E, Fabien CAM, et al. A review of the synthesis of reduced defect density InxGa1−xN for all indium compositions. *Solid State Electron*. 2017;136:3-11. doi:10.1016/j.sse.2017.06.020.

68. Adelmann C, Brault J, Jalabert D, et al. Dynamically stable gallium surface coverages during plasma-assisted molecular-beam epitaxy of (0001) GaN. *J Appl Phys*. 2002;91(12):9638-9645. doi:10.1063/1.1471923.

69. Valdueza-Felip S, Bellet-Amalric E, Núñez-Cascajero a., et al. High In-content InGaN layers synthesized by plasma-assisted molecular-beam epitaxy: Growth conditions, strain relaxation, and In incorporation kinetics. *J Appl Phys*. 2014;116(23):233504. doi:10.1063/1.4903944.

70. Cho SH, Sakamoto H, Akimoto K, Okada Y, Kawabe M. Epitaxial growth of GaN on sapphire (0001) substrates by electron cyclotron resonance molecular beam epitaxy. *Jpn J Appl Phys*. 1995;34(2B):L236.

71. Zywietz T, Neugebauer JJJ, Scheffler M, Scheffler M. Adatom diffusion at GaN (0001) and (0001) surfaces. *Appl Phys Lett*. 1998;73(4):487-489. doi:10.1063/1.121909.

72. Wagner RS, Ellis WC. Vapor-liquid-solid mechanism of single crystal growth. *Appl Phys Lett*. 1964;4(5):89-90. doi:10.1063/1.1753975.

73. Venables JA. Atomic processes in crystal growth. *Surf Sci*. 1994;299/300:798.

74. Kruse C, Einfeldt S, Böttcher T, Hommel D, Rudloff D, Christen J. Spatially modified layer properties related to the formation of gallium droplets on GaN(0001) surfaces during plasma-assisted molecular-beam epitaxy. *Appl Phys Lett*. 2001;78(24):3827-3829. doi:10.1063/1.1377629.

75. Kawamura T, Hayashi H, Miki T, Suzuki Y, Kangawa Y, Kakimoto K. Molecular beam epitaxy growth of GaN under Ga-rich conditions investigated by molecular dynamics

simulation. *Jpn J Appl Phys*. 2014;53:05FL08. doi:10.7567/JJAP.53.05FL08.

76. Matsuoka T, Okamoto H, Nakao M, Harima H, Kurimoto E. Optical bandgap energy of wurtzite InN. *Appl Phys Lett*. 2002;81(7):1246-1248.

77. Kuykendall T, Ulrich P, Aloni S, Yang P. Complete composition tunability of InGaN nanowires using a combinatorial approach. *Nat Mater*. 2007;6(12):951.

78. Gačević Ž, Gómez VJ, García Lepetit N, et al. A comprehensive diagram to grow (0001)InGaN alloys by molecular beam epitaxy. *J Cryst Growth*. 2013;364:123-127. doi:10.1016/j.jcrysgro.2012.11.031.

79. Yoshimoto N, Matsuoka T, Sasaki T, Katsui A. Photoluminescence of InGaN films grown at high temperature by metalorganic vapor phase epitaxy. *Appl Phys Lett*. 1991;59(18):2251-2253.

80. Davydov VY, Klochikhin AA, Emtsev V V., et al. Photoluminescence and Raman study of hexagonal InN and In-rich InGaN alloys. *Phys Status Solidi Basic Res*. 2003;240(2):425-428. doi:10.1002/pssb.200303448.

81. Correia MR, Pereira S, Pereira E, et al. Raman study of the A1(LO) phonon in relaxed and pseudomorphic InGaN epilayers. *Appl Phys Lett*. 2003;83(23):4761-4763. doi:10.1063/1.1627941.

82. Hernandez S, Cusco R, Pastor D, et al. Raman-scattering study of the InGaN alloy over the whole composition range. *J Appl Phys*. 2005;98(1):0-5. doi:10.1063/1.1940139.

83. Alexson D, Bergman L, Nemanich RJ, et al. Ultraviolet Raman study of and alloys Ultraviolet Raman study of A 1 „ LO … and E 2 phonons in In x Ga 1 À x N alloys. *J Appl Phys*. 2012;241(1998). doi:10.1063/1.1330760.

84. Oliva R, Ibanez J, Cusco R, et al. Raman scattering by the E2h and A1(LO) phonons of InxGa1-xN epilayers (0.25 < x < 0.75) grown by molecular beam epitaxy. *J Appl Phys*. 2012;1:0-9. doi:10.1063/1.3693579.

85. Johnsona MAL, Hughes WC, Rowland WH, et al. Growth of GaN, InGaN, and AlGaN films and quantum well structures by molecular beam epitaxy. *J Cryst Growth*. 1997;175:76-72.

86. Azadmand M, Barabani L, Bietti S, et al. Droplet Controlled Growth Dynamics in Molecular Beam Epitaxy of Nitride Semiconductors. *Sci Rep*. 2018;8(1):11278.

87. Grille H, Bechstedt F. Phonons in ternary group-III nitride alloys. *Phys Rev B*.

2000;61(9):20-25.

88. Correia MR, Pereira S, Pereira E, et al. Direct evidence for strain inhomogeneity in In x Ga 1− x N epilayers by Raman spectroscopy. *Appl Phys Lett*. 2004;85(12):2235-2237.

89. Kozawa T, Kachi T, Kano H, Taga Y, Hashimoto M. Raman scattering from LO phononplasmon coupled modes in gallium nitride Raman scattering. *J Appl Phys*. 2012;1098(1994). doi:10.1063/1.356492.

90. Inushima T, Shiraishi T, Davydov VY. Phonon structure of InN grown by atomic layer epitaxy. *Solid State Commun*. 1999;110(9):491-495. doi:10.1016/S0038-1098(99)00108-8.

91. Iliopoulos E, Georgakilas A, Dimakis E, et al. InGaN(0001) alloys grown in the entire composition range by plasma assisted molecular beam epitaxy. *Phys Status Solidi Appl Mater Sci*. 2006;203(1):102-105. doi:10.1002/pssa.200563509.

92. Ho I, Stringfellow GB. Solid phase immiscibility in GaInN. *Appl Phys Lett*. 1996;69(18):2701-2703. doi:10.1063/1.117683.

93. Wakahara A, Tokuda T, Dang X-Z, Noda S, Sasaki A. Compositional inhomogeneity and immiscibility of a GaInN ternary alloy. *Appl Phys Lett*. 1997;71(7):906-908. doi:10.1063/1.119684.

94. Karpov SY. Suppression of phase separation in InGaN due to elastic strain. *Mater Res Soc Internet J Nitride Semicond Res*. 1998;3(1998):6-10.

95. Doppalapudi D, Basu SN, Ludwig Jr KF, Moustakas TD. Phase separation and ordering in InGaN alloys grown by molecular beam epitaxy. *J Appl Phys*. 1998;84(3):1389-1395.

96. El-Masry NA, Piner EL, Liu SX, Bedair SM. Phase separation in InGaN grown by metalorganic chemical vapor deposition. *Appl Phys Lett*. 1998;72(1):40-42.

97. Zhu XL, Guo LW, Ge BH, et al. Observation of metallic indium clusters in thick InGaN layer grown by metal organic chemical vapor deposition. *Appl Phys Lett*. 2007;91(17):1-5. doi:10.1063/1.2802073.

98. Lu H, Thothathiri M, Wu Z, Bhat I. Study of Indium Droplets Formation on the InxGal_xN Films by Single Crystal X-Ray Diffraction. 1997;26(3):3-6.

99. Voorhees PW. The theory of Ostwald ripening. *J Stat Phys*. 1985;38(1-2):231-252.

100. Priante G, Glas F, Patriarche G, Pantzas K, Oehler F, Harmand J-C. Sharpening the interfaces of axial heterostructures in self-catalyzed AlGaAs nanowires: experiment and theory. *Nano Lett*. 2016;16(3):1917-1924.

101. Koblmüller G, Calleja E, Speck JS. In situ investigation of growth modes during plasma-assisted molecular beam epitaxy of (0001) GaN In situ investigation of growth modes during plasma-assisted molecular beam epitaxy of „ 0001 … GaN. 2013;161904(0001):2005-2008. doi:10.1063/1.2789691.

102. Komaki H, Katayama R, Onabe K, Ozeki M, Ikari T. Nitrogen supply rate dependence of InGaN growth properties, by RF-MBE. *J Cryst Growth*. 2007;305(1):12-18.

103. Yu Z, Buczkowski SL, Giles NC, Myers TH, Richards-Babb MR. The effect of atomic hydrogen on the growth of gallium nitride by molecular beam epitaxy. *Appl Phys Lett*. 1996;69(18):2731-2733.

104. Che SB, Shinada T, Mizuno T, Wang X, Ishitani Y, Yoshikawa A. Effect of precise control of V/III ratio on in-rich InGaN epitaxial growth. *Japanese J Appl Physics, Part 2 Lett*. 2006;45(46-50). doi:10.1143/JJAP.45.L1259.

105. Heying B, Smorchkova I, Poblenz C, et al. Optimization of the surface morphologies and electron mobilities in GaN grown by plasma-assisted molecular beam epitaxy Optimization of the surface morphologies and electron mobilities in GaN grown by plasma-assisted molecular beam epitaxy. 2007;2885(2000):1-4. doi:10.1063/1.1322370.

106. Le Donne A, Binetti S, Isella G, et al. Structural characterization of nc-Si films grown by low-energy PECVD on different substrates. *Appl Surf Sci*. 2008;254(9):2804-2808.

107. Greytak AB, Barrelet CJ, Li Y, Lieber CM. Semiconductor nanowire laser and nanowire waveguide electro-optic modulators. *Appl Phys Lett*. 2005;87(15):1-3. doi:10.1063/1.2089157.

108. Qian F, Gradecak S, Li Y, Wen C-Y, Lieber CM. Core/multishell nanowire heterostructures as multicolor, high-efficiency light-emitting diodes. *Nano Lett*. 2005;5(11):2287-2291.

109. Cui Y, Lieber CM. Functional nanoscale electronic devices assembled using silicon nanowire building blocks. *Science (80-)*. 2001;291(5505):851-853. doi:10.1126/science.291.5505.851.

110. Johansson J, Svensson CPT, Ma T, Samuelson L. Mass Transport Model for Semiconductor Nanowire Growth. 2005:13567-13571.

111. Meijers RÃ, Richter T, Calarco R, et al. GaN-nanowhiskers : MBE-growth conditions and optical properties. 2006;289:381-386. doi:10.1016/j.jcrysgro.2005.11.117.

112. Stoica T, Meijers R, Calarco R, Richter T, Lüth H. MBE growth optimization of InN

nanowires. *J Cryst Growth*. 2006;290(1):241-247.

113. Jensen LE, Bjo MT, Persson AI, Ohlsson BJ, Samuelson L. Role of Surface Diffusion in Chemical Beam Epitaxy of InAs Nanowires. 2004:2-5.

114. Sobanska M, Klosek K, Borysiuk J, et al. Enhanced catalyst-free nucleation of GaN nanowires on amorphous Al $_2$ O $_3$ by plasma-assisted molecular beam epitaxy. *J Appl Phys*. 2014;115(4):043517. doi:10.1063/1.4863456.

115. Wacaser BBA, Dick KA, Johansson J, Deppert K, Samuelson L, Borgstro MT. Preferential Interface Nucleation : An Expansion of the VLS Growth Mechanism for Nanowires. 2009;21(2):153-165. doi:10.1002/adma.200800440.

116. Motohisa J, Takeda J, Inari M, Noborisaka J, Fukui T. Growth of GaAs / AlGaAs hexagonal pillars on GaAs (1 1 1) B surfaces by selective-area MOVPE. 2004;23:298-304. doi:10.1016/j.physe.2003.11.279.

117. Geelhaar L, Chèze C, Jenichen B, et al. Properties of GaN Nanowires Grown by Molecular Beam Epitaxy. *IEEE J Sel Top Quantum Electron*. 2011;17(4):878-888. doi:10.1109/JSTQE.2010.2098396.

118. Calabrese G, Corfdir P, Gao G, et al. Molecular beam epitaxy of single crystalline GaN nanowires on a flexible Ti foil. *Appl Phys Lett*. 2016;108(20):202101. doi:10.1063/1.4950707.

119. Yoshizawa M, Kikuchi A, Mori M, Fujita N, Kishino K. Growth of self-organized GaN nanostructures on Al2O3(0001) by RF-radical source molecular beam epitaxy. *Jpn J Appl Phys*. 1997;36(4 B):L459-L462. doi:10.1143/JJAP.36.L459.

120. Schuster F, Furtmayr F, Zamani R, et al. Self-assembled GaN nanowires on diamond. *Nano Lett*. 2012;12(5):2199-2204. doi:10.1021/nl203872q.

121. Calleja E, Monroy E, Sanchez FJ, Calle F, Munoz E. The effect of the III / V ratio and substrate temperature on the morphology and properties of GaN- and AIN-layers grown by molecular beam epitaxy on Si (lll). 1998;0248(97). doi:10.1016/S0022-0248(97)00386-2.

122. Kanamori S. Investigation of reactively sputtered TiN films for diffusion barriers. *Thin Solid Films*. 1986;136(2):195-214. doi:10.1016/0040-6090(86)90280-4.

123. Calarco R, Meijers RJ, Debnath RK, Stoica T, Sutter E, Lüth H. Nucleation and Growth of GaN Nanowires on Si(111) Performed by Molecular Beam Epitaxy. *Nano Lett*. 2007;7(8):2248-2251. doi:10.1021/nl0707398.

124. Kaganer VM, Fernández-Garrido S, Dogan P, Sabelfeld KK, Brandt O. Nucleation, growth, and bundling of GaN nanowires in molecular beam epitaxy: Disentangling the origin of nanowire coalescence. *Nano Lett*. 2016;16(6):3717-3725. doi:10.1021/acs.nanolett.6b01044.

125. Brubaker MD, Levin I, Davydov A V., et al. Effect of AlN buffer layer properties on the morphology and polarity of GaN nanowires grown by molecular beam epitaxy. *J Appl Phys*. 2011;110(5):053506. doi:10.1063/1.3633522.

126. Bertness KA, Roshko A, Mansfield LM, Harvey TE, Sanford NA. Nucleation conditions for catalyst-free GaN nanowires. *J Cryst Growth*. 2007;300(1):94-99. doi:10.1016/j.jcrysgro.2006.10.209.

127. Treeck D Van, Calabrese G, Goertz JJW, et al. Self-assembled formation of long , thin , and uncoalesced GaN nanowires on crystalline TiN films. 2018;11(1):565-576.

128. Wölz M, Hauswald C, Flissikowski T, et al. Epitaxial Growth of GaN Nanowires with High Structural Perfection on a Metallic TiN Film. *Nano Lett*. 2015;15(6):3743-3747. doi:10.1021/acs.nanolett.5b00251.

129. Maus C, Stauden T, Ecke G, Tonisch K, Pezoldt J. Smooth ceramic titanium nitride contacts on AlGaN/GaN-heterostructures. *Semicond Sci Technol*. 2012;27(11):115007. doi:10.1088/0268-1242/27/11/115007.

130. Luther BP, Mohney SE, Jackson TN. Titanium and titanium nitride contacts to n-type gallium nitride. *Semicond Sci Technol*. 1999;13(11):1322-1327. doi:10.1088/0268-1242/13/11/017.

131. Gautier S, Komninou P, Patsalas P, et al. Optical and electrical properties of TiN / n-GaN contacts in correlation with their structural properties. *Semicond Sci Technol*. 2003;18:594-601.

132. Calabrese G, Gao G, Treeck D Van, Corfdir P, Sinito C. Controlling interfacial reactions during the molecular beam epitaxy of GaN nanowires on Ti / Al 2 O 3. *Manuscr Submitt Publ*.

133. Poitevin JM, Lemperiere G, Tardy J. Influence of substrate bias on the composition, structure and electrical properties of reactively d.c.-sputtered TiN films. *Thin Solid Films*. 1982;97(1):69-77. doi:10.1016/0040-6090(82)90418-7.

134. Fernández-Garrido S, Kaganer VM, Sabelfeld KK, et al. Self-regulated radius of

spontaneously formed GaN nanowires in molecular beam epitaxy. *Nano Lett*. 2013;13(7):3274-3280. doi:10.1021/nl401483e.

135. Bendavid A, Martin PJ, Netterfield RP, Kinder TJ. Characterization of the Optical Properties and Composition of TiN , Thin Films b y Spectroscopic. *Surf Interface Anal*. 1996;24(November 1995):627-633.

136. Adjaottor AA, Meletis EI, Logothetidis S, Alexandrou I, Kokkou S. Effect of substrate bias on sputter-deposited TiCx, TiNyand TiCxNythin films. *Surf Coatings Technol*. 1995;76:142-148. doi:10.1016/0257-8972(95)02594-4.

137. Kaiser R. Raman scattering, superconductivity, and phonon density of states of stoichiometric and nonstoichiometric TiN. *Phys Rev B*. 1978;17(3).

138. Tripathy S, Chua SJ, Chen P, Miao ZL. Micro-Raman investigation of strain in GaN and AlxGa1-xN/GaN heterostructures grown on Si(111). *J Appl Phys*. 2002;92(7):3503-3510. doi:10.1063/1.1502921.

139. Langereis E, Heil SBS, Van De Sanden MCM, Kessels WMM. In situ spectroscopic ellipsometry study on the growth of ultrathin TiN films by plasma-assisted atomic layer deposition. *J Appl Phys*. 2006;100(2):23534.

140. Liu R, Bell A, Ponce FA, Chen CQ, Yang JW, Khan MA. Luminescence from stacking faults in gallium nitride. *Appl Phys Lett*. 2005;86(2):21908.

141. Consonni V, Knelangen M, Jahn U, Trampert A, Geelhaar L, Riechert H. Effects of nanowire coalescence on their structural and optical properties on a local scale. *Appl Phys Lett*. 2009;95(24):241910.

142. Gibart P. Metal organic vapour phase epitaxy of GaN and lateral overgrowth. *REPORTS Prog Phys*. 2004;667:667-715. doi:10.1088/0034-4885/67/5/R02.

143. Gorgis A, Flissikowski T, Brandt O, et al. Time-resolved photoluminescence spectroscopy of individual GaN nanowires. *Phys Rev B*. 2012;86(4):41302.

144. Harris JH. Sintered aluminum nitride ceramics for high-power electronic applications. *JOM*. 1998;50(6):56-60.

145. Li J, Fan ZY, Dahal R, Nakarmi ML, Lin JY, Jiang HX. 200 nm deep ultraviolet photodetectors based on AlN. *Appl Phys Lett*. 2006;89(21):1-4. doi:10.1063/1.2397021.

146. Taniyasu Y, Kasu M, Makimoto T. An aluminium nitride light-emitting diode with a wavelength of 210 nanometres. 2006;441(May):325-328. doi:10.1038/nature04760.

147. Kasu M, Kobayashi N. Large and stable field-emission current from heavily Si-doped AlN grown by metalorganic vapor phase epitaxy. *Appl Phys Lett*. 2000;76(20):2910-2912. doi:10.1063/1.126514.

148. Pantha BN, Dahal R, Nakarmi ML, et al. Correlation between optoelectronic and structural properties and epilayer thickness of AlN. *Appl Phys Lett*. 2007;90(24):1-4. doi:10.1063/1.2747662.

149. Liu L, Liu B, Edgar JH, Rajasingam S, Kuball M. Raman characterization and stress analysis of AlN grown on SiC by sublimation. *J Appl Phys*. 2002;92(9):5183-5188. doi:10.1063/1.1506195.

150. Taniyasu Y, Kasu M, Makimoto T. Increased electron mobility in n -type Si-doped AlN by reducing dislocation density. *Appl Phys Lett*. 2006;89(18):2004-2007. doi:10.1063/1.2378726.

151. Landré O, Bougerol C, Renevier H, Daudin B. Nucleation mechanism of GaN nanowires grown on (111) Si by molecular beam epitaxy. *Nanotechnology*. 2009;20(41). doi:10.1088/0957-4484/20/41/415602.

152. Bourret A, Barski A, Rouvière JL, Renaud G, Barbier A. Growth of aluminum nitride on (111) silicon: Microstructure and interface structure. *J Appl Phys*. 1998;83(4):2003-2009. doi:10.1063/1.366929.

153. Safarian J, Kolbeinsen L, Tangstad M. Liquidus of Silicon Binary Systems. 2011;42(7491). doi:10.1007/s11663-011-9507-4.

154. Wang Q, Zhao S, Connie AT, et al. Optical properties of strain-free AlN nanowires grown by molecular beam epitaxy on Si substrates. *Appl Phys Lett*. 2014;104(22):1-5. doi:10.1063/1.4881558.

155. Li W, Guler U, Kinsey N, et al. Refractory plasmonics with titanium nitride: Broadband. *Adv Mater*. 2014;26(47):7959-7965. doi:10.1002/adma.201401874.

156. Sundgren JE. Structure and properties of TiN coatings. *Thin Solid Films*. 1985;128(1):21-44. doi:10.1016/0040-6090(85)90333-5.

157. Patsalas P, Charitidis C, Logothetidis S. The effect of substrate temperature and biasing on the mechanical properties and structure of sputtered titanium nitride thin films. 2000;125:335-340.

158. Briggs JA, Naik G V., Zhao Y, et al. Temperature-dependent optical properties of titanium

nitride. *Appl Phys Lett*. 2017;110(10). doi:10.1063/1.4977840.

159. Fernández-Garrido S, Zettler JK, Geelhaar L, Brandt O. Monitoring the formation of nanowires by line-of-sight quadrupole mass spectrometry: A comprehensive description of the temporal evolution of GaN nanowire ensembles. *Nano Lett*. 2015;15(3):1930-1937. doi:10.1021/nl504778s.

160. Sobanska M, Fernández-Garrido S, Zytkiewicz ZR, et al. Self-assembled growth of GaN nanowires on amorphous AlxOy: from nucleation to the formation of dense nanowire ensembles. *Nanotechnology*. 2016;27(32). doi:10.1088/0957-4484/27/32/325601.

161. Songmuang R, Ben T, Daudin B, Gonzlez D, Monroy E. Identification of III-N nanowire growth kinetics via a marker technique. *Nanotechnology*. 2010;21(29). doi:10.1088/0957-4484/21/29/295605.

162. Consonni V, Dubrovskii VG, Trampert A, Geelhaar L, Riechert H. Quantitative description for the growth rate of self-induced GaN nanowires. *Phys Rev B - Condens Matter Mater Phys*. 2012;85(15):1-7. doi:10.1103/PhysRevB.85.155313.

163. Brandt O, Fernández-Garrido S, Zettler JK, et al. Statistical analysis of the shape of one-dimensional nanostructures: Determining the coalescence degree of spontaneously formed gan nanowires. *Cryst Growth Des*. 2014;14(5):2246-2253. doi:10.1021/cg401838q.

164. Largeau L, Dheeraj DL, Tchernycheva M, Cirlin GE, Harmand JC. Facet and in-plane crystallographic orientations of GaN nanowires grown on. 2008;(111). doi:10.1088/0957-4484/19/15/155704.

165. Jindal V, Shahedipour-Sandvik F. Density functional theoretical study of surface structure and adatom kinetics for wurtzite AlN. *J Appl Phys*. 2009;105(8). doi:10.1063/1.3106164.

166. Zhuang D, Edgar JH. Wet etching of GaN, AlN, and SiC: A review. *Mater Sci Eng R Reports*. 2005;48(1):1-46. doi:10.1016/j.mser.2004.11.002.

167. Jasinski J, Liliental-Weber Z, Paduano QS, Weyburne DW. Inversion domains in AlN grown on (0001) sapphire. *Appl Phys Lett*. 2003;83(14):2811-2813.

168. Kuball M, Hayes JM, Prins AD, et al. Raman scattering studies on single-crystalline bulk AIN under high pressures. *Appl Phys Lett*. 2001;78(6):724-726. doi:10.1063/1.1344567.

169. Siegle H, Syassen K, Thomsen C, Wagner J. Effect of pressure on optical phonon modes and transverse effective charges in GaN and AlN. 2001;64:1-6. doi:10.1103/PhysRevB.64.035205.

170. Nilsson D, Janzén E, Kakanakova-Georgieva A. Lattice parameters of AlN bulk, homoepitaxial and heteroepitaxial material. *J Phys D Appl Phys*. 2016;49(17). doi:10.1088/0022-3727/49/17/175108.

171. Feneberg M, Leute RAR, Neuschl B, Thonke K, Bickermann M. High-excitation and high-resolution photoluminescence spectra of bulk AlN. *Phys Rev B*. 2010;82(7):75208.

172. Bryan Z, Bryan I, Bobea M, et al. Exciton transitions and oxygen as a donor in m-plane AlN homoepitaxial films. *J Appl Phys*. 2014;115(13):133503.

173. Alden D, Harris JS, Bryan Z, et al. Point-Defect Nature of the Ultraviolet Absorption Band in AlN. *Phys Rev Appl*. 2018;9(5):54036.